APPLICATIONS OF SELF-ASSEMBLY

FOR MOLECULAR

ELECTRONICS, PLASMON COUPLING, AND ION SENSING

A Dissertation

by

YANG-HSIANG CHAN

Submitted to the Office of Graduate Studies of
Texas A&M University
in partial fulfillment of the requirements for the degree of

DOCTOR OF PHILOSOPHY

May 2010

Major Subject: Chemistry

APPLICATIONS OF SELF-ASSEMBLY

FOR MOLECULAR

ELECTRONICS, PLASMON COUPLING, AND ION SENSING

A Dissertation

by

YANG-HSIANG CHAN

Submitted to the Office of Graduate Studies of
Texas A&M University
in partial fulfillment of the requirements for the degree of

DOCTOR OF PHILOSOPHY

Approved by:

Chair of Committee,	James D. Batteas
Committee Members,	D. Wayne Goodman
	Emile A. Schweikert
	Hong Liang
Head of Department,	David H. Russell

May 2010

Major Subject: Chemistry

ABSTRACT

Applications of Self-Assembly for Molecular Electronics, Plasmon Coupling, and Ion Sensing. (May 2010)

Yang-Hsiang Chan, B.S., National Sun Yat-sen University

Chair of Advisory Committee: Dr. James D. Batteas

This dissertation focused on the applications of self-assembled monolayers (SAMs) technique for the investigation of molecule based electronics, plasmon coupling between CdSe quantum dots and metal nanoparticles (MNPs), and copper ion detection using enhanced emission of CdSe quantum dots (QDs). The SAMs technique provides an approach to establish a robust, two-dimensional and densely packed structure which can be formed on metal or semiconductor surfaces. This allows for the design of molecular assemblies that can be used to understand the details of molecular conduction by employing various electrical testbeds. In this work, the strategy of molecular assemblies was used to pattern metal nanoparticles on GaAs surfaces, thereby furnishing a platform to explore the interactions between QDs and MNPs. The enhanced emission of CdSe QDs by MNPs was then used as a probe for ultrasensitive, cheap, and rapid copper(II) detection.

The study is divided into three main facets. The first one aimed at controlling electron transport behavior through porphyrins on surfaces with an eye toward optoelectronic and light harvesting applications. The binding of the porphyrin molecules

to Au surfaces, pre-covered with a dodecanethiol matrix, was characterized by FTIR, XPS, AFM, STM, of. This study has shown that the perfluoro coupling group between the porphyrin macrocycle and the thiol tether may provide a means of controlling the tunneling behavior.

The second area of this study focused on the design of a simple platform to examine the coupling between metal nanostructures and quantum dot assemblies. Here we demonstrate that by using a patterned array of Au or Ag nanoparticles on GaAs, plasmon enhanced photoluminescence (PL) can be directly measured and quantified by direct scaling of regions with and without metal nanostructures.

The third field presented a simple manner for using the enhanced PL of CdSe QDs as a probe for ultrasensitive Cu^{2+} ion detection and quantitative analysis. The PL of QDs was enhanced by two processes: first, photobrightening of the material, and second, plasmonic enhancement by coupling with Ag nanoprisms. This strong PL leads to a high sensitivity of the QDs over a wide dynamic range for Cu^{2+} detection, as Cu^{2+} efficiently quenches the QD emission.

ACKNOWLEDGEMENTS

There are so many people I need to thank, so I thank God first. I had never thought about getting a Ph.D. degree one day in my whole life until five years ago when I arrived at Texas A&M University. It is like a dream for me, but it is so true. Thank God for giving me so many opportunities and never giving up on me. I am always satisfied at what I already have and always thankful to those people who help me all the time. Especially, thanks to those people who were unfriendly because they gave me the most powerful motivation to grow up quickly. The most important thanks go to my parents, especially my father in heaven, because there is no me without them. They spent more than twenty years raising me and always gave me any kind of support without hesitation. Thanks to my previous advisor in Taiwan, Dr. Chun-hsien Chen, for pushing me out of Taiwan and letting me have such a wonderful adventure in Texas. Thanks to the government of Taiwan for forcing me to have the two-year military service. From that, I didn't learn how to kill the enemies and defend my country but I learned how to survive under extremely crucial conditions and help people out there.

I have highest regards and gratitude for my advisor, Dr. Batteas, for giving me the chance to work in his group. He is always willing to provide any kind of support to help the students in his group. He didn't despise me because of my pitifully poor English, but tried his best to "speculate" what I intended to say with great patience. Sometime I feel like he might have a much better understanding about "Chinglish" in these years

rather than my improved English. Dr. Batteas' energy, enthusiasm, and positivity have been a tremendous model for me.

I would like to thank Dr. Tinglu Yang for spending hours and hours on teaching me the physical chemistry lab, the photolithography and so on. Thanks to Jason for giving me the hard time all the time, and I love arguing with him. From that, I learned the essence of critical thinking which is very important for the research of science. Thanks for my good groupmates, Dr. Liu, Dr. Liang, Dr. Hong, Amanda, Albert, Ammon, Arika, Chi-Yuan, Ryan, Brad and other people I forgot to mention. Of course, I need to thank my family for tolerating me so long. Finally, I also sincerely thank Miss Huang for giving me the thought of marriage. Unfortunately, I am still not marriage material at this stage (hopefully in the future). Her true love gave me a lot of emotional support that I will never forget in my whole life. I really enjoy every minute living here with all my friends. As I always say: the secret of life is to live every moment.

TABLE OF CONTENTS

CHAPTER Page

LIST OF FIGURES

FIGURE Page

FIGURE Page

FIGURE Page

FIGURE Page

FIGURE Page

LIST OF TABLES

CHAPTER I

INTRODUCTION

1.1. Self-Assembled Monolayers

Self-assembled monolayers (SAMs) are organic layers formed by the chemisorption of molecules onto a substrate from the liquid or the gas phase. SAMs were first developed by Zisman[1] in 1946, in which a monolayer of long-chain alkyl alcohol was formed on a clean metal surface. At that time, it was just the discovery of a phenomenon without recognition of its potential, and was not widely investigated. Early work was initiated by Kuhn, in which a layer of chlorosilane derivative was adsorbed onto the hydrophilic glass, and the name self-assembled monolayers (SAMs) has been given ever since.[2] There have been intense studies in SAMs since 1983 when Nuzzo and Allara demonstrated that the close-packed SAMs of alkanethiolates on gold can be prepared by the adsorption of *di*-*n*-alkyl disulfides onto Au surfaces.[3] In addition to the most common S-Au bond, there is a variety of headgroups that bind to specific metals (Table 1.1).[4] However, due to the inertness of gold and the strong bonding energy between thiolate group and gold surface (approximately 40 kcal mol^{-1}), the field of alkanethiolate SAMs on gold has been the most studied thus far.

This dissertation follows the style and format of *Journal of the American Chemical Society*.

Table 1.1. Combinations of headgroups and substrates used in forming SAMs. (Adapted from ref 4.)

Ligand	Substrate	Ligand	Substrate
ROH	Fe_xO_y	RSSR'	Ag
	Si-H		Au
	Si		CdS
RCOO-/RCOOH	α-Al_2O_3		Pd
	Fe_xO_y	RCSSH	Au
	Ni		CdSe
	Ti/TiO_2	$RS_2O_3^-Na^+$	Au
	Si(111):H		Cu
	Si(100):H	RSeH	Ag
Ene-diol	Fe_2O_3		Au
RNH_2	FeS2		CdS
	Mica		CdSe
	Stainless Steel	RSeSeR'	Au
	$Yba_2Cu_3O_7$	R3P	Au
	CdSe		FeS_2
RCaN	Ag		CdS
	Au		CdSe
$R\text{-}N{\equiv}N^+(BF4^-)$	GaAs(100)		CdTe
	Pd	R3P=O	Co
	Si(111):H		CdS
RSH	Ag		CdSe
	AgS		CdTe
	Au	$RPO_3^{2-}/RP(O)(OH)_2$	Al
	AuAg		Al-OH
	AuCu		$Ca_{10}(PO_4CO_3)_6(OH)_2$
	Au_xPd_{1-x}		GaAs
	CdTe		GaN
	CdSe		Indium tin oxide
	CdS		(ITO)
	Cu		Mica
	FePt		TiO_2
	GaAs		ZrO_2
	Ge		CdSe
	Hg		CdTe
	HgTe	RPO_4^{2-}	Al_2O_3
	InP		Nb_2O_3
	Ir		Ta_2O_3
	Ni		TiO_2
	PbS	RN≡C	Pt
	Pd	$RHC{=}CH_2$	Si
	PdAg	RC≡CH	Si(111):H
	Pt		
	Ru	$RSiX_3$	HfO_2
	Zn	X=H, Cl	
	ZnSe	OCH_2CH_3	ITO
	ZnS		PtO
RSAc	Au		TiO_2
RSR'	Au		ZrO_2

SAMs are formed as the adsorbates organize spontaneously into an ordered monomolecular layer. Take alkanethiol adsorption on Au(111) surface from a liquid solution for example, two distinct kinetics can be observed. The first step is known as a diffusion-controlled Langmuir adsorption process, in which the rate depends on the thiol concentration and the entire procedure takes only a few minutes to achieve 80-90% of its maximal adsorption coverage. The second step is described as a surface crystallization process, in which the thiols on surface exchange with those in solution via desorption. This process takes several hours and leads to the formation of a 2D crystal-like arrangement, in which larger chain-chain van der Waals interactions prevent the further desorption of thiols from the surface. Additionally, kinetics for adsorption from the liquid phase depends on several factors including solvents used for preparing SAMs, temperature, concentration, immersion time, purity of thiols, oxygen content of solution, and cleanliness of substrate.

1.2. Self-Assembled Monolayers of Thiol-Based Molecules on Gold

As shown in Figure 1.1, an alkanethiol SAM can be divided into three parts, which are the head group, the spacer (alkane chain), and the terminal functional group. The headgroup must have a highly specific affinity for the substrate so that bond formation is spontaneous. The procedure of alkanethiol adsorption can be considered as an oxidation of the S-H bond, followed by a reductive elimination of H_2. That is,[5]

$$R\text{-}S\text{-}H + Au_n^{o} \longrightarrow R\text{-}S^{-}Au^{+} \cdot Au_n^{o} + \tfrac{1}{2}\, H_2$$

The bond energies of RS-H, H_2 and RS-Au are 87, 104 and 40 kcal mol^{-1}, respectively, and the net energy for this reaction would be *ca.* -5 kcal mol^{-1}. This reaction is therefore exothermic and spontaneous.

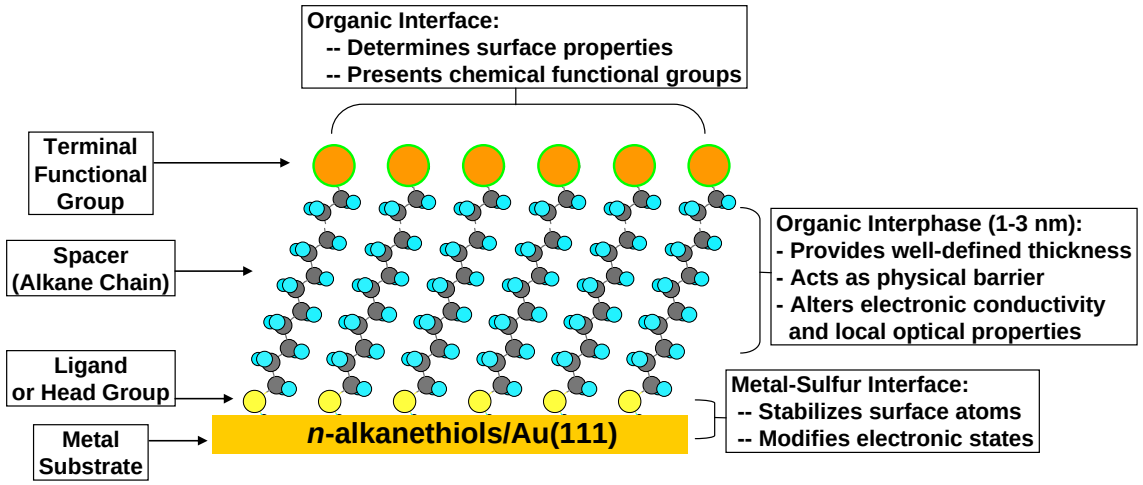

Figure 1.1. Schematic diagram of a well-ordered SAM of alkanethiolates on a metal substrate. (Adapted from ref 4.)

The spacer, in this case an alkane chain, provides Van der Waals (VDW) interactions to stabilize the molecules. Longer alkane chains result in larger VDW interactions among adjacent molecules that make the kinetic step of surface crystallization faster and yield higher ordering of monolayers. The terminal functional group is the contact between the SAM and the environment, and accordingly contributes to the diverse properties of surfaces. SAMs have been reported with terminal functional groups ranging from nonpolar methyl groups to polar hydroxyl groups. Moreover, SAMs with more complex functional groups such as ferrocenyl and biotinyl groups have been explored for the surface phenomena of electron transfer and molecular recognition.[4]

Proper terminal functional groups can be selected or further derivatized for the fabrication and modification of the surface properties.

1.3. Self-Assembled Monolayers on Silicon and GaAs

There has been a great deal of interest in the utilization of semiconductor substrates due to their predominant electronic and optoelectronic properties of interest in industrial applications. The simple preparation and high stability of SAMs on semiconducting substrates makes it inherently manufacturable and technologically applicable for further surface engineering. Here, we focus only on the SAMs on silicon oxide and GaAs because they are most widely employed as substrates for devices in industry due to their superior stability which allows for further surface modification steps with a minimum destruction of molecular structures. For the SAMs on silicon oxide surfaces, the formation and characterization of SAMs of alkylchlorosilane, alkylalkoxysilanes, and alkylaminosilanes on silanol-terminated surfaces *via* strong Si-O-Si covalent bonds have been widely studied recently.[6] The reproducibility of high-quality alkylchlorosilane SAMs on silicon remains a challenge however, because the amount of water in solution greatly influences the formation of silane SAM. It was suggested that a water level of 0.15 mg/100 mL in solvent can provide the optimal conditions for the formation of closely packed SAMs on silicon oxide.[7] Nevertheless, it was found that other parameters such as temperature, solvent, solution age, and deposition time also play significant roles in SAM formation.[8] Thus, the experimental

conditions should be carefully controlled in order to obtain a smooth and well-packed monolayer.

There has been a significant controversy over the mechanism of monolayer formation on silicon oxide.[6] Generally the process of SAMs growth on silicon oxide has been suggested to proceed *via* island-type or homogenous growth, or both, as illustrated in Figure 1.2. For longer-chain molecules, it was found that the SAMs form through an island-type growth. In contrast, shorter-chain molecules exhibit mostly homogenous growth, but both types of growth were observed by several groups using atomic force microscopy, depending on the experimental conditions such as water content and age of the silane solution. A model of a growing monolayer crystallite covered by a thin water layer was proposed by Rye *et al.* as shown in Figure 1.3.[9] The neighboring molecules were bound together the covalent bonds with the hydrocarbon tails orientated perpendicular to the surface normal in order to reduce steric effects. A molecular area of 21-25 $Å^2$ per chain with a tilt angle of 15-17^o from the normal was observed for the alkylsilane SAMs on SiO_2.[8] The general lack of long-range order was attributed to a certain degree of cross-polymerization between neighboring groups.

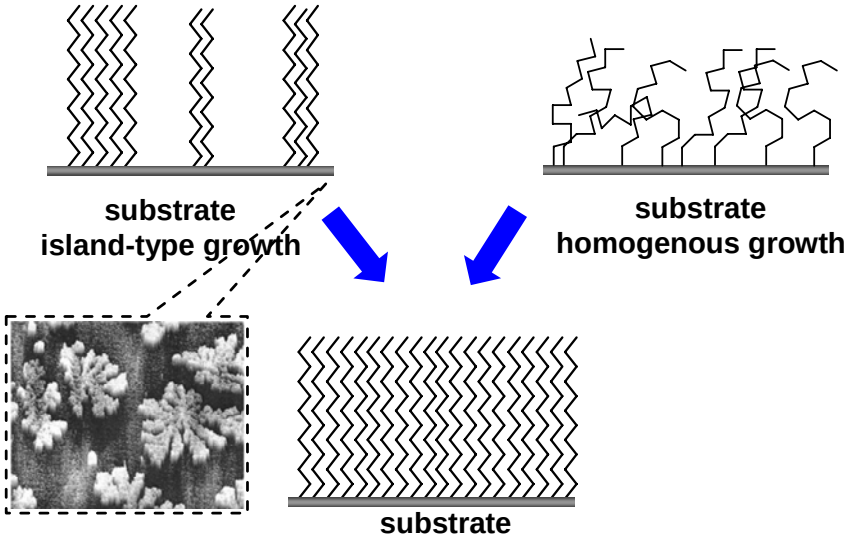

Figure 1.2. Schematic representation of island-type and homogenous growth of alkylsilane SAMs on SiO_2. Inset shows the AFM image (20 x 20 μm^2) of a partial alkylsilane film. (Adapted from ref 6.)

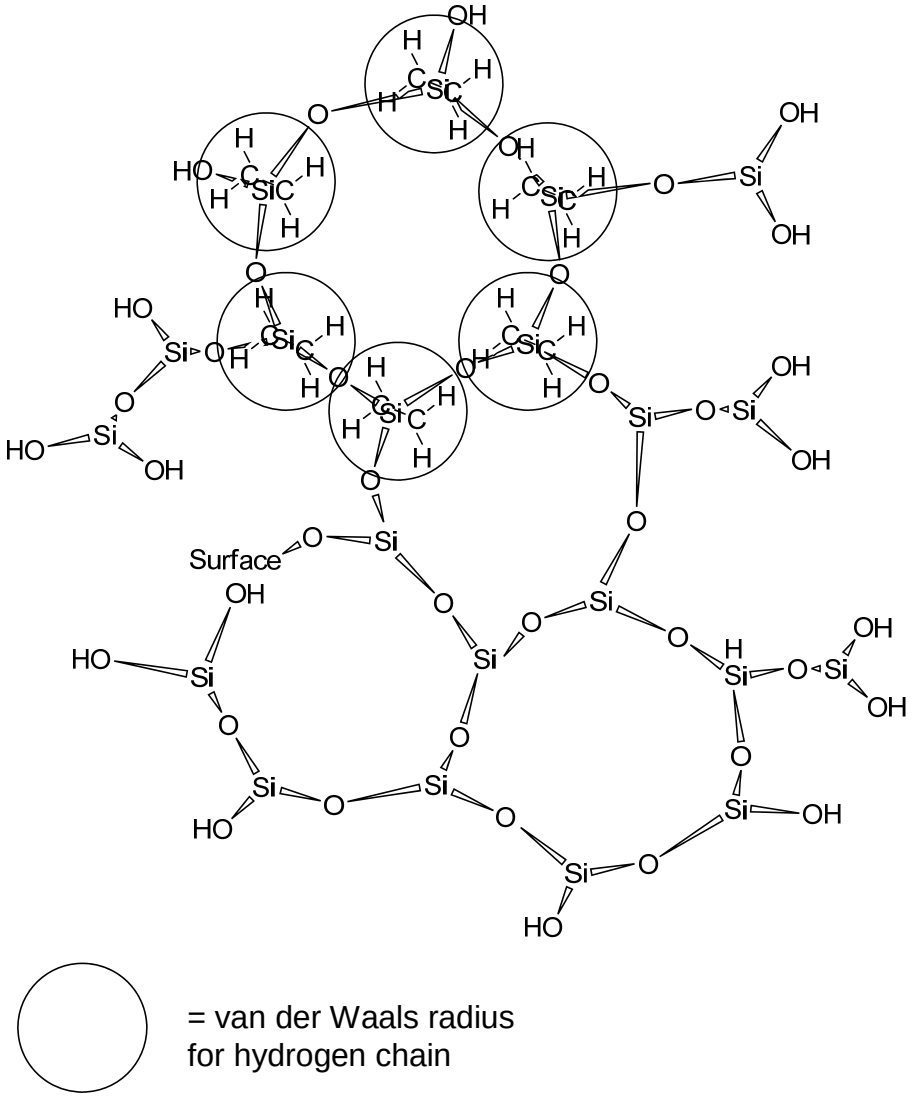

Figure 1.3. Model of a growing silane monolayer crystallite. (Adapted from ref 6.)

Among group III-V semiconductors, GaAs is one of the most widely used materials due to its high saturated electron velocity and high carrier mobility. This makes it extremely suitable for functions in high frequency telecommunications and fast-response electronic devices. Moreover, the direct band gap of GaAs exhibits a higher radiative decay rate and larger absorbance cross section, which renders it more

applicable than Si for light-emitting devices. However, the strong propensity towards oxidization[10,11] of bare GaAs surfaces after a few days in ambient atmosphere is a difficult matter to address. Recently, there have been a number of reports on the passivation of GaAs surfaces with inorganic sulfur molecules[12-14] by removing the native oxide layer using acid and/or base prior to modification. In particular, the use of SAMs has been extensively employed to mediate surface oxidation of GaAs because of the relatively stable, two-dimensional, and densely packed structures that can be formed through robust covalent bonds as compared to Langmuir-Blodgett (LB) films[15] and lipid bilayers.[16] It is therefore possible to tune their electronic and optical properties[17] by modifying the interfacial properties with molecules of various terminal groups. The fabrication of alkanethiolate monolayers on GaAs has been intensely studied recently. A molecular density of ~21.2 $Å^2$/molecule and a nearest neighbor distance of 3.995Å were revealed as shown in Figure 1.4. From Near Edge X-ray Absorption Fine Structure and infrared spectroscopy, the tilt angle of alkanethiol SAMs on GaAs was determined to be 14^o-15^o (Figure 1.4C). However, a tilt angle of $26^o \pm 10^o$ for aromatic thiol monolayer on GaAs was observed (Figure 1.5).[13] For alkanethiols with chains longer than 15 carbons, the SAMs are highly ordered with a herringbone arrangement of the molecules, which has also been seen in the assemblies on Au(111).[13] For chain length smaller than 15, it is diffucult to obtain a substantial ordering SAMs on GaAs due to the diminished van der Waals interactions. Generally, there still exist some challenges for alkanethiol SAMs on GaAs including their slow adsorption rate, poor resistance of the susbtrate to oxidation in air. These disadvantages make thiol SAMs undesirable for GaAs electronic

passivation. The alternative method is to introduce a fresh thin oxide layer as a binding layer onto GaAs surfaces by the exposure of UV-ozone or oxygen plasma after base and acid treatment. There have been only a few reports focusing on using this oxide layer as a binding layer for the adsorption of carboxylic acid,[18] phenylphosphonic acid,[19] and siloxane molecules[20] on GaAs substrates (see chaper IV for details).

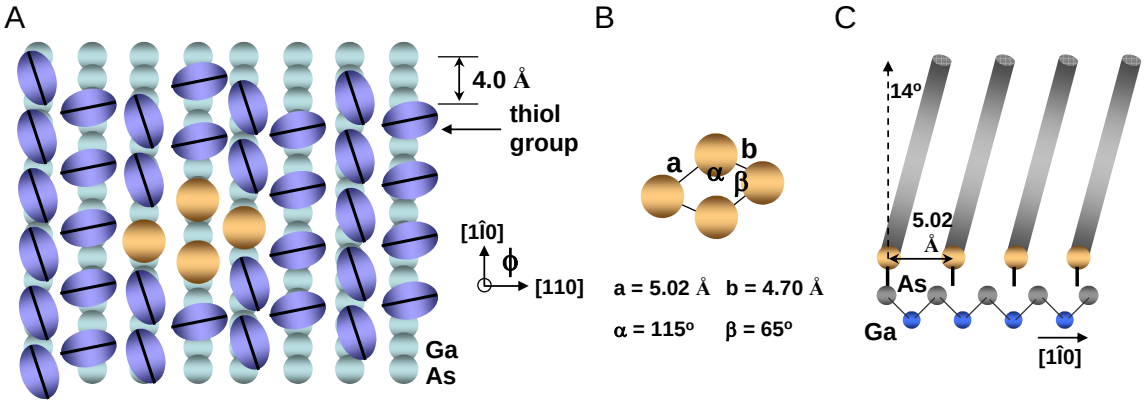

Figure 1.4. (A) Proposed lattice structure superimposed on GaAs(001). (B) A pseudohexagonal unit cell. (C) Schematic side view of alkanethiol adsorbates along the [110] step edge direction of GaAs(001). (Adapted from ref 13.)

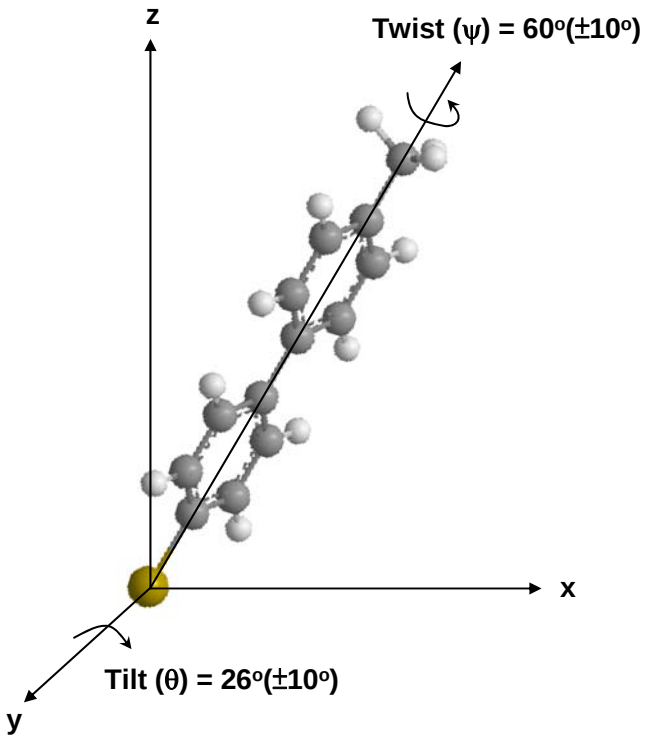

Figure 1.5. Schematic model of aromatic thiols on GaAs. (Adapted from ref 6.)

1.4. Patterning SAMs In Plane

Micro- and nano-fabrication techniques of spatially organized SAMs patterns including proteins/DNA,[21-25] and organic molecules[26-28] have attracted tremendous attention due to their diverse applications[29-32] including miniature electronic devices, catalysis, information storage and biological sensing. Many approaches for the fabrication have been developed such as photolithography,[33,34] microcontact printing,[35,36] direct evaporation,[37] scanning probe lithography,[38-40] electron-beam lithography,[41,42] paylene-based lift-off method,[43] focused ion beam lithography,[44] and nanoimprinting[45] onto metal or semiconductor surfaces. For the microcontact printing technique, the

SAMs are patterned by physically transferring the molecular components to the substrate in a predetermined template (Figure 1.6). The advantage for this strategy is that many features can be generated simultaneously on the substrate covering a large-scale area (up to ~100 cm^2) as compared to the scanning probe lithography in which only one feature can be written at a time. The feature resolution for the microcontact printing ranges from a couple of nm to several mm.

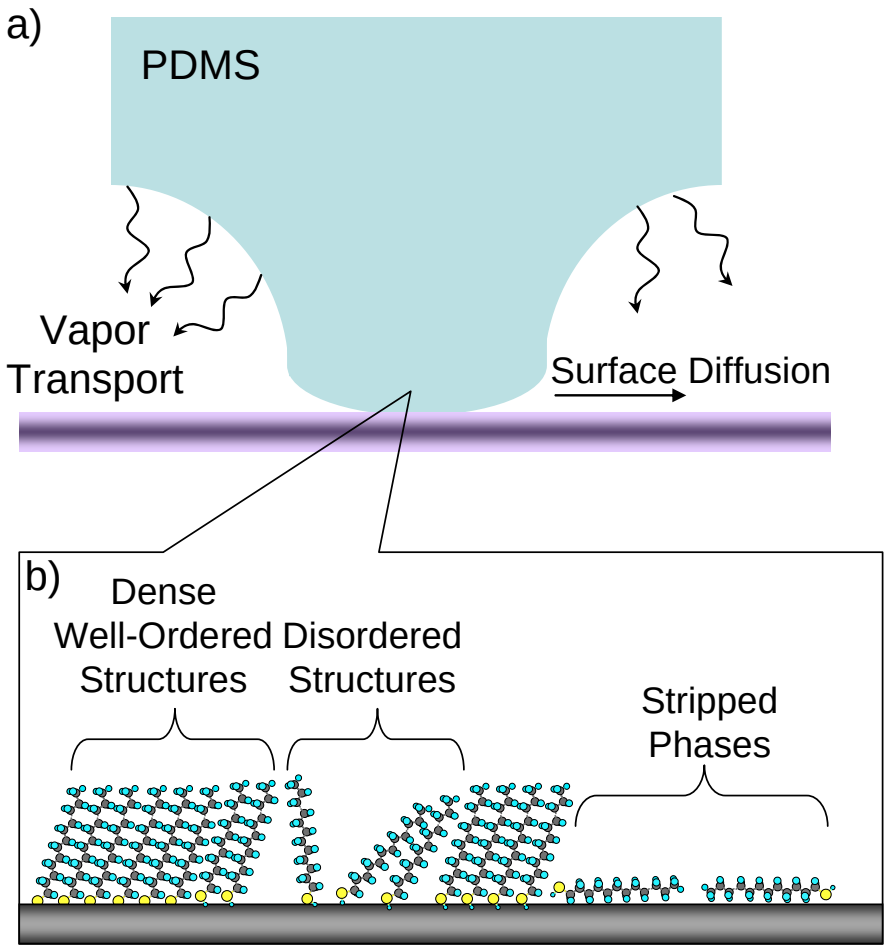

Figure 1.6. (a) Schematic diagram showing the principle of microcontact printing using the PDMS as a stamp. (b) Enlarged view for the contact regions between the stamp and substrate. (Adapted from ref 4.)

Other approaches including photolithography, e-beam lithography, and mechanical scratching rely on the selective damage to the pre-fabricated SAMs. Take photolithography for example, irradiation of the SAMs through a pre-designed photo-mask with UV or laser light results in the oxidation or degradation of the SAMs in the exposed area. The resulting oxidized molecules can then be removed by rinsing with proper solvents or replaced by another SAM by immersing into a second adsorbate solution (see Figure 4.3 as the example). For photolithography, the feature resolution depends on the wavelength of the light source due to the diffraction limitation. Generally it is difficult to reach a resolution less than 100 nm using this method. On the other hand, generating features with dimensions as small as 10 nm is common by means of beam lithography. However, the disadvantage of beam lithography is the cost of the equipment. For the AFM-based lithography (nanoshaving and nanografting), a high local force is applied on the AFM tip during the scan in the contact mode (Figure 1.7). This process leads to the displacement of the adsorbate molecules and a new molecule can therefore fill into the vacancy to create the patterned SAMs. The feature size of the AFM-based lithography can be less than 10 nm depending on the diameter of the AFM tip.

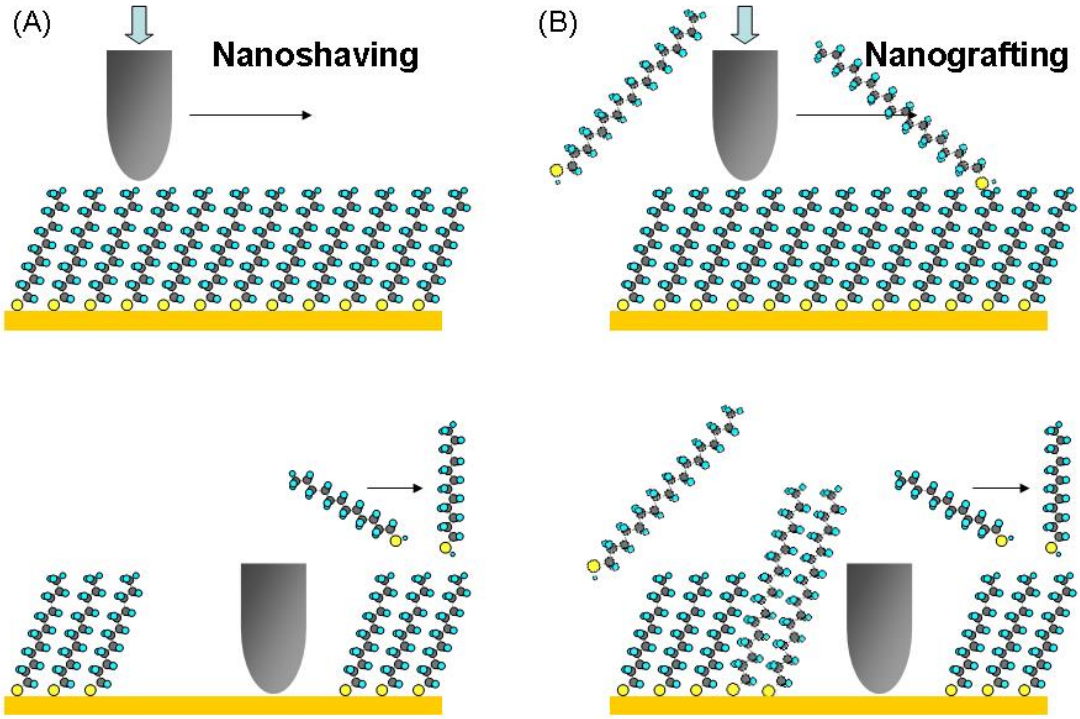

Figure 1.7. Schematic diagrams of basic manipulation mechanisms of AFM-based lithography.

1.5. Summary

Self-assembled monolayers are a very powerful tool for surface engineering. They provide a general and flexible method to tailor the interfacial properties on any geometry or size. Their chemical functionality and thermodynamic stability make them possible to be utilized for more complex systems.

Our interest and main goal of the study reported herein is to use SAMs as a facile tool for various applications. For example, we employed SAMs to investigate the electronic properties of molecules of interest. We also used the patterned SAMs as a template to create arrays of metal nanoparticles on GaAs. Additionally, we used SAMs

as the capping ligands to tune the optical properties of quantum dots *via* simple desorption/re-adsorption processes. This study represents the practical applications of SAMs in several fields including molecular electronics, optics of quantum dots, and biosensing.

CHAPTER II

EXPERIMENTAL

2.1. Atomic Force Microscopy

The Atomic Force Microscope (AFM) was first invented by Gerd Binning in 1986 and has became one of the most powerful analytical techniques in surface science. The AFM consists of a cantilever with sharp tip end, a piezoelectric translator, a quadrant photodetector, and a feedback controller that is connected to a computer (Figure 2.1). When the tip approaches the surface of a sample, the cantilever is deflected by the forces between the tip and sample which include van VDW, capillary, electrostatic, and chemical forces. The displacement of the cantilever in turn leads to a deflection of the laser which is detected by the photodetector. The feedback controller then communicates with the piezoelectric scanner to adjust the height in order to keep the constant vertical deflection force (F_N). The scanning software then constructs a topographic image of the sample surface according to each (x, y, z) data point.

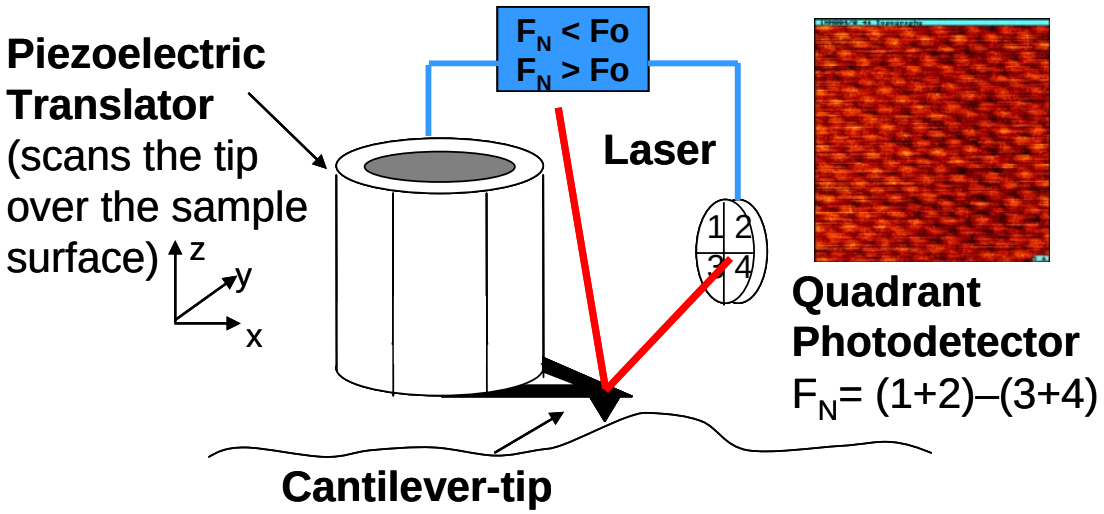

Figure 2.1. Schematic illustration of an atomic force microscope. The inset shows an typical image of mica surface obtained by AFM.

There are several scanning modes in AFM: (1) contact mode: tip touches the surface and relies on maintaining a constant tip-sample force. (2) non-contact mode: tip probes the force gradient of the surface and produces images without touching the surface. (3) intermittent force mode: tip only intermittently contacts the surface and reduces lateral shearing forces while scanning. (4) modulated force mode: tip oscillates in contact with the surface while the changes in amplitude and phase of the tip oscillation provide information on the surface's viscoelastic properties. (5) lateral force mode: tip probes the torsional forces acting on the tip-lever assembly, which can provide information regarding friction and shear contact stress. Different modes are selected depending on the surface properties of the material of interest. For example, the imaging of soft materials is best done using the non-contact mode in order to prevent the destruction of the samples while the biological samples are best scanned under liquid conditions using tapping mode.

2.2. Confocal Fluorescence Microscopy

Confocal Fluorescence Microscopy is a technique which provides true three-dimensional optical resolution. The principle of this technique was first advanced by Marvin Minsky and then patented in 1957.[46] In confocal fluorescence microscopy (Figure 2.2), the light coming from the laser passes through a pinhole and is reflected by a dichroic mirror. The light is then focused by an objective lens into a small focal volume on the surface of a sample. The dichroic mirror reflects shorter wavelength light while transmitter longer wavelengths. Therefore, longer wavelength fluorescent light emitted from the sample is transmitted by the dichroic mirror and then collected by the detector while the light from scattering or reflection is blocked. The detector can be a photomultiplier tube (PMT), charge-coupled device (CCD), or any other light-sensitive device.

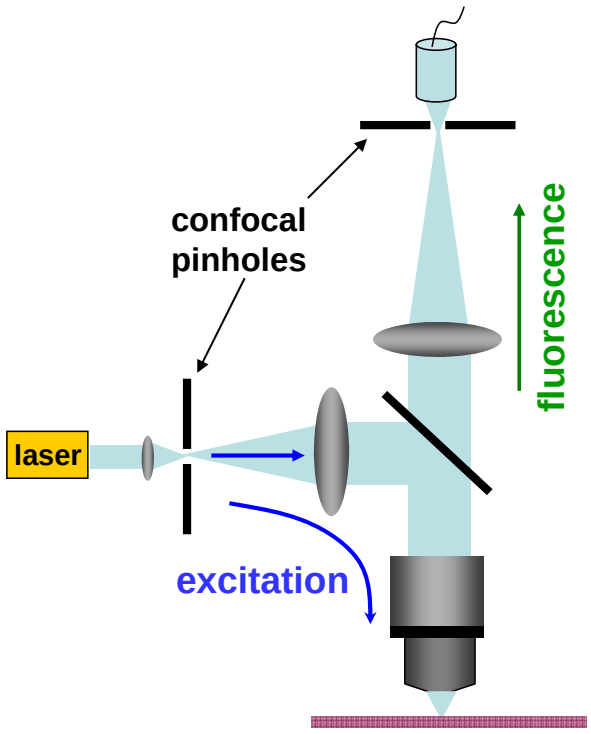

Figure 2.2. Schematic illustration of the fluorescence confocal laser scanning microscopy.

In confocal fluorescence microscopy, any signal from the out-of-focus planes is suppressed by an aperture as depicted in Figure 2.2. Only light originating from the in-focus planes is imaged by the detector. The position of this pinhole is in a conjugate plane with both the plane of focus of the microscope objective and the point of excitation of the laser (excitation pinhole). True three-dimensional resolution is therefore accomplished by collecting a single point at a time, which usually requires long imaging time.

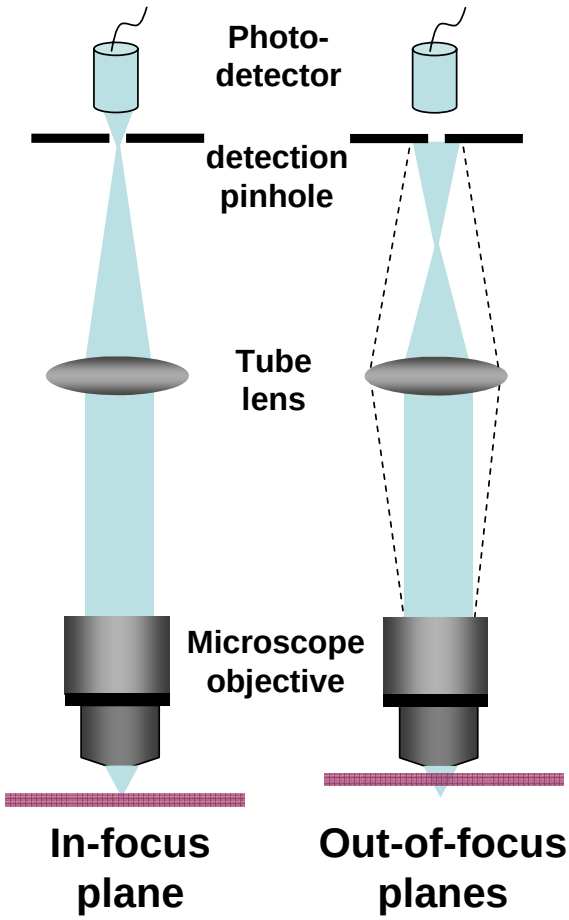

Figure 2.3. The principle of confocal fluorescence microscopy.

2.3. Scanning Tunneling Microscope

Scanning tunneling microscopy (STM) is a technique which was invented by Russell Young in 1972. This technique was further developed by Binning and Rhorer in 1981 to achieve vibration isolation[47] and later demonstrated atomic resolution of the Si (111)-7x7 surface.[48] Binning and Rohrer were awarded the 1986 Nobel Prize in Physics for their elaborate design of the STM. An STM is capable of imaging electrically

conducting surfaces down to atomic scale by applying a positive or negative bias between the tip and sample, while the tunneling current is employed as the feedback (Figure 2.3). With tunneling, not structural properties, but electronic properties can be obtained, which allows for a diversity of applications. In addition, recent reports have shown the manipulation of individual atoms and molecules[49] on surfaces by the STM tip. To date, STM has revealed many interesting phenomena in the field of molecular electronics including negative differential resistance,[50] field effect transistors,[51] information storage, molecular rectifiers,[52] and reversible redox switching.[53,54]

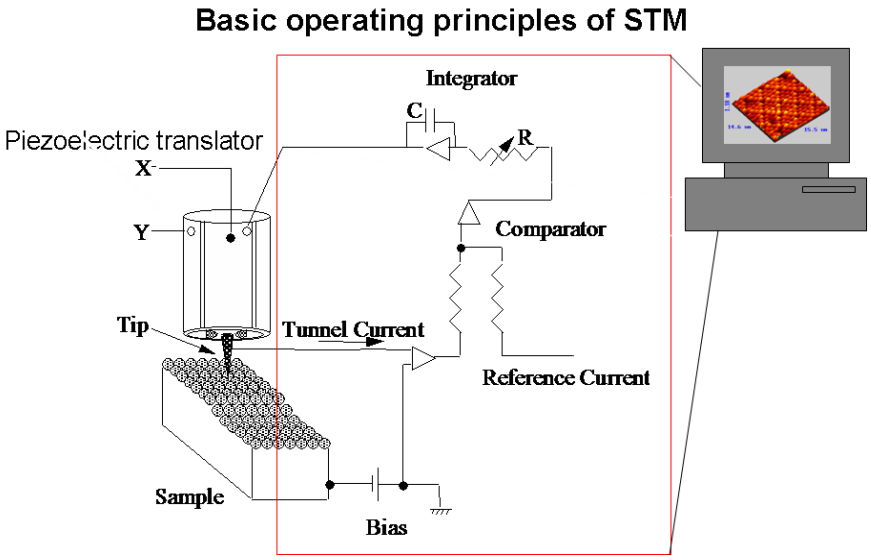

Figure 2.4. Schematic diagram of the working components of an STM.

The principle of STM relies on the process of quantum tunneling. When the STM is brought close to the surface without touching it under potential, electrons will tunnel from the tip to the sample or from the sample to the tip depending on the applied bias,

without crossing the potential barrier (Figure 2.4). The electron tunneling is dictated by the overlap of tip and sample wavefunctions. The current passing through the vacuum barrier decays exponentially with the distance between the tip and sample as shown below (Figure 2.5):

$$I \sim Ve^{-kz}$$

Where I is the tunneling current, V is the bias between the tip and sample, k is a tunneling decay constant and z is the tip-sample separation. This strong dependence of current on distance renders STM sensitive to tip-sample separation as little as 0.01 Å. In STM, images are acquired in two main modes, constant current and constant height. In constant current mode, the tip is controlled by the feedback electronics to maintain a constant current between the tips and sample. The topographic data is therefore plotted as it scans over the surface. In constant height mode, the tip is held at a fixed height and voltage over the surface and the variations in the current is recorded as the tip rasters back and forth.

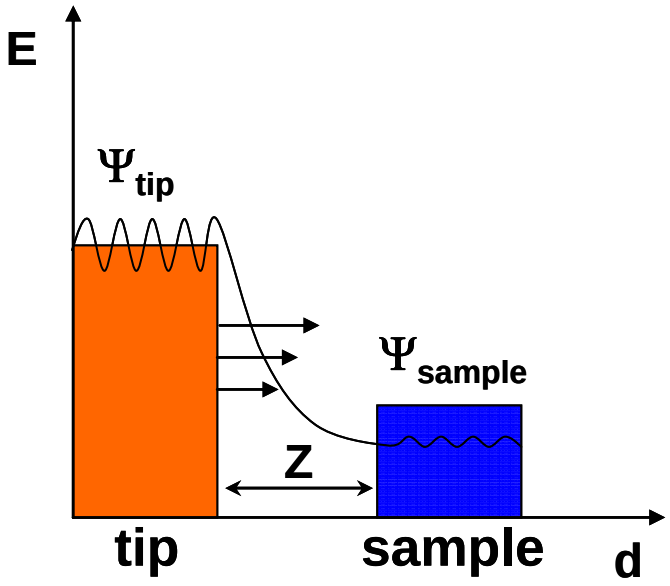

Figure 2.5. Schematic diagram of 1-D tunneling barrier.

CHAPTER III

CHARACTERIZATION OF A THIOL TETHERED TRI-PYRIDYL PORPHYRIN ON AU(111)

3.1. Synopsis

Porphyrins are actively studied for use in molecular and organic electronic components of devices due to their diverse, tunable optical and electronic properties. In this study mixed self-assembled monolayers (SAMs) of dodecanethiol and a tri-pyridyl porphyrin attached to a thiol tether via a perfluorinated phenyl ring, (TPy_3PF_4-SC_5SH) were prepared on Au(111) substrates. The synthetic strategy allows rapid formation of derivatives with different tethers. The surface structural and electronic properties of mixed monolayer SAMs of the porphyrin inserted into the dodecanethiol matrix were investigated using scanning tunneling microscopy (STM), atomic force microscopy (AFM), Fourier transform infrared reflection-absorption spectroscopy (FT-IRAS), and X-ray photoelectron spectroscopy (XPS). Density Functional Theory (DFT) calculations were also employed to evaluate the analytical vibrational frequencies of the TPy_3PF_4-SC_5SH molecule as well as its electronic structure. For the mixed monolayers, the morphology of the porphyrin molecules was probed by STM where it was found that the molecules assembled into domains of ~ 2 and 6 nm. AFM shows that the molecules protrude above the *n*-dodecanethiol layer by ~ 0.9 nm, while by STM, apparent heights of only ~ 0.5 nm were observed, suggesting limited tunneling efficiency. Stochastic switching of the porphyrin molecules was also observed during STM measurements in

the mixed monolayer and is likely associated with conformational changes within the monolayer since these molecules tended to insert near defects within the SAM.

3.2. Introduction

In recent years, thiol-derivatized molecules on gold substrates have been widely implemented for elaborate designs of molecular electronics.[55-58] The use of self-assembled monolayers (SAMs)[4] has been extensively employed for this development because of the relatively stable, two-dimensional, and densely packed structures that can be formed on metal or semiconductor surfaces through robust chemical bonds (e.g. Au-S, Si-O and Si-C bonds) as compared to Langmuir-Blodgett (LB) films[59] and lipid bilayers.[60] The electronic properties of single molecules or small groups of molecules have been studied by constructing different electrical testbeds, including electrical and mechanical break junctions,[61-65] cross-wire junctions,[66] nanopores,[67] mercury drop contacts,[68] conducting-probe atomic force microscopy (CP-AFM),[69,70] and scanning tunneling microscopy (STM).[65,71,72] STM is a powerful surface analysis technique, as it enables the observation of individual molecules with atomic resolution on surfaces. In addition to topographic details, STM images can elucidate details of the local tunneling probability as well as the electronic density of molecular orbitals (e.g. highest occupied molecular orbital, HOMO and lowest unoccupied molecular orbital, LUMO) participating in the tunneling process thus can influence the local transport behavior.

Although organic molecules with[73-76] and without[77-79] π-electron conjugated system have attracted considerable attention for in the potential manufacturing of

electronic devices down to the molecular level, highly π-conjugated molecules are of particular interest since the π-electron delocalization inside such molecules typically results in lower injection barriers and more efficient tunneling or electron transfer. Recent work in this aspect has been explored on polythiophenes,[80-82] oligo(phenylene ethynylene)s (OPEs),[83-85] oligo(phenylene vinylene)s (OPVs)[86] as well as phthalocyanines,[87] porphyrins[88,89] Re/Ru-bipyridyl molecules[90] and metal string complexes.[91,92] There have been a number of previous studies on porphyrins anchored to various substrates[93-97] because of their remarkably diverse photoelectrochemical, catalytic, electronic, and biochemical properties[98] that enable their use as active components of devices for applications including chemical sensors,[99,100] information storage,[101,102] and electrocatalytic or photocatalytic oxidations or reductions.[103,104] The relatively small HOMO-LUMO gap (ca. 2 eV) and the proximity of the HOMO states to the Fermi level of Au can be an advantage in many of these applications. In addition to single molecules, hierarchical assemblies of porphyrins self-organized by various strategies have also been explored as a means of creating light harvesting structures for energy conversion.[105-108]

Key in the implantation of hierarchical assembly of porphyrins for the construction of molecular based devices is the ability to readily create assemblies that can be reliably organized and attached to surfaces in high yields. In the work presented here, a free-base porphyrin macrocycle bearing three 4-pyridyl moieties and one pentafluorophenyl substituent in the *meso* positions was synthesized as a core platform for the rapid, high yield attachment of tethers that can be tailored to both the surface

chemistry and other properties. In the present case a terminal dithiolalkane replaces the 4-fluoro group to yield a derivative for immobilization onto a gold surface via strong sulfur-gold chemisorption (Figure 3.1). The work described herein is the first in a series of molecular systems being investigated by our groups for the creation of light harvesting and molecular/organic electronic devices. The pyridyl moieties provide a convenient attachment point for additional molecules via metal-ligand coordination chemistry, while the use of the fluorinated phenyl ring provides easy surface attachment group. Moreover, by controlling the extent of fluorination of this linker group, this phenyl ring, can be used as an internal barrier to control the tunneling between the pyrrole macrocycle and the thiol tether. This barrier can be modulated by systematic variation of the number and position of the fluoro groups on the ring, thus affording some control of the relative orbital energies of this phenyl group and the degree of steric interactions between the 2,6-positions on this phenyl group with the pyrrole β-hydrogens. Thus, control of these interactions provides a means to dictate the electronic coupling between the macrocycle and the tether.

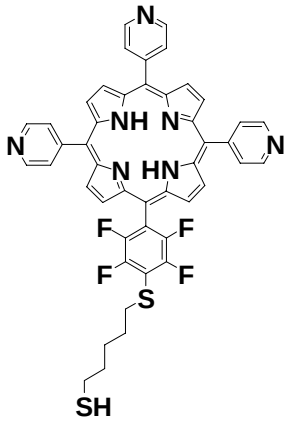

Figure 3.1. Chemical structure of TPy_3PF_4-SC_5SH.

In this work the tri-pyridyl porphyrin with the fully fluorinated ring has been explored. In addition to the synthesis, we describe the preparation and characterization of mixed monolayers of the thiol tethered porphyrin inserted into a pre-assembled *n*-dodecanethiol monolayer on gold surfaces. The surface assembly has been characterized utilizing STM, AFM, X-ray photoelectron spectroscopy (XPS), and Fourier transform infrared reflection absorption spectroscopy (FT-IRAS).

3.3. Experimental Details

Materials. Self-assembled monolayers were prepared on Au films, including Au(111) on mica (Molecular Imaging-Agilent, Phoenix, AZ) and on evaporated Au films on Si. Au films on Si substrates were prepared by thermal evaporation onto single-side polished Si(100) wafers (Virginia Semiconductor Inc.) in a bell-jar evaporator (BOC Edwards, Auto 306). The chromium (5 nm) and gold (200 nm) films were deposited under vacuum ($p < 2.0 \times 10^{-6}$ Torr) at the rate of 0.5 and 3 Å/s, respectively. Dodecanethiol (DDT) was purchased from Aldrich (98% purity) and used as received.

Synthesis of Porphyrin Thiol Compound. 5,10,15-tri(4-pyridyl)-20-(4-(1',5'-dithiopentyl)-2,3,5,6-tetrafluorophenyl) porphyrin (TPy_3PF_4-SC_5SH) was synthesized in two steps. First, a mixed aldehyde condensation in propionic acid using one equivalent of pentafluorobenzaldehyde, three equivalents isonicotinaldehyde and four equivalents pyrrole yields a statistical mixture of compounds that are readily separated by flash

chromatography.[109] The 4-fluoro group of the target 5,10,15-tri(4-pyridyl)-20-perfluorophenylporphyrin (15mg, 21.2 mmol), was reacted with 1,5-dithiopentane (25mL, 180.5) mmol and diethyl amine (60mL, 580 mmol) in a solvent mixture of DMF, chloroform and methanol (4:4:1 v/v, 3mL) in the dark under nitrogen at room temperature for 24h. After evaporation of the solvent at reduced pressure, the crude product was purified by flash silica gel column chromatography with a 97% CH_2Cl_2 / 3% CH_3OH (v/v) eluent. The major fraction was collected and subjected to one more column purification with the same solvent system (yield 13.8mg, 79% based on compound 1). UV- visible in CH_2Cl_2 (λ_{max} nm (rel. intensity): 416 (100), 511 (9.28), 544 (3.85), 585 (6.25) and 640 (2.39). NMR (500MHz, $CDCl_3$):δ = 9.10 (d, J = 6.3 Hz, 6H), 8.91 (m, 8H), 8.20 (m, 6H), 3.31 (t, 2H), 2.67 (m, 2H), 1.91 (m, 2H), 1.79 (m, 4H), 1.45 (t, 1H) and –2.81 (s, 2H). UV-Vis ($CHCl_3$): 416, 511, 544, 585 and 640. ESI-MS: 824 (MH^+).

Preparation of Mixed Monolayers. Au(111) substrates (purchased from Molecular Imaging Inc.) were ~150 nm flame-annealed gold films on mica. Before each experiment, all substrates were treated with UV/ozone for 20 min, followed by rinsing the gold film in sequence with high purity (18.2 MΩ•cm) water (NANOpure Diamond, Barnstead), ethanol, and dried with streaming nitrogen. SAMs of *n*-dodecanethiol were formed by immersion of the Au films in 1 mM *n*-dodecanethiol in ethanol for 24 h. After rinsing liberally with ethanol, the substrates were soaked in 0.5 mM porphyrin thiol dissolved in dichloromethane for five days to allow the insertion of the porphyrin

molecules into *n*-dodecanethiol matrix. After insertion, the substrates were removed from the solution and were rinsed with dichloromethane and blown dry with streaming nitrogen.

Scanning Tunneling Microscopy. STM measurements were taken both in air and under ultrahigh vacuum (UHV) conditions. STM measurements in air were carried out with a NanoScope IIIa (Veeco Metrology Group, Santa Barbara, CA) using a low-current scanning head under ambient conditions. High resolution images were collected under UHV conditions using an Omicron UHV-XA STM system. The system was operated with a typical base pressure of $< 3 \times 10^{-10}$ Torr. Images were collected using Pt/Ir (70/30) tips which were mechanically cut. The typical imaging conditions of tunneling current and tip bias voltage ranged from 10 pA to 200 pA and from +500 mV to +1.5 V, respectively. Current-voltage (I-V) spectra were collected under UHV conditions over a voltage range of -2 V to + 2 V.

Atomic Force Microscopy. AFM images were acquired with a Molecular Imaging 4500 Pico SPM (Agilent, Phoenix, AZ) with a deflection-type detection scanning head interfaced with an SPM1000 control electronics Revision 8 (RHK Technology Inc., Troy, MI). All AFM images were acquired in contact mode under ethanol using commercially available Si_3N_4 AFM tips (Veeco/TM Microscopes, Sunnyvale, CA) with nominal tip radii of ~ 10 nm and nominal spring constants ranging from 0.03-0.1 N/m.

X-ray Photoelectron Spectroscopy. XPS data were acquired with a Kratos Axis ULTRA X-ray photoelectron spectrometer equipped with a 165 mm hemispherical electron energy analyzer. The incident radiation was the MgKα X-ray line (1253.6 eV) with a source power of 180 W (15 kV, 12 mA). The analysis chamber was maintained at a steady base pressure of $<6 \times 10^{-9}$ Torr during sample analysis. Survey scans of up to 1100 eV were carried out at a analyzer pass energy of 160 eV with 1.0 eV steps and a dwell time of 300 ms. Multiplexed high resolution scans (Au 4f, C 1s, S 2p, N 1s, and F 1s) were taken at a pass energy of 40 eV with 0.1 eV steps and a dwell time of 60 ms. The survey and high resolution spectra were obtained with averages of 5 and 50 scans, respectively. The Au 4f peak at 84.0 eV was set as a reference for all XPS peak positions to compensate for energy shifts due to the spectrometer work function. The fitting of high-resolution sulfur peak was executed by utilizing XPSPEAK 6.1 in which a Shirley-type background[110] (from ~159 eV to ~168 eV) with an 80% Lorentzian-Gaussian curve-fitting program were used. The spin-split doublets of the S(2p) were fitted by fixing the area ratio at $2p_{3/2}$:$2p_{1/2}$ = 2:1 and setting their energy difference to 1.2 eV. The full width half-maximum of each peak was also maintained at a constant value.

FTIR Spectroscopy. Transmission IR spectra of the solid porphyrin compounds were obtained in KBr pellets. FTIR spectra of the mixed monolayers were collected on evaporated Au films on Si. Reflection-absorption spectroscopy was collected using an FT-IR spectrometer (Nicolet 6700, Thermo Electron Corporation, Madison, WI)

equipped with a liquid nitrogen-cooled HgCdTe (MCT) detector. FTIR data were acquired in single reflection mode with polarized light generated by a ZnSe polarizer adaptor (FT-80, Thermo Electron Corporation). The light path, MCT detector, and sample chamber were purged with dry nitrogen during the measurements. An UV/ozone cleaned gold substrate was used as the reference. The IR spectra were collected with a total of 1024 scans of both the sample and the reference at 4 cm^{-1} resolution.

3.4. Results and Discussion

FTIR Measurements. The IR spectra of TPy_3PF_4-SC_5SH calculated by DFT and prepared in KBr pellets are presented Figure 3.2A and 3.2B, respectively. The molecules in KBr pellets are ground thoroughly and thus presumably exhibit isotropic orientation. Figure 3C displays the infrared reflection absorption spectroscopy spectrum of porphyrin thiol/dodecanethiol mixed monolayers on Au. The observed peak frequencies and vibrational modes were assigned based on the calculations and previously reported literature[94,97,111,112] and are summarized in Table 3.1.

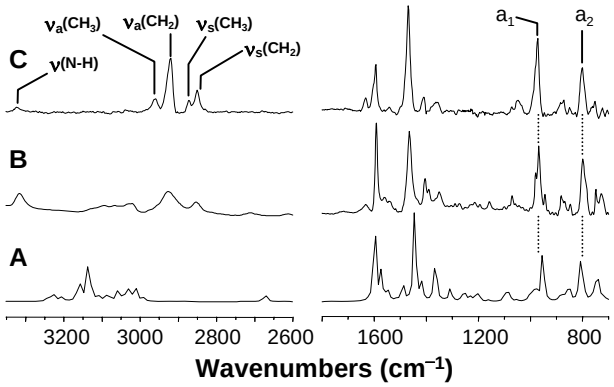

Figure 3.2. IR spectra of TPy3PF4-SC5SH (A) calculated by TPSS and (B) prepared in KBr pellets; and IRAS spectrum of (C) TPy3PF4-SC5SH/dodecanethiol mixed SAMs.

Table 3.1. Peak assignments for the porphyrin thiol in KBr Pellets, in monolayers mixed with dodecanethiol and TPSS calculations. [a]The peak intensity is negligible. [b]Calculated with density functional theory TPSS/6-31G+(d').

peak position (cm^{-1})			
in KBr	**in mixed SAMs**	**DFT[b] calc.**	**vibrational mode**
3316	3318	3470	ν(N-H), stretching
-----[a]	2964	-----[a]	$\nu_a(CH_3$, ip), asym stretching
-----[a]	2936	-----[a]	$\nu_s(CH_3$, FR), sym stretching
2926	2919	3058	$\nu_a(CH_2)$, asym stretching
-----[a]	2877	-----[a]	$\nu_s(CH_3)$, sym stretching
2853	2850	3010	$\nu_s(CH_2)$, sym stretching
2533	-----[a]	2663	ν(SH)
1592	1593	1603	ν_{8b}(C=C), in-plane stretching
1465	1468	1447	ν_{19a}(C=C), in-plane stretching
1069	1045	1077	ν_{18b}(CH), in-plane bending
968	969	970	pyrrole breathing
798	~791	800	ν_{11}(CH), out-of-plane bending
~726	723	729	pyrrole deformation

A proposed model of the porphyrin thiol derivative embedded in *n*-dodecanethiol SAMs tilting away from the surface normal by ~ 30^o is illustrated in Figure 3.3, where the in-plane pyrrole ring breathing mode, a_1, and out-of-plane pyrrole C-H bending mode, a_2, are sketched. The tilt angle of the porphyrin macrocycle (α) with respect to the surface normal can be derived from the intensity ratio of these two transition dipoles. The observed disappearance of the ν(SH) mode at 2534 cm^{-1} confirms the formation of S-Au covalent bonds. The absorptions between 2800 and 2965 cm^{-1} are *n*-alkyl stretch modes ($\nu(CH_2)$ and $\nu(CH_3)$ originating from dodecanethiol matrix and the porphyrin thiol alkyl tether). The corresponding vibrational peaks for the in-plane and out-of-plane contributions from the porphyrin thiol pyrrole moieties (a_1 and a_2, respectively) are denoted in Figure 3.3 for deducing the molecular tilt angle of the thiol-derivatized porphyrin SAMs.

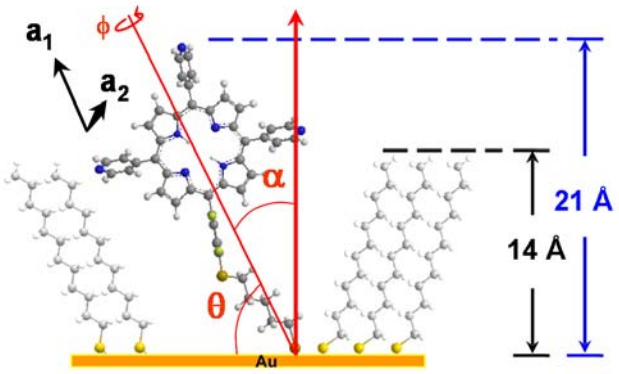

Figure 3.3. Proposed binding scheme of TPy_3PF_4-SC_5SH inserted into n-dodecanethiol SAMs and corresponding in-plane (a_1) and out-of-plane (a_2) dipole vectors of porphyrin macrocycle.

The increase of intensity ratio of I_{a1}/I_{a2} in the mixed monolayers (Figure 3.2C) as compared with the KBr pellets (Figure 3.2B) suggests that the porphyrin macrocycle orients at a certain angle relative to the surface normal rather than lying flat on the Au surface according to the surface dipole selection rule[113] in which the dipole moments perpendicular to the metallic substrates can be enhanced, while those parallel to the substrates will be cancelled out. Based on the intensity ratios of the orthogonal vectors of I_{a1}/I_{a2} in mixed monolayers versus the isotropic KBr sample, the average tilt angle (α) was determined to be ~ 39.0^o relative to the surface normal.[114] The value of the average azimuthal tilt angle was obtained by assuming that the rotation angle (ϕ) around the main molecule axis was 0^o and the porphyrin ring was planar which is in accordance with the results of theoretical calculation (*vide infra*). Although the rotation angle might vary from 0^o, the value of the calculated tilt angle is not affected much by the variation of rotation angle. If the relative isotropic intensity, I_{a1}/I_{a2}, from the calculated spectrum is

used in place of the experimentally measured KBr sample, the tilt angle of the macrocycle in the mixed monolayers would be similar at ~ 41.0^{o}.

X-ray Photoelectron Spectroscopy. A representative survey spectrum of the porphyrin thiol/dodecanethiol mixed monolayer is shown in Figure 3.4. High-resolution spectra of the C(1s), N(1s), and F(1s) regions show peak binding energies of 284.8 ± 0.1, 399.0 ± 0.1 and 687.0 ± 0.1 eV, respectively, while the high-resolution S(2p) signal can be fitted into two sets of doublets from the S($2p_{3/2}$) and S($2p_{1/2}$) components split by 1.2 eV. The two S($2p_{3/2}$) peaks are centered at 162.1 ± 0.1 and 163.7 ± 0.1 eV, respectively (Figure 3.5). The first type of sulfur corresponds to the thiol chemisorbed onto the gold substrate,[115] while the second at higher binding energy can be attributed to the presence of the S coordinated to the tetrafluorophenyl ring.[103] The experimentally determined value of F:N atomic ratio is consistent with the expected 4:7 stoichiometry within a deviation of 10-15% which demonstrates that the integrity of the porphyrin thiol molecules is retained after insertion into the *n*-dodecanethiol matrix.

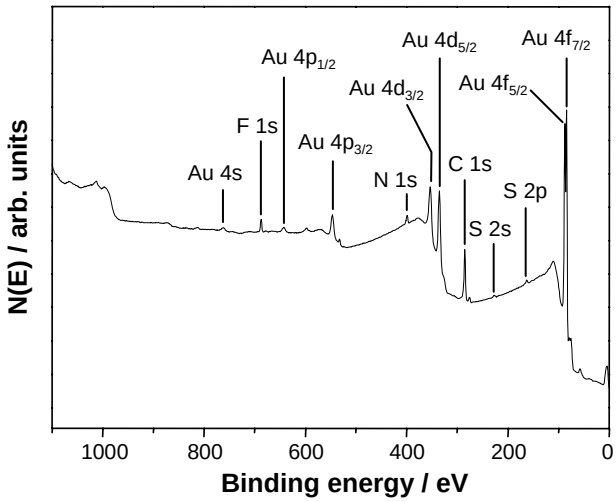

Figure 3.4. X-ray photoelectron survey spectrum for TPy3PF4-SC5SH/dodecanethiol mixed monolayers on Au (111).

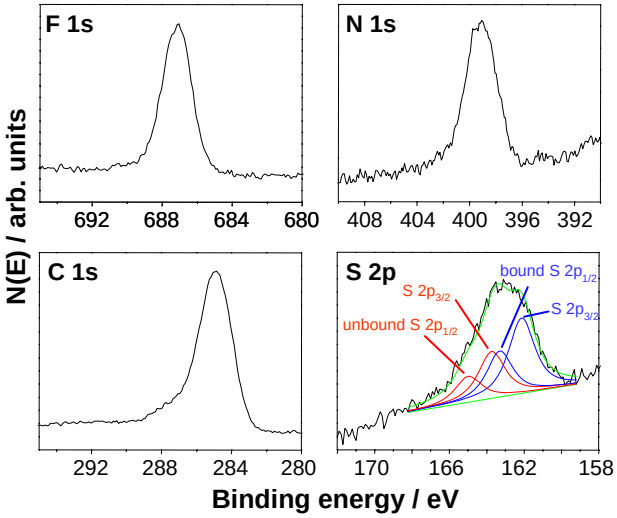

Figure 3.5. High-resolution XPS for TPy3PF4-SC5SH/dodecanethiol mixed SAMs, showing the F 1s, N 1s, C 1s, and S 2p spectral regions.

Surface Imaging. In order to examine the surface structure of the inserted porphyrin molecules, both atomic force and scanning tunneling microscopies were employed. AFM images of the mixed monolayer show clusters inserted into the

dodecanethiol matrix, suggesting that the porphyrin molecules are sticking up out of the dodecanethiol background. Based on the physical heights determined from contact mode images in ethanol, the porphyrins were observed to extend above the dodecanethiol SAM anywhere from 0.5 nm to 2 nm (Figure 3.6A). The variation in heights is likely due to differences in bonding location, such as near defects or step edges in the film. The average measured height difference was found to be ~ 0.9 nm, which is consistent with the average structure illustrated in Figure 3.2 as deduced from the FTIR data, in which the porphyrin macrocycle is tilted ~ 39^{o} away from the surface normal. Due to the large size of the AFM tips used (ca. 10 nm) sufficiently high resolution images however were not possible by AFM to detail the molecular organization of the dodecanethiol matrix. As such, scanning tunneling microscopy was employed to obtain molecular resolution images of the mixed monolayer films.

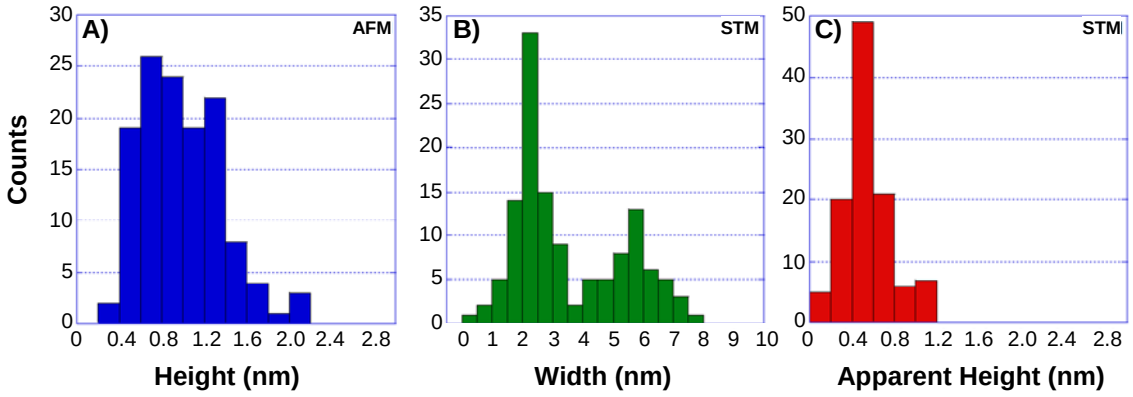

Figure 3.6. Height and domain size distributions from AFM and STM measurements. (A) Physical height difference between the dodecanethiol and porphyrins deduced from AFM images in ethanol. (B) Domain size histogram and (C) apparent height distribution for the ON conductance state of TPy3PF4-SC5SH embedded in *n*-dodecanethiol SAMs from UHV-STM (Vbias = 1.4 V, Itunnel = 20 pA).

STM images of the dodecanethiol matrix on the Au(111) surface shows the close-packed structures typically observed for alkanethiols that have been previously reported[116-118] (Figure 3.7). When the porphyrins are inserted into the SAM, they are found to organize next to and into defects in the film and appear as bright unresolved clusters. From the examination of a number of self assembled mixed monolayers, the clusters are found to form two predominate average domain sizes of ~ 2 nm and ~ 6 nm in width (Figure 3.6B). The ~ 2 nm domains are likely single inserted porphyrins whose physical width from pyridyl-pyridyl group is ~ 1.5 nm, convoluted with the STM tip shape,[119,120] or broadened by thermal motion, while the ~ 6 nm domains are porphyrin aggregates (likely 3-5 molecules) which tend to have strong π–π coupling between macrocycles. This distribution is observed when imaging either in air or under UHV conditions. Interestingly, all of these domains show similar apparent heights of 0.5 nm on average relative to the dodecanethiol matrix. The apparent height distribution for these porphyrin thiol domains is displayed in Figure 3.6C. This apparent height is nearly half that of the observed physical height deduced from AFM images of the same samples and suggests that the barrier to tunneling within the molecules is significant.

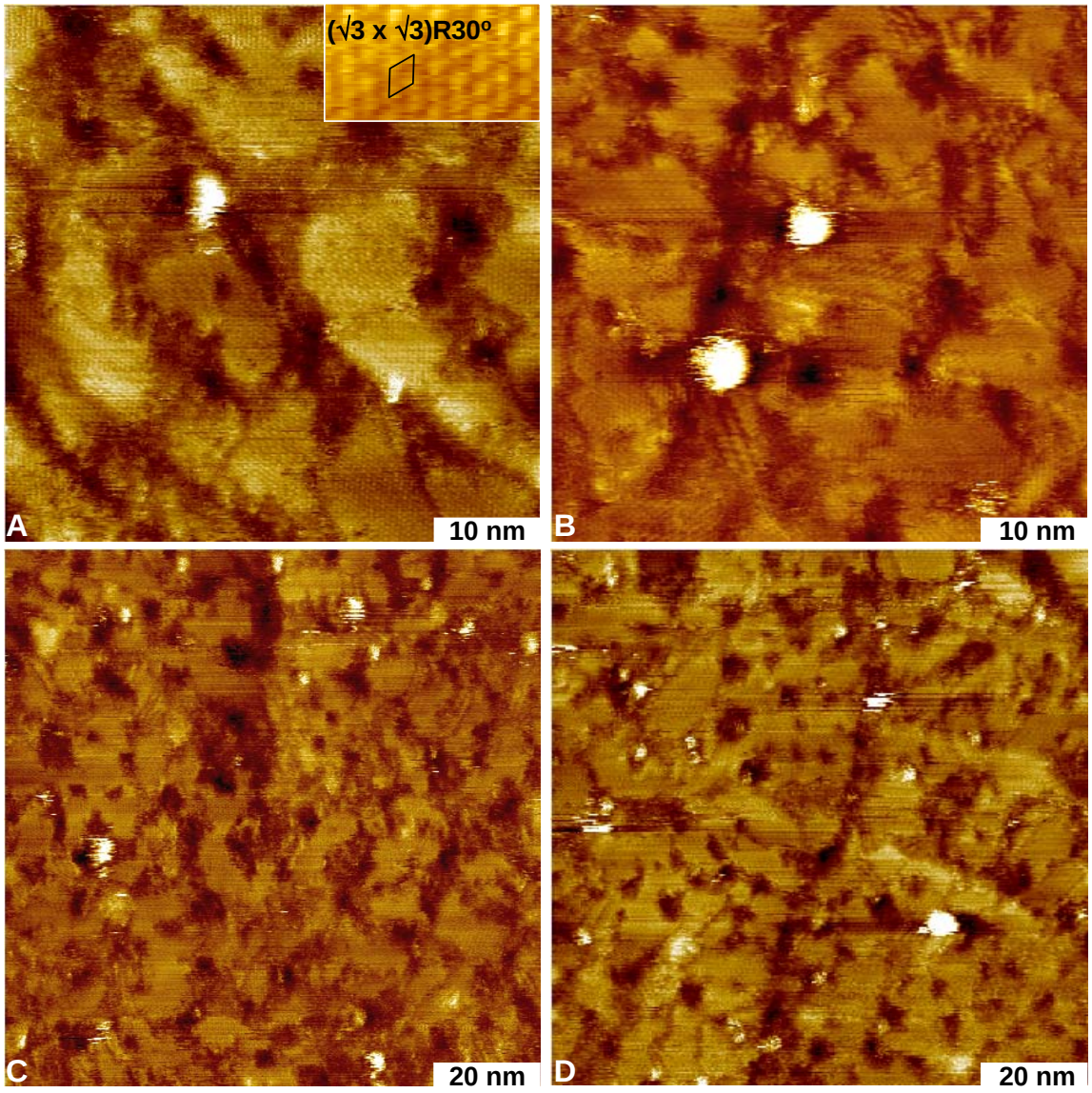

Figure 3.7. UHV-STM images of TPy3PF4-SC5SH molecule(s) isolated within n-dodecanethiol matrix on Au(111) under UHV conditions. Imaging size: (A) 50 x 50 nm, (B) 50 x 50 nm, (C) 100 x 100 nm, and (D) 100 x 100 nm; imaging conditions: Vbias = 1.4 V, Itunnel = 20 pA. The inset in (A) magnifies the (√3 x √3)R30o lattices for n-dodecanethiol SAMs.

Comparing the physical height as deduced from AFM measurements to the observed height in the STM, the electron tunneling decay constant, β, for the porphyrin thiol can be estimated using a two layer tunnel junction model[73,121,122] assuming that the

contact conductance between the two molecules is essentially equivalent. Based on this assumption, the decay constant for the porphyrin thiol can be estimated from the apparent height difference as follows:

$$\beta = [\beta_{DDT} h_{DDT} - \alpha(\delta h_{STM} - \delta h)] / h_{por},$$

where β_{DDT} is the tunneling decay constant for dodecanethiol (1.2 $Å^{-1}$), h_{DDT} is the physical thickness of the dodecanethiol layer (~ 14 Å, based on a molecular tilt angle of 30°), α is the decay constant between the tip and molecule in vacuum, (~ 2.3 $Å^{-1}$), δh_{STM} is the apparent height difference determined by STM, and δh is the height difference deduced by the AFM topographic data, h_{por} is the physical height of the porphyrin thiol as deduced by AFM and FTIR measurements. Utilizing this formalism, the tunneling constant β for the porphyrin thiol was estimated to be ~ 1.4 $Å^{-1}$. This β value is consistent with current-voltage (I-V) spectroscopy measurements (Figure 3.8) of the dodecanethiol SAM compared to the inserted porphyrins, which show similar current values over the range of bias probed from (-2 V to +2 V) despite the conjugated nature of the porphyrin moiety and the potentially low injection barrier as suggested from DFT calculations, which places the HOMO ~ 0.2 eV below the Fermi level for Au (~ 6.1 eV). This high β value suggests that the tunneling in this molecule is ultimately dominated by the alkyl tether which binds the molecule to the surface, which has been seen previously for other systems,[122] and is consistent with the alkyl tether decoupling the macrocycle from the surface, as has been seen for napthyl compounds by 2-photon photoemission.[123]

There is also likely a contribution from the lack of orbital overlap between the porphyrin macrocycle and the alkyl tether due to the orientation of the tetrafluorophenyl ring coupling the two and we are in the process of systematically investigating how changing the chemistry and orientation of the phenyl ring influences the conduction properties.

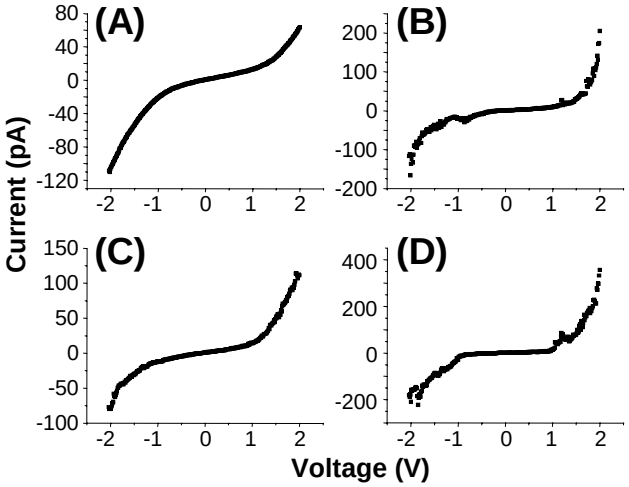

Figure 3.8. I-V spectra (averaged from 50 curves each) for the (A) dodecanethiol matrix, (B) small (~ 2 nm) porphyrin domains and (C, D) large (> 6 nm) porphyrin domains.

Current-voltage (I-V) curves from the small (ca. 2 nm) and large (~ 6 nm) domains show some distinct differences (Figure 3.8). The single molecules show a roughly symmetric I-V curve, as compared to that of dodecanethiol, with an upturn in current flow around -1 V and + 1.5 V. When examining the I-V curves for the larger aggregates (Figure 3.8C and 3.8D), the upturn in current appears nearly symmetrically at ± 1 V. Moreover, two families of I-V curves appear, one with a distinct current blockade and one without. This may be due to local intermolecular interactions shifting the HOMO-LUMO levels as is typically observed during the formation of H and J

aggregates for porphyrins.

In addition to their relatively low conductance, the inserted porphyrins show the phenomenon of stochastic switching[71,124-126] whereby the molecules in the "ON" state exhibit several Å's of apparent height protrusion relative to the surrounding alkanethiol matrix, while the "OFF" state shows little to no contrast from the host matrix (Figure 3.9). Such "ON/OFF" conductivity switch-like behavior has been explored both theoretically and experimentally to be associated with orientation changes of the molecules,[127,128] interactions among neighboring molecules,[129] reduction of functional groups,[130] bond-fluctuation,[125,131] and changes in molecule-substrate bond hybridization.[71,132] Weiss et al. has demonstrated how controlling the rigidity of the local matrix in which the molecules are implanted may be used to influence switching behavior arising from molecular orientation dynamics.[126]

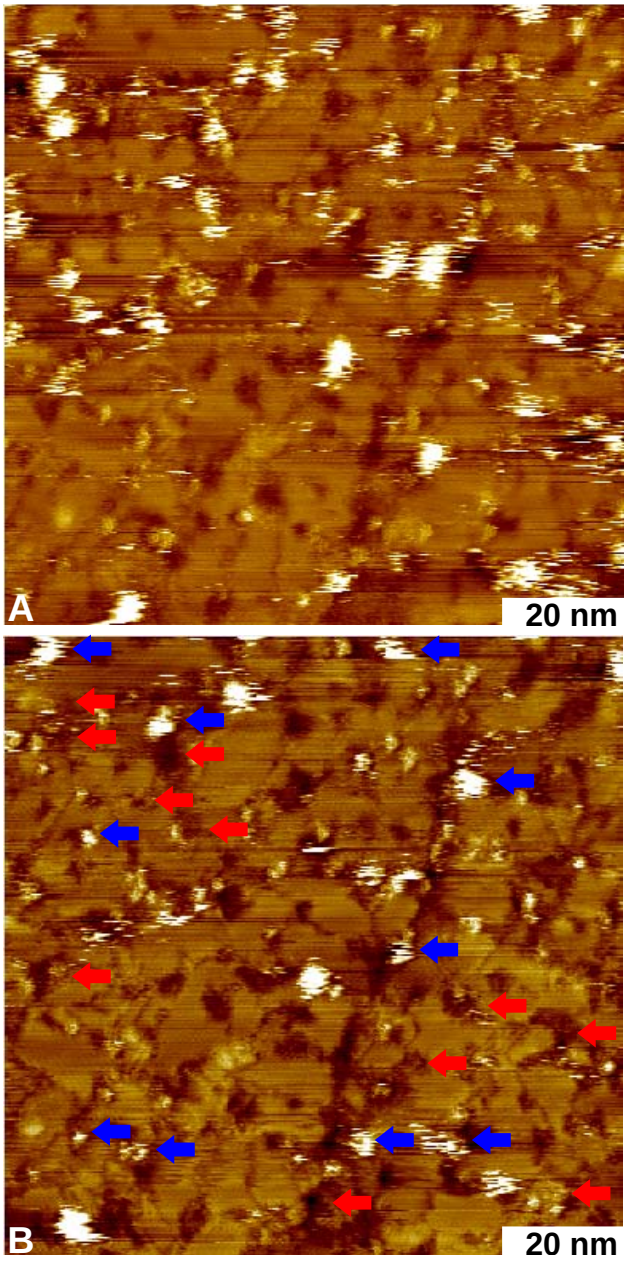

Figure 3.9. Representative STM images for ON and OFF switching behavior of TPy3PF4-SC5SH. The red arrows in (B) indicate the OFF conductance state switching from the ON conductance state in (A), while the blue arrows exhibit the ON state turning from the OFF state in (A). Total measurement time = 8.2 minutes, 100 x 100 nm, Vbias = 1.4 V, Itunnel = 20 pA.

Unlike many previous examples, the switching behavior that we observe generally occurs only a few times for each molecule or cluster of molecules. In fact, after extended periods of imaging a region, virtually no porphyrins are further observed within the scan area. Upon expanding the scan area, clusters are again observed, but only outside the region that had been previously imaged. This suggests that the molecules are either removed from the surface, chemically altered by oxidation or reduction, or that an irreversible conformational change has occurred that renders them undetectable by STM in their new conformation. The redox pathway is unlikely because the first two oxidations and reductions of the porphyrin macrocycle are reversible under UHV conditions. While the majority of the inserted molecules appear near defects in the SAM layer, even those that have been found in the center of well ordered domains show "switching" behavior. As such, the dodecanethiol near the porphyrins may be more disordered than can be deduced simply from the STM images, due to the bulkiness of the macrocycle impeding imaging directly near the inserted molecules, and still enables local conformational changes in the inserted molecule.

3.5. Summary

Tri-pyridyl porphyrin compounds have been attached to Au surfaces by a thiol tether, through a tetrafluorophenyl linker. The use of the fluorinated linker provides a facile means of attachment to any dithiol tether. When inserted into a background matrix of dodecanethiol, the porphyrins are observed to tend to bind near the edges of defects within the alkanethiol layer as either single molecules or small ensembles (ca. 3-

5 molecules). Based on the apparent height of the molecules relative to the dodecanethiol matrix, the tunneling efficiency was found to be low, similar to that of a simple alkanethiol which is considered a molecular insulator. From DFT calculations, the low tunneling efficiency can be attributed to the lack of effective orbital overlap between the frontier orbitals of the porphyrin macrocycle and the thiol tether due to the orthogonal dihedral angle between the porphyrin ring and the perfluorophenyl linking group. In addition to the electronic effects on the phenyl ring, the 2,6 fluoro moieties increase the rotation barrier and diminish the dynamics of the aryl – porphyrin bond. Thus, this group introduces an effective tunneling barrier directly within the molecule reducing the tunneling efficiency, despite of the close proximity of the HOMO of the molecule to the Au Fermi level. Future studies will examine how selective removal of the fluorine groups from the tether can be used to tune the tunneling properties by both electronic and steric interactions. Also, once attached to the surface, additional porphyrin rings will also be coordinated to this compound via metal-ligand coordination to create energy harvesting structures.

CHAPTER IV

SOLUTION ENHANCED NANOPATTERNING OF GAAS BY SCANNING PROBE LITHOGRAPHY

4.1. Synopsis

Scanning probe lithography has been employed to pattern GaAs(100) surfaces in aqueous solution conditions via enhanced chemical etching and with directed assembly of alkylthiols. By varying the applied loads on the cantilever/tip and selecting solutions with varying pH from 3 to 11, nanowells with depths from a few nm up to 100's of nm can be formed. Using nanoshaving and nanografting approaches, thiolate monolayers self-assembled on the GaAs(100) surface can also be patterned. These approaches can be applied to the directed fabrication of nanoscale electronic and optical architectures using scanning probe methods.

4.2. Introduction

Due to its wide application in opto-electronic and photonic devices, and its arising interest in plasmonic devices, it is becoming extremely important to pattern GaAs surface on the nanometer scale with precisely controlled size, geometry, and depth. A variety of techniques have been employed to pattern GaAs surface. Focused-ion beam (FIB) has been widely used to pattern semiconductors, like Si and GaAs surfaces. However, this technique is generally a destructive method to generate patterns directly on the surface with small lateral dimensions;[133] and the major concern is the sputtered

material redeposition and incident ion beam contamination occurred during FIB patterning.[134] Though FIB-assisted Cl_2 etching has been proved to be a useful maskless technique for patterning GaAs,[135,136] the optical and electrical properties can also be severely degraded by the ion-induced damage during etching.[137,138] Furthermore, ions with kinetic energy of only a few hundred eV can introduce damage up to hundreds of nm deep into the surface.[139,140] Thiols self-assembled on GaAs surface, especially those long chain monolayers, exhibit highly oriented, uniformly densely packed, robust, and protective structures, as being recently characterized by X-ray photoelectron spectroscopy (XPS),[141] attenuated total reflection Fourier-transform Infrared spectroscopy (ATR-FTIR),[142] atomic force microscopy (AFM), IR and near edge X-ray absorption fine structure (NEXAFS).[143] Furthermore, it has been reported that SAMs can be degraded and patterned by ultraviolet (UV) light, and therefore can be utilized as a lithographic template.[144] Therefore, despite the fact that thiols self-assembled on GaAs is nearly 2 orders of magnitude slower than on Au,[143] octadecanethiol (ODT) film has been utilized as a sensitive self-developing positive resist and a durable masking layer for chemical etching of GaAs, producing patterns with a depth of ~ 30 nm, where electron beam was employed instead of UV.[145] Meanwhile, PDMS stamps have been employed to pattern GaAs surface with dithiol film followed by wet chemical etching to produce nanowells on this semiconductor surface.[146]

Recently, scanning probed lithography has been applied to pattern various surfaces on the nanometer scale.[147-152] With conductive tips, nanopatterns have been successfully created on different metal surfaces including GaAs by local

oxidation.[147,150,152] The disadvantage is that the oxide patterns created by the conductive tip is often dependent on the environmental condition, for example humidity, and is less than 6 nm thick.[150] Atomic force microscopy (AFM) has also been employed to directly write patterns on a GaSb mask of InSb semiconductive surface, followed by wet chemical etching.[149] Though the mask layer can be removed by wet etching, the depth and width of the patterns transferred from the mask layer during wet etching depend on the etching chemicals and the etching time. Therefore, it is difficult to control the patterns dimensions. Conductive AFM lithography has previously been used to produce local oxide nanopatterns on GaAs surface in air; by removing the oxide, nanowells were produced on the GaAs surface.[151] In the mean time, cantilever oscillation of AFM has been employed to created nanopatterns on GaAs possessing a depth of less than 4 nm.[148] It is generally difficult to pattern samples by direct scratching using SPL technique, especially hard surfaces, because the applied load must exceed the threshold force. For example, a force higher than 100 nN is required to pattern GaSb surface results nanostructures ~ 5.0 nm deep.[149]

4.3. Results and Discussion

In this paper, we describe a very simple and convenient method to directly pattern GaAs(100) surface on the nanometer scale with scanned probe lithography (SPL) in aqueous solutions. By selecting solutions with different pH (DI, NH_4OH, and HCl) and varying the applied loads, nanowells with controlled depth range from several nm to submicron can be created on GaAs surface. The patterning of thiol modified GaAs

surface will also be introduced, aiming to anchor metal nanostructures on GaAs surface to fabricate photonic, plasmonic, and molecular devices. As being reported, peptide molecules have been successfully patterned on GaAs surface with dip-pen nanolithography, exhibiting a crystalline-like and interchain hydrogen bonding structures.[153] With the aid of dithiol molecules, the junction of Au-molecule-GaAs has been investigated.[154,155] Meanwhile, gold nanopatterns have been created on dithiol modified GaAs using a PDMS stamp.[156] The experiments were carried out with an AFM system (Molecular Imaging Pico, Phoenix AZ) with a SPM 1000 controller (RHK Technology, Troy MI). Prior to the experiments, GaAs sample was etched in NH_4OH for 3 minutes, rinsed in ethanol, and dried by nitrogen. Thiols were self-assembled on the freshly etched GaAs in 3mM octadecanethiol/dodecanethiol of ethanol solution for 24 hours following procedures described in reference.[143] Infrared spectrum showed that the films exhibit very well ordered structures (data not shown here). Si_3N_4 tip/cantilever assemblies possessing a typical spring constant of 0.5 N/m were conducted in these experiments.

As the Si_3N_4 tip scanned on GaAs surface with an applied load, the tribochemical process induced local oxidation, and the oxide GaAs was then removed by the solution generating nanopatterns on the surface. After patterning, the surface was immediately imaged with the same tip at a force less than 10 nN. Fig. 4.1(a) and (b) demonstrate nanopatterns on GaAs substrate created with an applied load of 37.8 nN in NH_4OH solution with a ph of 10 and 11 respectively. The spacing between each line during patterning is 1 nm, and the dimension of each pattern is 200 nm × 200 nm. The cross-

sectional plots (Fig. 4.1(c) and (d)) across the GaAs surface show that the nanowells possess depth of ~ 13 nm and 43 nm, corresponding to ph of 10 and 11 respectively. Because the cone-shape tip and tip-surface convolution, all the nanowells exhibit narrow down structures. The nanowells created with a line spacing of 0.5 nm have also been investigated. Fig.4.2 shows nanowells produced in HCl and NH_4OH solution possessing a pH of 3 and 10 respectively. Fig.4.3 illustrates the average depth of nanowells patterned on GaAs surface by SPL as a function of applied loads, in HCl, DI, and NH_4OH solution with pH from 3, 6, to 10 and 11. Depth of nanostructures increases with the increasing load in the same solution. Overall, nanopatterns generated in NH_4OH solution (pH 11) is much deeper than other solutions with the same applied load, while in DI water the depth nanowells is only several nm even at high load. The roughness of etched GaAs surface and SAMs on GaAs was measured by AFM as shown in Fig. 4.4. Nanopatterning of SAMs on GaAs in ethanl of two different pH values was perfomed as shown in Fig. 4.5, demonstrating that deeper nanostrcutures on thiol modified GaAs surface can be created under a basic solution.

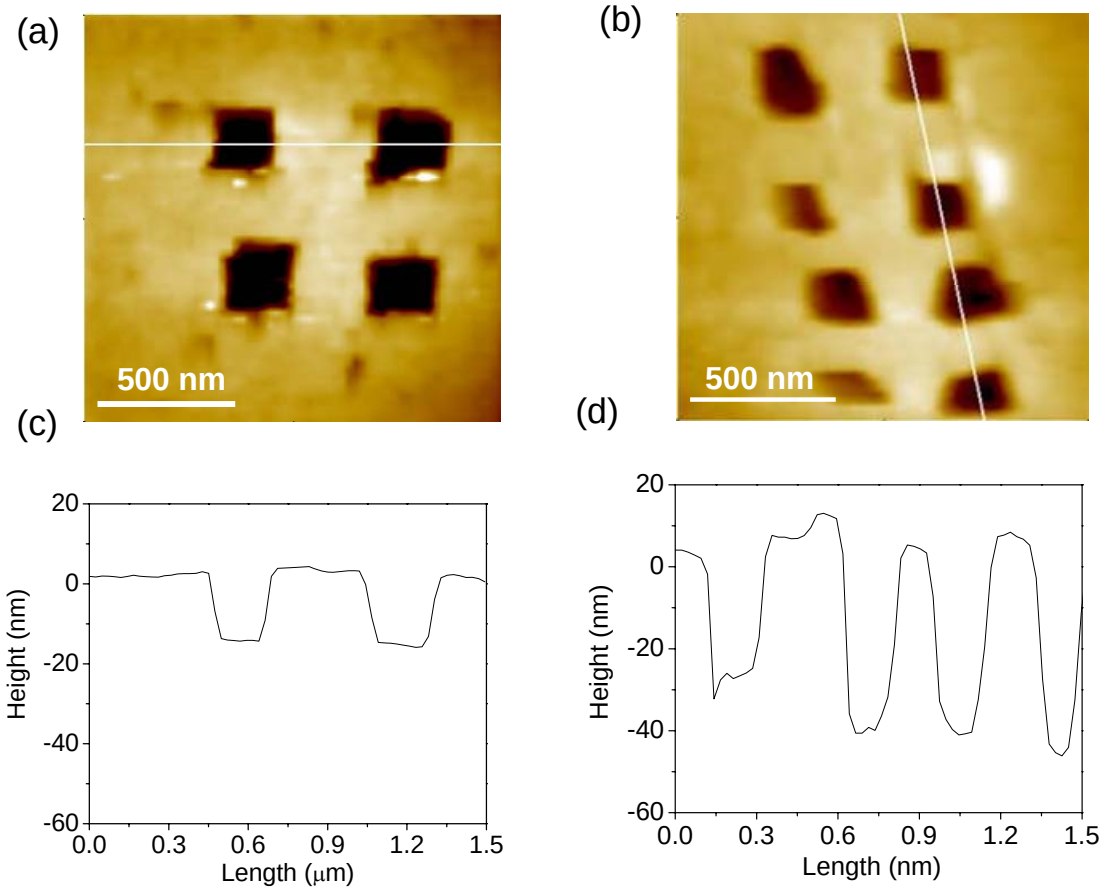

Figure 4.1. The AFM images of the patterns created on GaAs surface in NH_4OH with a pH of 10 (a) and 11 (b). The line spacing during scanning is 10 nm; (c) and (d) the cross-sectional plots correspond to lines in (a) and (b) portray the nanostructures dimension and depth.

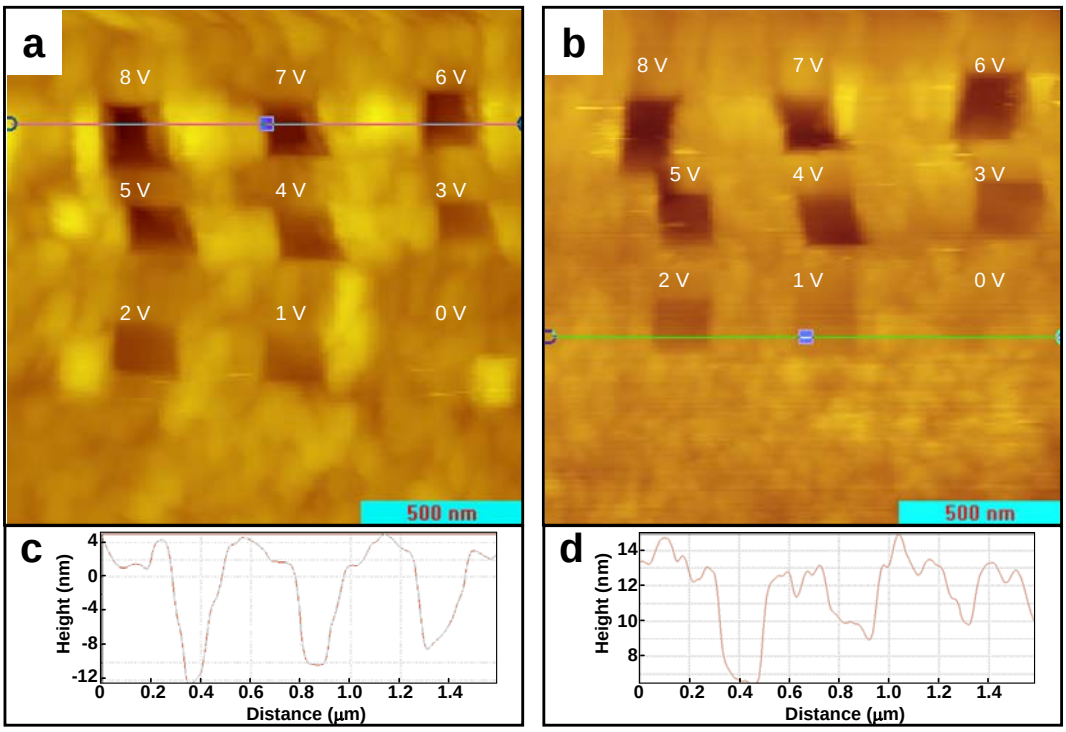

Figure 4.2. The AFM images of the patterns created on GaAs surface in HCl and NH_4OH with a pH of 3 (a) and 10 (b), respectively. The line spacing during scanning is 5 nm; and their corresponding cross-sectional plots (c) and (d).

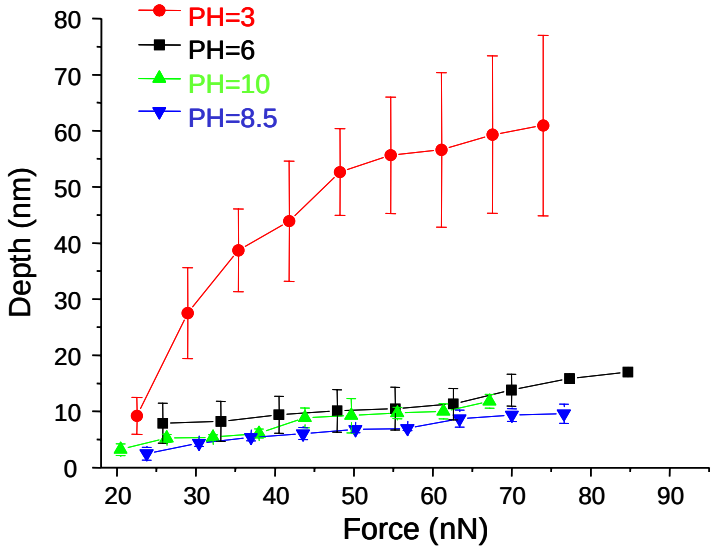

Figure 4.3. The averaged depth of nanopatterns created on GaAs surface by SPL in different solutions as a function of applied loads, at a line spacing of 10 nm.

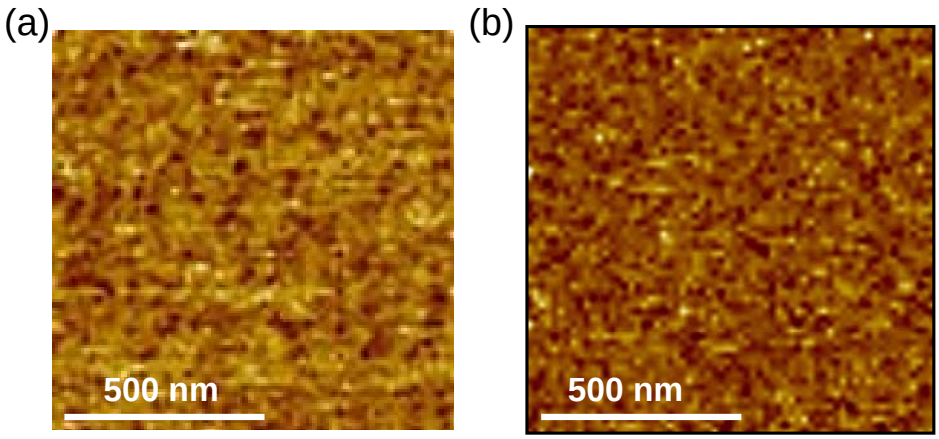

Figure 4.4. The AFM images of an etched GaAs surface (a) and SAMs on GaAs (b) with rms surface roughness of 1.09 nm and 1.05 nm respectively.

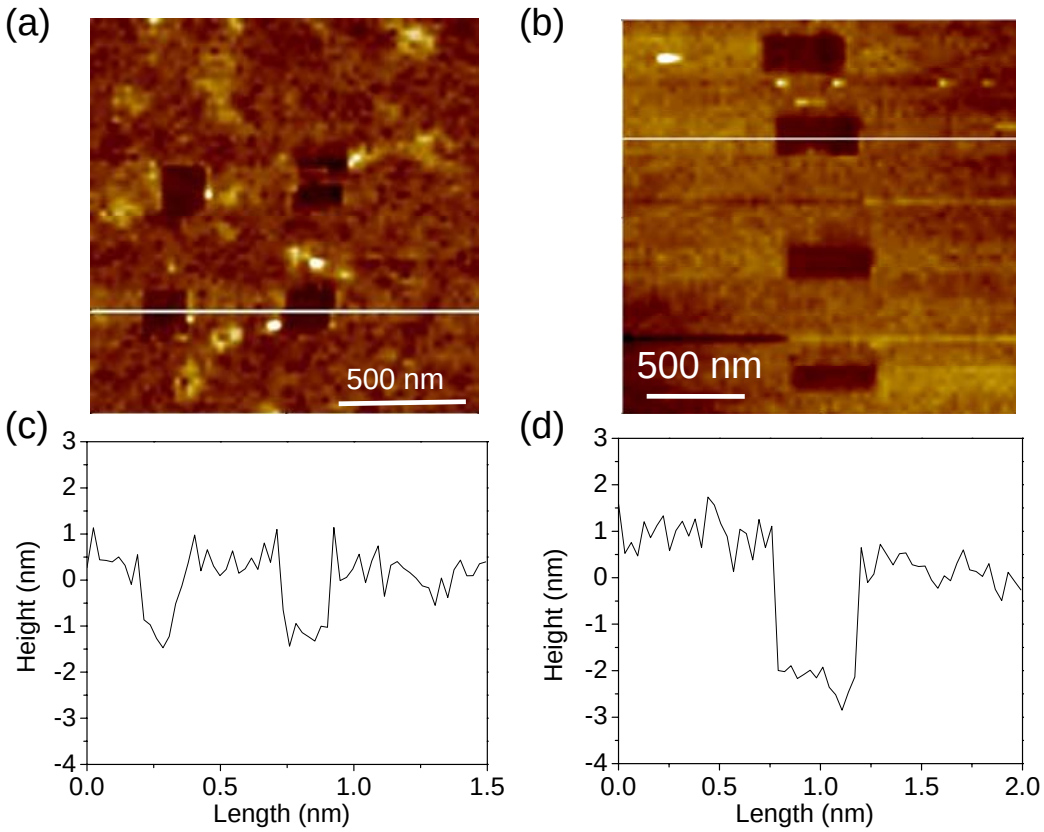

Figure 4.5. Nanopatterns created on SAMs/GaAS (a) in ethanol at an applied load of 37.8 nN, and (b) in ethanol with 5 mM NH_4OH at an applied load of 12.6 nN; and their corresponding cross-sectional plots (c) and (d) demonstrate that adding 5 mM NH_4OH produced much deeper nanowells on thiol modified surface even at low loads.

4.4. Summary

In summary, directly patterning of GaAs by SPL in aqueous solution was introduced, and the depth of the nanowells depends strongly on the applied load, the ph of the aqueous solution, and the line spacing during the scanning. This dependence is attributed to the tribochemical process, i.e. local oxidation, occurred between the scanned tip and GaAs surface. Nanopatterns with depth ranging from several nm to submicron have been successfully patterned on GaAs surface.

CHAPTER V

USING PATTERNED ARRAYS OF METAL NANOPARTICLES TO PROBE PLASMON ENHANCED LUMINESCENCE OF CDSE QUANTUM DOTS

5.1. Synopsis

Here we present a simple platform for probing plasmon enhanced photoluminescence (PL) of quantum dots by confocal microscopy. In this study, self-assembled monolayers of silane-derivative molecules were patterned onto the oxidized GaAs surfaces to direct the attachment of Au or Ag nanoparticles onto the surface. Following the directed binding of metal nanoparticles (MNPs), a layer-by-layer deposition of oppositely charged polymers was used to create films with varying thickness by controlling the numbers of deposited layers. CdSe quantum dots (QDs) of ~ 4 nm and 6.5 nm in diameter with 16-mercaptohexadecanoic acid as a surfactant were then adsorbed onto the outermost polymer layer via electrostatic interactions. Using confocal fluorescence microscopy, the enhanced PL from the CdSe over the Au or Ag nanoparticle patterns could be imaged directly and scaled against the regions with no Au or Ag nanoparticles, and the luminescence of the GaAs (as an internal standard) for different CdSe-metal separations. By using a pattern, PL enhancement as a function of particle-CdSe spacing can be readily probed all on a single platform, where the QDs over MNPs and not over MNPs can be directly compared in the same dielectric environment. The observed luminescence as a function of metal-QD separation can be

readily fit to a combined model of metal-fluorophore fluorescence quenching and local electric field enhancement.

5.2. Introduction

It is well known that the local surface plasmon resonance (LSRP) of MNPs can be excited when the particles are optically irradiated. The energy of the surface plasmon resonance is found to be dependent on the size, shape, composition, and organization of the metal nanostructure. As the LSPR of MNPs is found to change in response to the dielectric environment surrounding the particles, shifts in the peak position of the LSPR can be followed as a means of detection of analytes.[157,158] Enhancement in the Raman scattering of molecules in the proximity of MNPs have also been reported, which gives rise to surface enhanced Raman spectra (SERS) for which detection of signals down to the single molecule level have been reported.[159,160] Related to this, it has been observed that the photoluminescence intensity of quantum dots (QDs) and quantum wells (QWs) can also be enhanced by the electromagnetic coupling with metal surface plasmons.[161-167] Time-resolved spectroscopic studies of QD and QW structures coupled to MNPs have shown that the radiative decay rate, absorption cross section, and quantum efficiencies of luminescence generally increase in the presence of metal nanostructures due to the increased local electric field surrounding the irradiated metal structures. For example, Atwater and co-workers have shown that for Si nanocrystals coupled with a rough Au film, that the quantum efficiency for luminescence could be increased by ca. 60%.[165] The extent of the enhancement that can be achieved by coupling of QDs to

metal nanostructures or rough films, strongly depends on the proximity of the QDs to the metal structure, and has been shown to decay exponentially with increasing distance between the two. By bringing QDs closer to the metal, their photoluminescence can be enhanced by the locally increased electric field. However, if the QDs are too close to the MNP, quenching of the photoluminescence is observed. As such, a maximum in photoluminescence enhancement is found to occur at an optimal separation depending on the competitive effects of the distance dependence of the electric field and the quenching efficiency. In addition to QD-particle separation, the structure and type of metal particles used (*e.g.* Ag, Au), polarization of the incident light and the laser power have all been found to influence the extent of plasmon enhanced photoluminescence. The ability to quantitatively determine the extent of photoluminescence enhancement as a function of QD-metal separation however can be challenging as artifacts such as scattering differences between samples, variations in laser intensity and differences in dielectric medium, can make scaling the luminescence intensities of coupled and non-coupled quantum dots difficult to evaluate.

In this chapter we present a simple platform in which the coupling of CdSe quantum dots with Au or Ag nanoparticles has been quantitatively measured. To address some of the above mentioned challenges, we have positioned single layers of quantum dots on top of arrays of the desired metal nanostructure positioned in a grid pattern, in which the separation between the two was controlled with a polymer spacer formed using layer-by-layer assembly. This simple approach yields a patterned structure in which the photoluminescence of the QDs above the metal patterns may be directly

scaled against those not above the metal pattern by imaging the structure with confocal fluorescence microscopy. Additionally as this structure is built on a GaAs(100) single crystal, the inherent luminescence of the GaAs offers the means of scaling each measurement from sample to sample, aiding in eliminating effects of scattering or variations in laser intensity. From these studies we have shown that this simple platform can be readily made using chemical self-assembly approaches and adapted to various materials. Here we report two initial studies of the coupling of CdSe quantum dots of *ca.* 4 nm and 6.5 nm in diameter, with Au nanoparticles and Ag nanoprisms respectively, as a function of metal-QD separation.

5.3. Experimental Details

Preparation of Silane Monolayers. Single side polished GaAs(100) substrates (AXT, 400 μm, Si-doped, University Wafer, Inc., Boston, MA) were etched and cleaned following the procedures described previously by Jun *et al.* to remove the native oxide using dilute acid and base solutions.[168] Briefly, the GaAs samples were immersed into 1:20 NH_4OH/H_2O solution for 1 min and then rinsed liberally with high purity (18.2 MΩ•cm) water (NANOpure Diamond, Barnstead), followed by ethanol. The GaAs substrates were immediately immersed into a 1:10 HCl/ethanol solution for 1 min. The substrates were subsequently rinsed with copious ethanol, blown dry with streaming nitrogen, and treated with UV/ozone for 20 min to make a fresh oxide layer on the GaAs surfaces. Self-assembled monolayers (SAMs) of 3-aminopropyltriethoxylsilane (APTES, purchased from Gelest, Inc.) were formed by immersion of the freshly oxidized GaAs

substrates in 5 mM APTES in ethanol for 12 h. After being taken out from the solution of APTES, the SAM-modified substrates were rinsed with ethanol and blown dry under a nitrogen stream in preparation for patterning.

X-ray Photoelectron Spectroscopy. To evaluate the surface chemistry XPS data were acquired with a Kratos Axis ULTRA X-ray photoelectron spectrometer equipped with a 165 mm hemispherical electron energy analyzer. The incident radiation was the MgKα X-ray line (1253.6 eV) with a source power of 180 W (15 kV, 12 mA). The analysis chamber was maintained at a steady base pressure of $< 6 \times 10^{-9}$ Torr during sample analysis. Survey scans of up to 1100 eV were carried out at an analyzer pass energy of 160 eV with 1.0 eV steps and a dwell time of 300 ms. Multiplexed high resolution scans of the Ga(3d), C(1s), As(3d), and N(1s) regions were taken at a pass energy of 40 eV with 0.1 eV steps and a dwell time of 60 ms. The survey and high resolution spectra were obtained with averages of 5 and 50 scans, respectively. The C(1s) peak at 284.8 eV was set as a reference for all XPS peak positions to compensate for energy shifts due to the spectrometer work function.

Synthesis of CdSe QDs. Trioctylphosphine oxide (TOPO)-passivated CdSe spherical nanocrystals were synthesized from well-established solvothermal methods.[169,170] 250 mg of CdO with 2.85 g hexadecylamine, 1.15 g TOPO and 1.09 g tetradecylphosphic acid were degassed under reduced pressure at 110 ºC for one hour. Then, under nitrogen, the solution was heated to 300 ºC until it became optically clear.

0.5 g tri-n-butylphosphine (TBP) was injected and the temperature was reduced to 260 ºC. 0.8 g of a 10% by weight Se powder in TBP solution was then quickly injected. When the desired size was reached, the flask was cooled down to 60 ºC and 10 g of nonanoic acid was added. Methanol was used to clean the solution and the nanocrystals were subsequently resuspended in toluene. Cleaning with methanol was repeated three times. Exchange of surfactant group from TOPO to water- soluble group was performed as follows.[171] First, 20 mg of 16-mercaptohexadecanoic acid (16-MHA) was dissolved in 15mL of methanol. The pH of the solution was adjusted to 10-11 using tetramethylammonium hydroxide and 20 mg of CdSe nanocrystals were added to this solution. The mixture was refluxed under nitrogen atmosphere for 6 hours. To clean the nanocrystals, a mixture of ethyl acetate and ether was used to precipitate the particles which could then be resuspended in methanol. Subsequent cleanings used only ethyl acetate to precipitate the particles. After the final cleaning, the 16-MHA-passivated CdSe were resuspended in water. The particle size was determined by TEM (Figure 5.1)

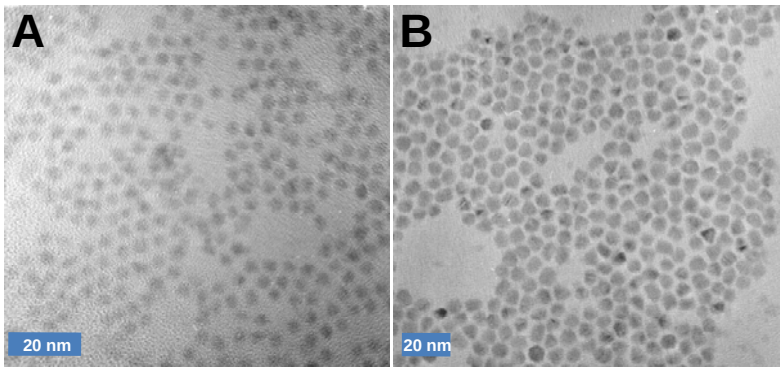

Figure 5.1. TEM images of (A) 4 nm and (B) 6.5 nm CdSe QDs.

Synthesis of Gold and Silver Nanoparticles. Two types of particles were investigated in this study, Au nanoparticles and Ag nanoprisms. Au nanoparticles were prepared by reducing $HAuCl_4$ (Alfa Aesar, 99.99% purity) with sodium citrate.[172] The size of the citrate-stabilized gold NPs was determined to be ~18 nm in diameter based on by the maximum surface plasmon absorbance in the UV-visible spectra (USB-ISS-UV/Vis, Ocean Optics Inc.) at 523 nm. AFM images of isolated Au particles also confirmed the size to be 18 ± 2 nm. The Ag nanoprisms, were synthesized by first creating spherical silver NPs by the reduction of $AgNO_3$ (Sigma, 99+% purity) with $NaBH_4$ in an ice bath.[173] Here, 1 mL of 10 mM $AgNO_3$ in water was injected into 99 mL of 1 mM $NaBH_4$ and 0.3 mM sodium citrate aqueous solution. The color of this mixed solution turned to yellow immediately (Figure 5.2A) and was kept stirring in an ice bath for 30 min. The photochemical shape conversion of spherical Ag NPs into flat nanoprisms was carried out by exposure to a white fluorescent lamp (15 W) for ~72 h with a sample-source distance of ~ 5 cm. The color of the Ag NPs solution changed from yellow to green (Figure 5.2A) gradually during the period of illumination. The average edge length and thickness of triangular Ag nanoprisms measured by TEM (*vide infra*) were 100 ± 20 nm and 12 ± 3 nm, respectively (Figure 5.2C). Approximately 50% of the Ag nanoparticles were found to be completely converted to nanoprisms.

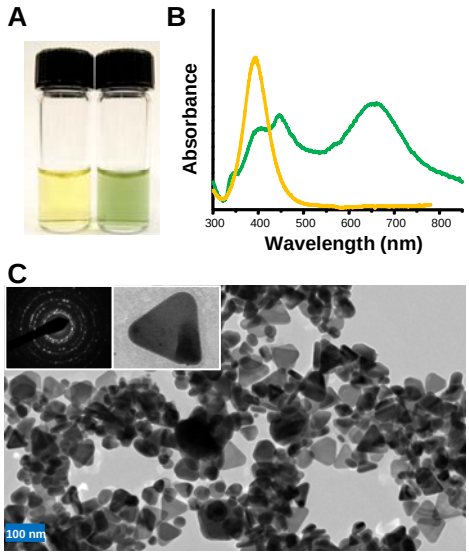

Figure 5.2. (A) Photographs of Ag nanosphere (left) and nanoprism (right) solutions and (B) their corresponding absorption spectra displayed in yellow and green line, respectively. (C) TEM image of photoinduced Ag nanoprisms. The inserts show the electron diffraction analysis and enlarged view of single Ag nanoprism.

Patterning of Metal Nanoparticles. There are very few methods available to pattern MNPs on GaAs surfaces, despite that on other metal or semiconductor surfaces, many approaches for the micro- and nano-fabrication techniques of spatially organized patterns including metal nanostructures,[174-178] proteins/DNA,[21-25] organic molecules,[26-28] and organic semiconductor[179,180] have been developed such as photolithography,[33,34] microcontact printing,[35,36] direct evaporation,[37] scanning probe lithography,[38,39,181] electron-beam lithography,[41,42] paylene-based lift-off method,[43] focused ion beam lithography,[44] and nanoimprinting[45]. The reason comes from the strong propensity towards oxidization[10,182] of bare GaAs surfaces after a few days in ambient atmosphere makes this topic difficult to deal with.

For patterning linker molecules on GaAs surface, oganosulfur and oganosilane molecules were considered in our system. Recently, there have been a number of reports of successfully growing oganosulfur molecules on GaAs surface by removing the native oxide layer using base and/or acid prior to modification.[12-14] However, this strategy has some drawbacks. Firstly, the fabrication of thiol SAMs on GaAs needs the preparation procedures in anaerobic environment such as anhydrous/degassed solvents and a nitrogen or argon purged glovebox in order to generate high quality and good reproducibility of SAMs with maximum degree of arrangement. Secondly, it has also been reported that alkanethiols self-assembled rate on GaAs is nearly 2 orders of magnitude slower than on Au, for example, only ~80% coverage was reached after 12 h for the octadecanethiol/GaAs SAMs.[183] Thirdly, the patterning of thiol self-assembled monolayers (SAMs) suffers from challenges owing to their susceptibility to exchange with solute thiols, easy oxidation, and slow adsorption rate. The significant instability of these protective molecules resulted from the gradually oxidative degradation by the penetration of water molecules or oxygen adsorption to the etched GaAs surfaces was observed after couple weeks of air exposure[13] These disadvantages make thiol SAMs undesirable for GaAs electronic passivation.

The alternative method is to introduce a fresh thin oxide layer as a binding layer onto GaAs surfaces by exposing the substrate to UV-ozone or oxygen plasma after base and acid treatment. There have been only a few reports focusing on using this oxide layer on GaAs substrates.[18-20] Here, instead of using thiol molecules, we have demonstrated that the patterning of silane monolayers on oxidized GaAs substrate can be

easily achieved through UV photolithography by taking the advantage of strong Si-O-Ga/As and Si-O-Si bonds. By using this protocol, we are able to position and attach Au or Ag nanoparticles (NPs) onto GaAs surfaces with predetermined patterns using organosilane molecules as the linkers. First, the pristine GaAs wafers were cleaned with dilute NH_4OH and HCl to remove the native oxidation layer and surface contamination. Then the GaAs substrates were exposed to UV/ozone for 20 min to produce a fresh oxide layer. Formation of OTMS and APTES SAMs were carried out by simply immersing the pretreated GaAs substrates into APTES or OTMS solutions for couple hours. In addition to OTMS and APTES, we found that other precursor molecules with (m)ethoxysilane terminal group, including octadecyltrimethoxysilane, (3-mercaptopropyl)trimethoxysilane, 2-(4-pyridylethyl)triethoxysilane and (3-triethoxylsilylpropyl)4,5-dihydroimidazole, can also be modified onto oxidized GaAs surfaces using the same method. Interestingly, for precursor molecules with chlorosilane terminal group such as octadecyltricholrosilane, which is a good SAM precursor for Si surfaces, very poor quality of SAMs were formed on oxidized GaAs surface. A possible explanation for this is that the HCl generated during chrolosilane based SAMs formation[184] will etch the GaAs surfaces and thus prevent forming high quality monolayers.

Briefly, the synthesized MNPs were bound to an oxidized GaAs surface by attachment to a patterned layer of APTES on the surface (*vide supra*). Patterned arrays of the APTES SAMs were created on the oxidized GaAs surface by photolithography. Here, a grid pattern was generated on the GaAs surface using a TEM grid (T2000-Cu,

Electron Microscopy Inc.) as a shadow mask. The TEM grid was placed on top of the APTES-modified GaAs and the mask/substrate framework was exposed to UV/ozone (λ_{em} = 185 nm and 254 nm) at a distance of ~ 1 cm away from the sample for 15 min. After selective photo-oxidation of the APTES SAM, the TEM grid was removed from the surface and the substrate was rinsed with ethanol and then immersed into a 5 mM solution of *n*-octadecyltrimethoxysilane (OTMS) in toluene for 4 h, allowing the OTMS SAM to grow and fill in the exposed GaAs regions. This resulted in a patterned array of hydrophobic and hydrophilic regions on the surface. After patterning, the surfaces were rinsed in sequence with toluene, ethanol, and water, followed by soaked in one of the citrate-stabilized Au or Ag nanoparticle solutions for 12 h to allow for attachment of the MNPs onto APTES SAMs by electrostatic attraction. Following nanoparticle attachment, the samples were rinsed copiously with water to remove any Au or Ag NPs non-specifically bound to the hydrophobic regions of the surface.

Layer-by-layer Deposition of Polymers. To control separation distance between the patterned MNPs and the CdSe, a polymer spacer formed by layer-by-layer assembly was used. Here, a positively charged polymer solution was prepared by adding 0.5 M NaCl to an aqueous 5 μL/mL poly(diallyldimethylammonium chloride) (PDADMAC) (Aldrich, 20 wt. % in water, M_w 100,000-200,000) solution. For the negatively charged polymer solution, an aqueous solution of 1mg/mL poly(sodium 4-styrenesulfonate) (PSS) (Aldrich, M_w 70,000) containing 0.5 M NaCl was prepared. To create different thicknesses of polymer layers, the patterned metal arrays on GaAs (carrying net negative

charge) were immersed into the PDADMAC solution for 30 min to allow for full adsorption of a single layer. The substrate was then rinsed liberally with water and followed by dipping into the PSS solution for the second layer polymer adsorption. For multilayer deposition, this cycle was repeated, with the outermost layer always terminating in a positive layer of PDADMAC to allow for the further attachment of negatively charged 16-mercaptohexadecanoic acid terminated CdSe QDs.

Sample Imaging. AFM images were acquired with a combined confocal fluorescence/atomic force microscope (WITec Alpha300 R, Germany) under ambient conditions (24 ± 2 ^{o}C). All AFM images were acquired in tapping mode using commercially available aluminum-coated silicon AFM tips from Nanoscience Instrument (Phoenix, AZ) with nominal tip radii of less than 10 nm and nominal spring constants of 48 N/m. Images were acquired at a resolution of 512 x 512 lines at a scan rate of ~1 Hz. The photoluminescence spectra were collected using an Ar ion laser at 488 nm (~70 $\mu W/\mu m^2$) as the excitation source with a typical integration time of 36 ms/pixel. A Nikon 100x (0.9 NA) objective was utilized for imaging and spectral data acquisition and the laser was focused to a spot size of ~1 μm^2. The spectral data were acquired with an Acton triple grating spectrometer with an Andor Peltier cooled (-66 ^{o}C) CCD detector. High resolution images are obtained by integrating the complete photoluminescence spectra for the given region of interest (500-650 nm for the 4 nm CdSe QDs, 550-700 nm for the 6.5 nm CdSe QDs and 750 – 900 nm for the GaAs) at each image pixel (typically 200 x 200 pixels per image). Scanning Electron Microscopy

(SEM) images were obtained with a Joel 6400 SEM under vacuum. All samples for SEM imaging were modified by Au sputtering to increase the conductivity and decrease the effects of charging. Transmission electron micrographs (TEM) of the synthesized CdSe nanoparticles were acquired using a JEOL 2010 transmission electron microscope at an acceleration voltage of 200 kV. Samples were prepared using copper grids from Ted Pella. A drop of CdSe solution, in toluene, was dropped onto the grid and allowed to evaporate at room temperature.

5.4. Results and Discussion

Formation of Au or Ag Arrays on GaAs. In order to directly compare the effects of metal nanoparticles on the photoluminescence of QDs, we created a patterned array of metal nanoparticles on a GaAs substrate by directing attachment of the metal particles to the surface with an amine terminated self-assembled monolayer. This patterned layer could then be covered by a polymer spacer layer of varying thickness through layer-by-layer assembly and then coated with a single layer of quantum dots. Using this approach the ratio of the photoluminescence intensities from the QDs over the metal particles could be directly scaled against the regions without metal particles in a single photoluminescence image. Figure 5.3 illustrates our method of selectively patterning Au or Ag nanoparticles (NPs) on the GaAs surface. While several approaches were tried (*vide supra*), ultimately the attachment of alkoxysilane SAMs on the oxidized GaAs surface yielded the best results in terms of film stability and metal particle attachment density.

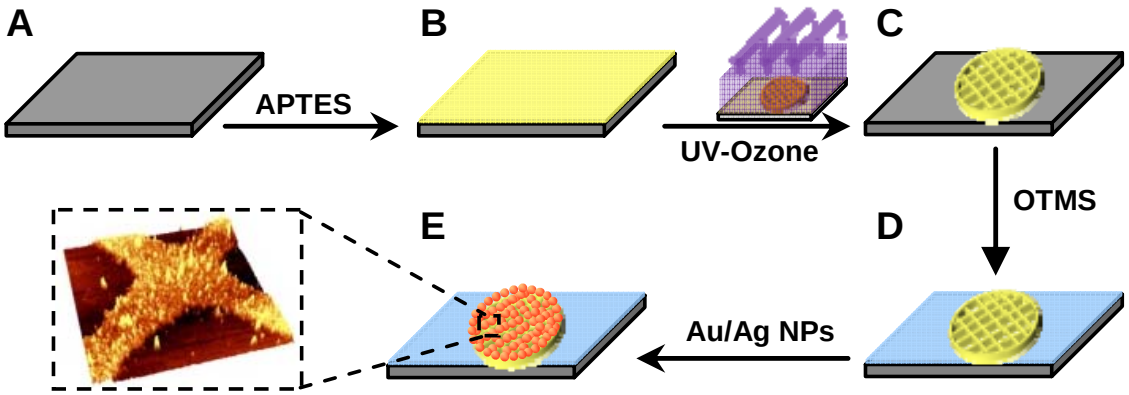

Figure 5.3. Schematic diagram of patterning metal NPs on GaAs. GaAs substrates are first cleaned and oxidized (A), and then modified with an APTES SAM (B). A Cu TEM grid is placed on top of SAM-functionalized GaAs surface and exposed to the UV-Ozone for 20 min, leaving an APTES SAM in the unexposed regions (C). After removing the grid, the GaAs surfaces are immersed in OTMS solutions for 4 h to backfill the excavated area (D). The substrates are next soaked in the desired citrate stabilized Au or Ag NPs aqueous solution where they attach to the amine terminated regions of the surface (E).

To form the patterned metal grid structure, the cleaned and oxidized GaAs surface was first coated with a uniform SAM of the aminopropyltriethoxysilane (APTES) (Figure 5.3B). Following APTES assembly, a Cu TEM grid was placed in conformal contact with the GaAs substrate to function as shadow mask, and then the sample was then exposed to UV/ozone to photo-oxidize the uncovered portions of the SAM layer (Figure 5.3C). Following rinsing, the oxidized SAM was removed and now the uncovered GaAs regions were then backfilled with an octadecyltrimethoxysilane (OTMS) SAM resulting in a patterned array of hydrophilic and hydrophobic regions on the surface (Figure 5.3D). Finally, the sample was immersed in the desired solution of Au or Ag NPs (*ca*. pH 7) to allow for the citrate stabilized NPs to attach onto the amine rich regions by electrostatic interaction (Figure 5.3E). A few nanoparticles were found to

attach to the OTMS regions, but those that did were weakly bound and could be readily rinsed away.

As the assembly process was carried out in water, the stability of the SAM is of the utmost importance. To confirm the high quality and stability of the silane SAMs formed using this method, Fourier transform infrared reflection absorption spectroscopy (FT-IRAS) measurements were obtained for OTMS SAMs and XPS experiments were performed for the APTES SAMs on the oxidized GaAs surface. The FTIR spectra of OTMS sample showed that the $\nu_{as}(CH_2)$ asymmetric stretch was centered around 2917 cm^{-1} (data not shown), which is characteristic of well ordered crystalline-like silane SAM.[185,186] After 8 months of air exposure, the OTMS SAMs were observed to exhibit no observable signal decrease for both $\nu(CH_2)$ and $\nu(CH_3)$ stretch modes and the $\nu_{as}(CH_2)$ asymmetric stretch was maintained at *ca.* 2917 cm^{-1}. As compared to SAMs of octadecanethiol on GaAs, which we also explored for this patterning purpose (*vide supra*), these films demonstrated much greater stability, as the octadecanethiol/GaAs SAMs were found to degrade within a couple of weeks under ambient conditions. For the APTES SAMs, a representative survey spectrum of XPS is shown in Figure 5.4, confirms the presence of the APTES SAM on the oxidized GaAs surface. High-resolution spectra of the C(1s), N(1s), and Ga(3d) regions show peak binding energies of 284.8 ± 0.1 eV, 399.0 ± 0.1 eV and 20.5 ± 0.1 eV, respectively, while the high-resolution As(3d) signal can be separated into two peaks at 44.8 ± 0.1 eV for As oxides and 42.2 ± 0.1 eV corresponding to GaAs bulk. The XPS data also indicates that a fresh

oxidation layer was readily introduced by UV/ozone and the APTES monolayers were successfully grown on these surfaces.

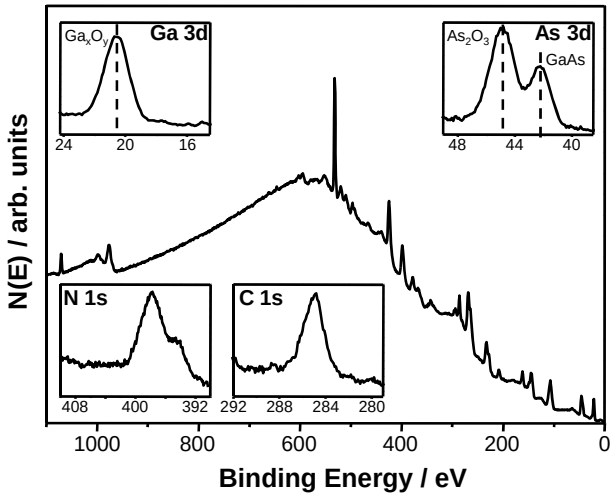

Figure 5.4. X-ray photoelectron survey and high-resolution spectra for APTES monolayers on GaAs (100). The high-resolution spectra show the Ga(3d), As(3d), N(1s), and C(1s) spectral regions which show that the surface is first oxidized and then covered by the APTES SAM.

Following particle attachment, the resulting grid structures were examined by AFM. Topographic AFM images of the patterned Au arrays on GaAs are shown in Figure 5.5A-D. The cross-sectional profile (Figure 5.5B) reveals that the average height of the Au array is 18 ± 2 nm which is consistent with the size of a single-layer Au NPs, suggesting that the interparticle repulsive force due to the citrate stabilizer was sufficient to prevent the physical adsorption of a second layer of Au NPs. Similar results were also observed for Ag-nanoprism patterns as presented in Figure 5.5E-H, in which the cross-sectional analysis shows the average height of ~ 120 nm in accordance with the edge-length of a silver nanoprism, suggesting the Ag nanoprisms stand up face by face rather than lie down flat and stack on the surface. As mentioned above, the gold nanoparticles

were found to exhibit an absorption maximum at ~ 523 nm, which suggests that the average size is ~18 nm in diameter.[187] The silver nanoprisms of 100 ± 20 nm in edge-length which were synthesized from small Ag nanospheres following the reported photoinduced transformation method[188] have two broad absorption peaks around 450 nm and 670 nm. The extinction spectra of each however were found to be modified after deposition onto the substrate (determined from deposition on APTES modified glass coverslips) showing the emergence of an extinction peak at 660 nm for gold NPs and the broadening of silver-NP plasmon peak at higher wavelength. These effects can be ascribed to interparticle coupling and/or disorder of the NP films (Figure 5.6).[189,190] These interparticle coupling effects will impact the PL enhancement of QDs based on the degree of spectral overlap as has been reported previously.[164,191,192]

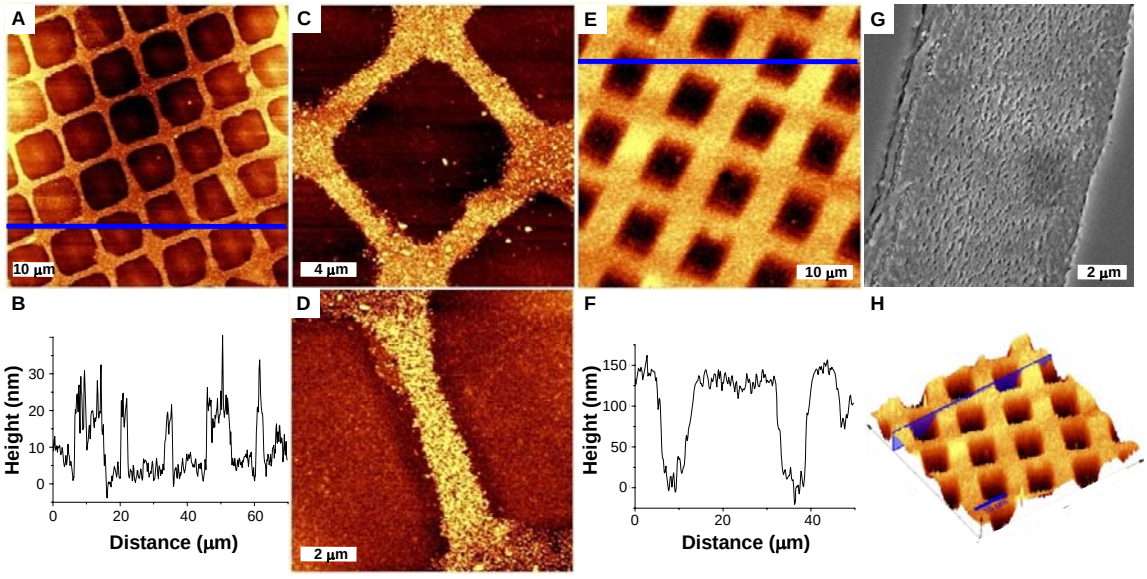

Figure 5.5. Topographic AFM images of the Au and Ag patterned metal nanoparticle arrays on GaAs(100). Au-NP patterns: (A) 70 x 70 µm and (B) its corresponding cross-sectional plot (blue line) showing that a single layer of particles is bound to the surface, (C) 20 x 20 µm, and (D) 10 x 10 µm. Ag-NP patterns: (E) 50 x 50 µm and (F) its

corresponding cross-sectional plot (blue line). (G) SEM image (10 x 10 μm) of the Ag film, and a (H) 3-D topographical plot showing the waffle like structure of the thick Ag film which corresponds in thickness to the long axis of the Ag nanotriangles used.

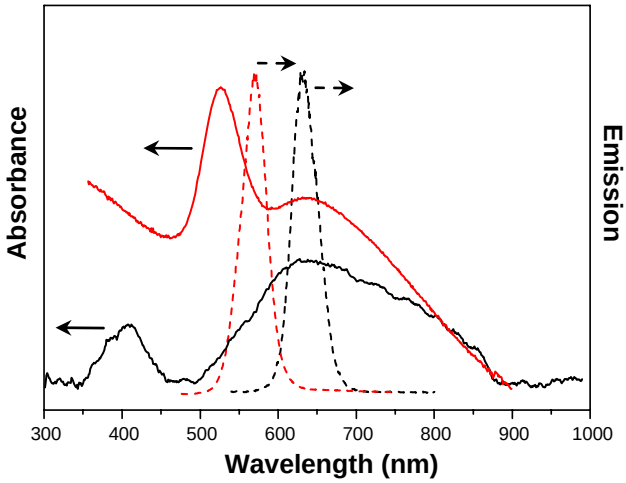

Figure 5.6. UV-visible spectra of Ag NPs (solid black line) and Au NPs (solid red line) on APTES-modified glass with 5 layers of PSS:PDADMAC; and photoluminescence of 6.5 nm CdSe (dash black line) and 4 nm CdSe (dash red line) nanocrystals on top of 5 layers of PSS:PDADMAC.

Controlling CdSe-Metal Distance. Previous work by Kulakovich *et al.* has shown that layer-by-layer polymer assembly can be used to provide a controllable spacing layer for QD-metal films. Here we have adapted this approach to our patterned array to also control separation and test our platform against a known system (CdSe-Au).[163] Following creation of the metal grid structure, the CdSe quantum dots of the desired size were then attached at controlled distances from the metal pattern using layer-by-layer polymer assembly. Here, alternating layers of poly(diallyldimethylammonium chloride) (PDADMAC) and poly(sodium 4-styrenesulfonate) (PSS) were put on the surface in order to build up films of controlled thickness. This began with a positively charged layer of PDADMAC, followed by the negatively charged PSS layer. Terminating with

an additional PDADMAC layer yields a surface with a net positive charge, onto which our 16-MHA terminated CdSe particles (which carry a net negative charge at the assembly pH) could then be bound electrostatically (Figure 5.7A). Importantly, these polymer layers have no optical absorption in the visible region of the spectrum and have not been observed to quench QD emission.[163] Although the thickness dependence of these different polyelectrolyte layers has been well determined previously[193] for deposition on surfaces such as polystyrene particles, it is likely that this will dramatically vary from surface to surface. As such, to accurately determine the polymer film thickness, in our patterned arrays, a background thickness (D_1) was determined by tapping-mode AFM after slightly scratching through assembled polymer films with varying numbers of layers on the oxidized GaAs surface (Figure 5.7). Extending this to the patterned grid such as for the Au-NP system, illustrated in Figure 5.7A, once the value of D_1 is determined, the thickness of polymer thin films above Au NPs, D, can be simply derived from the following relationship:

$$H + 4 + D_1 = 4 + D + 18 \text{ (nm)} \quad (1)$$

where 4 nm is the average diameter of the CdSe QDs, 18 nm is the average diameter of the Au nanoparticles, and H is the height difference between the regions with and without Au NPs after coating of the polyelectrolyte spacers and CdSe QDs, as determined from the topographic AFM images (*e.g.* Figure 5.8A). Plotting the value, D_1, against different numbers of polymer layers (Figure 5.7C) shows a nonlinear increase in film thickness with the number of layers.

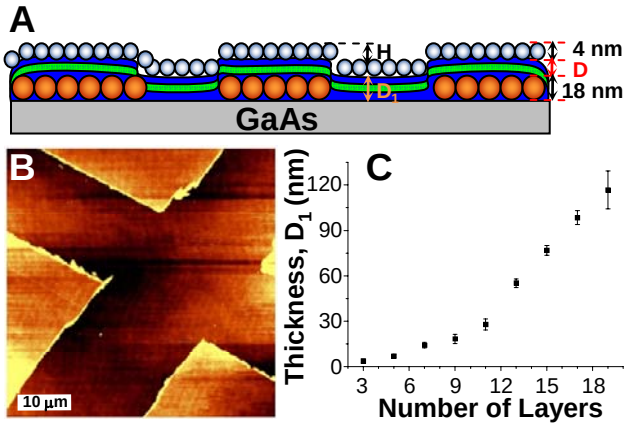

Figure 5.7. (A) Schematic cross-sectional view of the sample showing that polymers and 4 nm QDs were deposited onto Au-NP arrays on GaAs in sequence. (B) AFM topographic image of different layers of polymers deposited on pure GaAs substrates without metal patterns which were removed by scratching. (C) The polymer thickness on bare GaAs (D_1) measured from AFM versus the number of polyelectrolyte layers.

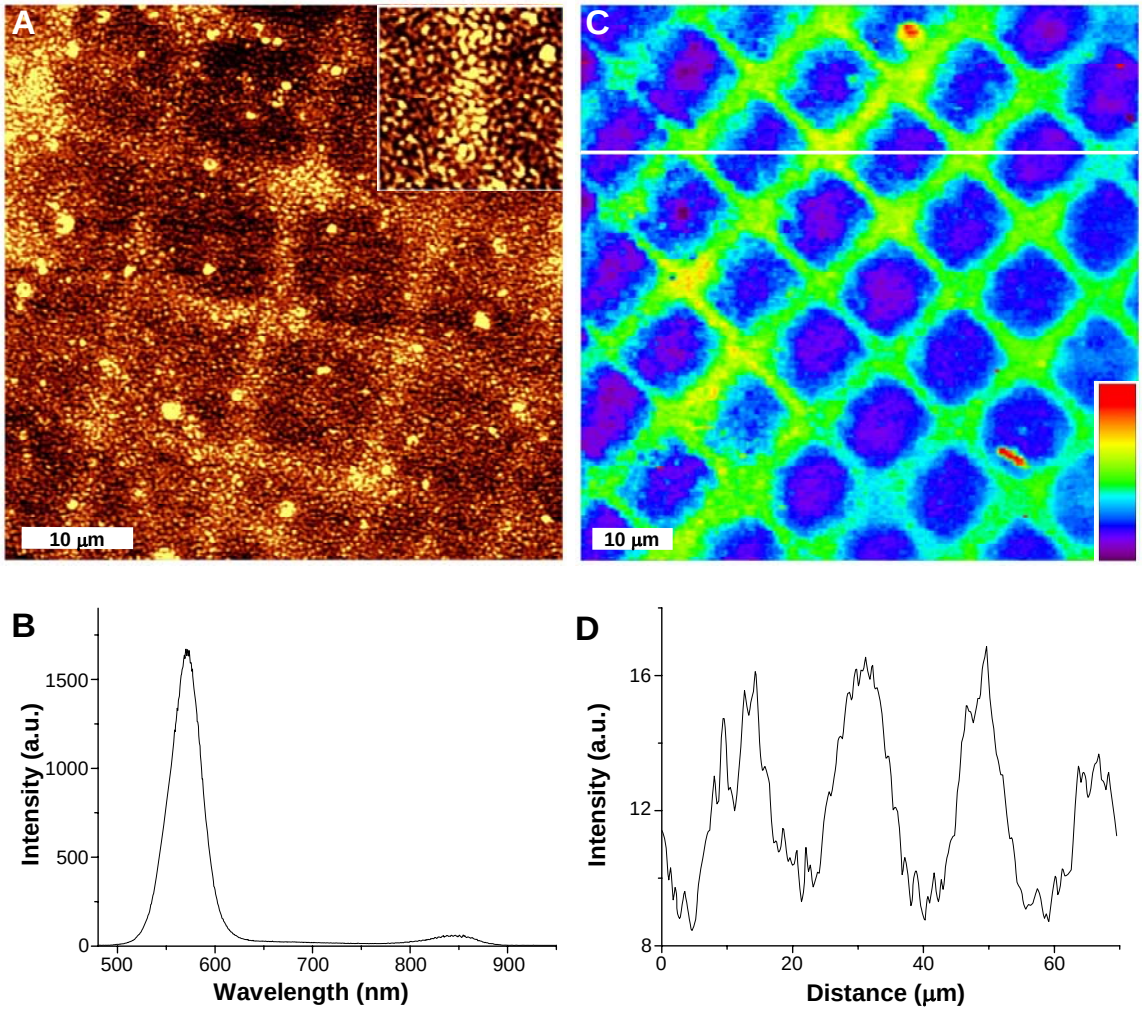

Figure 5.8. (A) Topographic AFM image of CdSe QDs deposited on 19 layers of polymer over a Au-NP patterned GaAs surface. The top-right inset magnifies a 10 x 10 µm area. (B) A representative emission spectrum from the film in panel A shows both the CdSe and GaAs emission at ca. 585 nm and 845 nm respectively. (C) A false color photoluminescence image of 4 nm CdSe QDs above 9 layers of polymers on Au-NP patterned GaAs surfaces (the z-scale bar is from 7-23 a.u.). The image is produced by integrating the spectral region for the CdSe from 500-650 nm. (D) The cross-sectional plot corresponds to the white line in panel C, illustrating the relative photoluminescence enhancement.

Photoluminescence Measurements. By using patterns of Au or Ag NPs on the GaAs surface, the environment of the CdSe QDs could be separated into two parts:

regions with and without NPs under the polymer spacer layer. To measure the relative photoluminescence of the two regions, the sample was imaged using a confocal fluorescence microscope with an Ar ion laser at 488 nm as the excitation light. The PL intensity of CdSe over the NPs could then be directly normalized to those of the adjacent CdSe without NPs. Figure 5.8B shows a typical luminescence spectrum within this ensemble. The peak around 585 nm originates from CdSe QDs and the peak around 845 nm is from the GaAs background. Although the PL intensity from the GaAs background should remain constant during each experiment, undesired fluctuations of laser power can occur from sample to sample. Thus, by using GaAs as the support background, we could use the PL intensity from GaAs as a built-in reference to normalize the PL intensity of the QDs for each individual measurement. A representative PL image plotted using the CdSe emission spectrum, integrated from 500-650 nm clearly shows that the luminescence of the QDs over the Au pattern is enhanced relative to the non-metal containing regions (Figure 5.8C). From the cursor profile (Figure 5.8D) it can be seen that in this case the QDs over the metal particles show nearly twice the intensity of those not over the metal.

One challenge in quantifying the extent of the photoluminescence enhancement is that reflection or scattering of the laser source by the MNPs might re-excite the CdSe QDs and thus results in an artificial increase in CdSe PL. To examine the possibility of this factor, the sample was scanned with a low laser power (70 $nW/\mu m^2$) and a confocal scanning image was generated by collecting the 488 nm laser spectrum itself (Figure 5.9A). The results indicate that the gold NPs strongly absorb the laser light owing to

their broad absorption around 523 nm rather than reflect/scatter the laser light. As shown in Figure 5.9B, the laser intensity above the regions of Au NPs (white spot) shows 48% lower intensity than that above the regions without Au NPs (red spot). Nevertheless, based on this, the relative absorption is insignificant and can be neglected when higher laser powers (*ca*. several tens of $\mu W/\mu m^2$) are used for the PL measurements. Similar results for PL enhancement of CdSe QDs of 6.5 nm in diameter were observed on Ag-NP arrays (Figure 5.10).

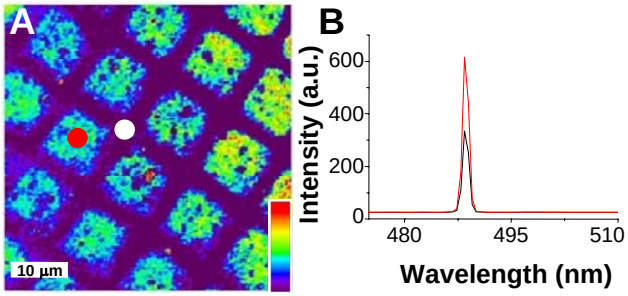

Figure 5.9. (A) A confocal scanning microscopy image generated by collecting the 488 nm laser line on 9 layers of polymers deposited upon Au-NP patterned GaAs surfaces (the z-scale bar is from 50-850 a.u.). (B) Spectra on the GaAs background (red circle) and Au-NP patterned (white circle) regions. The red line and the black line represent the averaged spectrum of the reflected laser light of red circle and white circle areas in panel A, respectively.

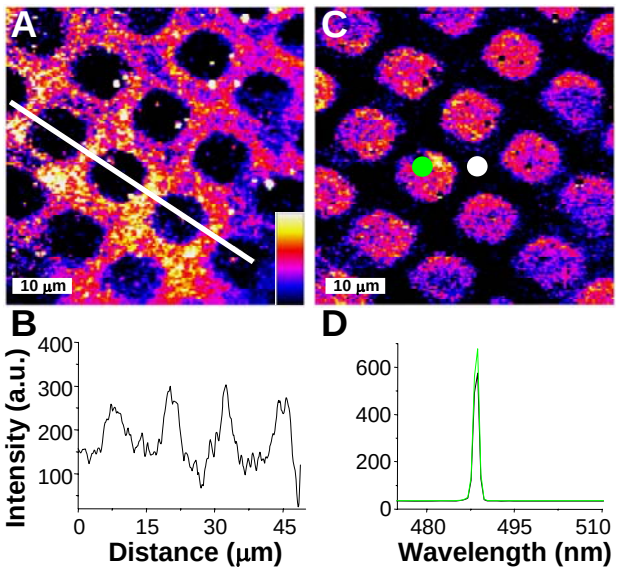

Figure 5.10. (A) False color photoluminescence image of 6.5 nm CdSe QDs above 5 layers of polymer on a Ag-NP patterned GaAs surface (the z-scale bar is from 165-300 a.u.) and (B) its cross-section analysis along the white line. (C) The corresponding confocal image at the same scanning region generated by collecting the 488 nm laser line on 5 layers of polymers deposited upon Ag-NP patterned GaAs surfaces. (D) Reflected laser light from the GaAs background (green circle) and the Ag-NP patterned (white circle) regions. The green line and the black line represent the averaged spectrum of green circle and white circle areas in panel C, respectively.

The plasmon enhancement of the QD photoluminescence was found to depend on the number of polymer layers which controls the QD-metal separation (Figure 5.11). For the Au-NP system, the enhancement was found to reach a maximum at 9 layers of polymer, corresponding to ~10.8 nm. For the Ag-NP system, the maximum peak was at 5 layers of polymer (~7.7 nm). An overall maximum enhancement by a factor of two was observed in both the CdSe-Au and CdSe-Ag systems, and is consistent with previous results for coupling between CdSe and Au nanoparticles.[163] These results can be partially attributed to the locally enhanced electric field surrounding the MNPs under illumination, where the maximum field enhancement should occur at the closest QD-

metal separation distance.[194] At such close QD-particle distances however, competitive mechanisms such as quenching, prevail due to electron transfer or non-radiative energy transfer from the QDs to the metal.[195-199] As such, these two mechanisms compete with each other and thus render a distribution of PL enhancement as a function of separation between the QDs and MNPs (Figure 5.11). When the QDs are more than 20 nm away from the MNPs, there is little to no coupling observed between the QDs and the MNPs. For the CdSe-Au system, the trend in photoluminescence enhancement as a function of distance was found to be highly reproducible. For the CdSe-Ag system, however a large standard deviation in the photoluminescence intensity was observed for small separations. We attribute this to the much larger surface corrugation of the Ag films, due to the much larger particles and degree of inhomogeneity in their size (~100 ± 20 nm).

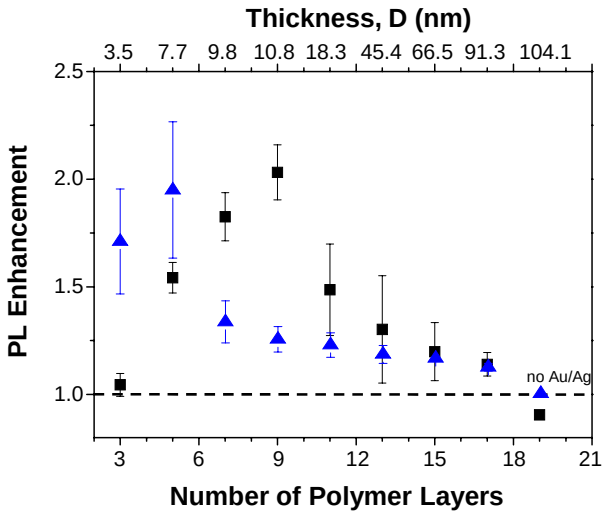

Figure 5.11. PL intensity enhancement of CdSe QDs versus number of polymer layers between QDs and Au (black squares)/Ag (blue triangles) NPs. The upper x-axis indicates the calibrated thickness of corresponding polymer spacer (D) above metal NPs as illustrated in Figure 5.7A.

While the measured enhancement for the CdSe-Au was consistent with previous reports, the observed enhancement for the Ag system was lower than we expected considering the typically large enhancements for other optical properties such as SERS signals for Ag as compared to Au materials. In one previous report, coupling between InGaN with rough Ag films was shown to yield enhancements by as much as 14-fold.[164] One might also expect that Ag nanoprisms should offer higher enhancement than the Au nanoparticles owing to the larger local electric field typically surround the sharp points of a Ag nanoprism. Several factors may contribute to the lower than expected enhancement. In particular, our yield of complete photoinduced conversion of Ag nanospheres to nanoprisms was found to be only ~50% on the basis of the UV-visible spectra and TEM images (Figure 5.2), such that *ca*. half of the Ag NPs in the films are non-resonant with both the CdSe QDs as well as the excitation laser. The intrinsic low-coverage citrate-coated Au or Ag NPs on surfaces may also partially explain the lower than expected enhancement.[200] Lastly, it has also been demonstrated that the angle of the incident light and polarization can greatly influence the local-field enhancement for materials with sharp geometries such as nanoprisms, which we did not vary in our measuremnts.[190,201] As such, each of these factors likely contribute to the reduced PL enhancement by the citrate-covered Ag nanoprisms.

Mechanism. In order to elaborate on the experimental results to determine if the distance dependence we observed is reasonable, we separated the interactions between QDs and MNPs into two factors: PL quenching due to energy transfer from the QDs to

the MNPs and the electric field induced PL enhancement from MNPs on the QDs. Here, due to the complexity of the CdSe-Ag system, we will only examine the CdSe-Au system. Based on the competing factors of quenching and electric field enhancement, the final apparent enhancement of the PL intensity can be depicted as:

$$\frac{I}{I_0} = P_Q \times P_E \tag{2}$$

Where I is the PL intensity of QDs over the MNP-coated GaAs surface; I_0 is the PL intensity of QDs without MNP coupling; P_Q and P_E are the quenching factor and enhancement factor, respectively, as described in equations 3 and 4 below. For the PL quenching part, an energy transfer mechanism has been successfully employed in various systems including dye-dye, MNP-dye, and QD-dye platforms.[202-204] In order to simplify our system, we will assume that for each QD there is only one MNP nearby. It should be noted that experimentally, based on the average surface coverage of the QDs and metal nanoparticles determined by AFM measurements, that there are *ca.* three-four QDs per Au particle. Based on the relative particle sizes and their surface coverage, statistically this ratio yields nearly 1 QD per MNP in close enough proximity to experience PL enhancement. The next closest QDs would be *ca* 40 nm from the MNP and based on our measurements may contribute *ca*. 20 % to the measured PL enhancement. Under these conditions, the PL quenching factor can be written as:[199,205,206]

$$P_Q = \frac{(d / R_Q)^{n_Q}}{1 + (d / R_Q)^{n_Q}} \tag{3}$$

Where d is the MNP-QD separation distance; R_Q is the Förster like radius at which 50% of the fluorescence is quenched; n_Q is the dependence of fluorescence quenching on the MNP-QD separation distance. For the Förster dipole-dipole energy transfer or fluorescence resonance energy transfer (FRET) mechanism,[202] the energy transfer quenching exhibits an $(d/R_Q)^6$ dependence. While for other mechanisms such as the nanosurface energy transfer (NSET) process, n_Q will equal 4.[199,207,208] Yun *et al.* has claimed to be able to distinguish between FRET and NSET processes by controlling the distance between a Au NP and a dye.[205] As such, by fitting our photoluminescence enhancement data we will also attempt to do the same.

For the PL enhancement part, it has been theoretically and experimentally demonstrated that the enhancement efficiency depends on the spectral overlap between donor emission and LSPR of MNPs and is proportional to the near field electric field intensity of the metal surface.[209-211] Here, we simplify the enhancement model *via* the following equation:

$$P_E = \left(\frac{R_E}{d}\right)^{n_E} + 1 \qquad (4)$$

Where R_E is a constant for the MNP-QD separation at where we observe twice the luminescence enhancement, d is the same MNP-QD separation distance in equation 3 and n_E is the distance dependence power.

To apply these models to our data, the experimental data of the Au-QD system (Figure 5.11) was fit using equation 2, combined with equations 3 and 4, where n_Q was set to 4 or 6 and R_Q was calculated directly for either the FRET or NSET models based on the materials. All of the other parameters, d, R_E, and n_E were left to be freely variable in the

fit. If the fit to the data is better for n_Q = 4, this would suggest that the NSET mechanism dominates the energy transfer quenching processes. However, if a better fit is obtained for n_Q = 6, this would be indicative of a FRET mechanism being the major contributor to the quenching of the QD PL. The fitting of our results for both n_Q = 4 and 6 are shown in Figure 5.12, in which the green and blue dashed lines represent the curves for quenching and electric field enhancement as a function of MNP-QD separation distance, respectively. From these results, it can be seen that when n_Q = 6 a much better fit to the data is found, suggesting that the FRET mechanism seems to dominate in our system. This finding is consistent with earlier studies of ZnS capped CdSe coupled to Au nanoparticles *via* peptide tethers.[199]

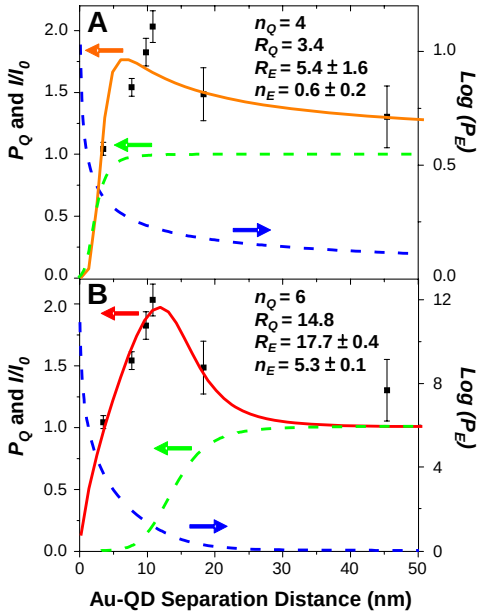

Figure 5.12. Fitting results for PL intensity enhancement for the Au-QD system. (A) For n_Q = 4 and (B) for n_Q = 6, respectively. The data points are from Figure 5.10. Only 0-50 nm of separation is shown to highlight the fit near the peak position. The orange and red solid lines represent the apparent PL enhancement as described in equation 2 for the NSET and FRET mechanisms. The green and blue dashed curves depict the quenching and enhancement factors as described in equations 3 and 4, respectively.

5.5. Summary

Using a patterned array of metal particles, photoluminescence enhancement for CdSe coupled to Au nanoparticles and CdSe coupled to Ag nanoprisms was investigated as a function of the CdSe-metal separation distance. The use of a patterned array allowed for the photoluminescence enhancement to be readily scaled between regions with and without metal particles and account for any scattering or differences in dielectric medium that could influence the determination of the relative enhancement, all in a single experiment. The PL enhancement of CdSe coupled to Au and Ag particles was found to peak at a factor of two at distances of ~ 11 nm and 8 nm, respectively. The resulting data can be explained by the competition between energy transfer quenching and plasmon-assisted enhancement of the QD photoluminescence and could be fit to a simple model combining these two effects. This simple platform which can be fabricated using directed assembly approaches should be readily adaptable to probing photoluminescence enhancement for a range of other materials.

CHAPTER VI

SPATIALLY SELECTIVELY TUNING OF QUANTUM DOT THIN FILM LUMINESCENCE

6.1. Synopsis

This chapter describes a simple post-synthetic method to create patterns of colloidal CdSe nanocrystals with different optical properties and/or surface modifications on solid surface with sub-micron spacing resolution. While post-synthetic schemes relying on photooxidation of QDs has been recently demonstrated in solution for tuning their optical properties, this often leads to reduced control over their resulting emissive properties due to aggregation that often results from oxidation in solution. Here we have employed a "lithosynthesis" approach to photochemically alter the surface chemistry of the quantum dots. In this process we are able to fine tune the optical properties of quantum dots, immobilized on a substrate through local photochemical oxidation and ligand exchange. As such, there is no issue of aggregation of the quantum dots and spectral changes show significantly reduced broadening as compared to processing in solution. These findings open an interesting way to nondestructively pattern quantum dot thin films. In addition to changing their local optical properties, the QDs that are patterned show an increased propensity for selectively binding of new molecules, making their surface chemical and optical properties re-configurable numerous times. Lastly, as this procedure can be employed with any conventional lithographic technique, this process is readily scalable for high throughput

nanofabrication. With the increasing interests of applying colloidal quantum dots in optical and electrical devices, bio-labeling and biosensing platforms, we expect this procedure will be of interest to the large community of scientists and engineers.

6.2. Introduction

Quantum dots have found numerous applications because of their exceptional features including high quantum yield, tunable wavelength of broad absorption with narrow PL spectra by size, and low photobleaching, which suggest their use for *in vivo* cellular labeling and *in vitro* biomolecular detection.[212-215] These applications would be greatly increased if one could create spatially addressable platforms of QDs with selective optical properties. In present technologies, to create patterned arrays of quantum dots, one is first required to synthesize QDs with different sizes to achieve the desired luminescent properties by controlling particle size. The size selectivity is limited by the synthetic platform being used and requires several processing steps. To pattern these structures, one then faces the challenge of placing the specific color of quantum dot of inertest in the correct location on a support using either specific chemical linkers or pre-patterned templates.[216-218] This could be very laborious and non-economical, as it first requires the synthesis of QDs with the desired sizes and then an approach to position them to a pre-decided location. It has recently been shown that by using photo-oxidation, the effective size of the QD can be modified post-synthetically to tune QD emission.[219-221] However, those experiments were all carried out in solution that can often lead to aggregation, resulting in undesirable spectral broadening and

inhomogeneity. Here we present a technology by utilizing a focus laser to "lithosynthesize" the QDs with the desired optical properties (Figure 6.1), which allows the directed patterning of QD materials to create features with selective wavelengths and whose luminescence may be locally modified by chemical addition to allow for the writing, reading and erasing of features. This also provides a localized means of chemically altering these materials by selective addition of new molecules making this approach amenable for selective patterning of sensors.

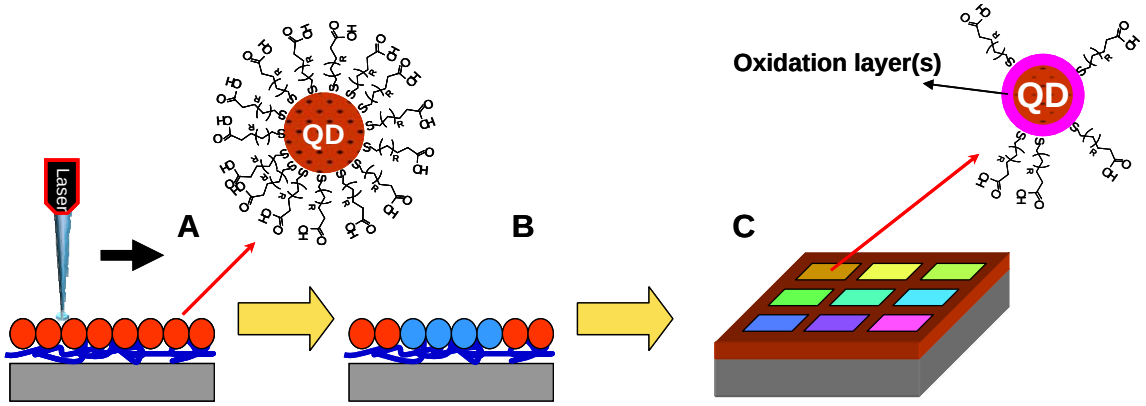

Figure 6.1. Photo-oxidation of CdSe by laser exposure with controlled exposure time. In aconfocal fluorescence microscope, a focused laser beam (~2 kW/cm2) was used to scan a 16-mecaptohexadecanoic acid (16-MHA) capped QD film (A) to create patterns of oxidized QDs (B). The 16-MHA molecules are decomposed during laser lithography and the outer layers of CdSe QDs were oxidized, and the oxidation degree of each pattern was controlled by the dwell time or strength of the laser beam with each different color of each array representing different PL wavelength (C).

6.3. Experimental Details

Immobilization of QDs onto Solid Support to Form a QD Film. A silicon or glass substrate was first cleaned by the base piranha solution (NH_4OH:H_2O_2:H_2O=1:1:4) for 10 min to form a hydroxyl terminated surface (This is a typical semi-conductor cleaning method, e.g. RCA-1). *Caution: the base piranha cleaning solution is highly corrosive*

and should be used very carefully. The substrate was then rinsed by ultrapure water (18.2 MΩ·cm, NANOpure Diamond, Barnstead, Iowa USA) and immersed into 1 mg/mL positively charged poly(diallyldimethylammonium chloride) (PDADMAC, Aldrich, 20 wt. % in water, M_w 100,000-200,000) in a 0.5 M NaCl aqueous solution for 20 min to allow for full absorption of a single layer. The polymer modified substrate was then immersed in 16-mercapto-1-hexadecanoic acid (16-MHA) capped CdSe QDs in aqueous solution for 8 hrs to form a thin film of QDs (*ca*. 1-2 layers). The resulting substrate was then further rinsed by ultrapure water to wash away weakly bound QDsSingle side polished GaAs(100) substrates.

Lithography and Imaging Processes. The lithography and imaging processes were carried out using a combined confocal fluorescence/AFM microscope (WITec Alpha300R, Germany) under ambient conditions (24 ± 2 ^{o}C) coupled with an argon ion laser with an Andor Peltier cooled (-70 ^{o}C) CCD detector. A Nikon high numerical aperture objective (100x, 0.9 NA) was used to focus the laser on a sample for both lithography and imaging. For lithography, a laser power up to 150 μW/μm^2 was used, while a lower laser power of 3 to 15 μW/μm^2 was used for imaging. At lower laser power, the same behavior was observed but the time required for photo-oxidation was much longer, whereby, the photo-oxidation of CdSe QDs was found to be negligible during the rapid integration time of ~ 50 ms/pixel. (For example, it takes a few hours to reach the maximum intensity under illumination of 15 μW/μm^2 laser, comparing to several seconds for 150 μW/μm^2 laser).

XPS Measurements. Three samples were prepared by drop casting of 50 μL of QD solution (~1 μM) on a cleaned silicon substrate. The samples were blown dry with nitrogen and then immersed in 1 mM 16-MHA/ethanol solution for 10 min. After removing the samples from the solution of 16-MHA, the substrates were rinsed by ethanol thoroughly. One sample was examined by XPS without further treatment, while the other two samples were exposed to UV/ozone for 4 min to reach the maximum photoluminescence intensity. One of these two samples was then subsequently re-immersed in 1 mM 16-MHA/ethanol solution for 10 min and then rinsed with copious amounts of ethanol. The XPS data were acquired with a Kratos Axis ULTRA X-ray photoelectron spectrometer equipped with a 165 mm hemispherical electron energy analyzer. The incident radiation was the Mg Kα X-ray line (1253.6 eV) with a source power of 180 W (15 kV, 12 mA). The analysis chamber was maintained at a steady base pressure of $< 6\times10^{-9}$ Torr during sample analysis. Survey scans of up 1100 eV binding energy were carried out at a analyzer pass energy of 160 eV with 1.0 eV steps and a dwell time of 300 ms. Multiplexed high-resolution spectra of the C(1s), S(2p), Cd(3d), and Se(3d) regions were taken at a pass energy of 40 eV with 0.1 eV steps and a dwell time of 60 ms. The survey and high-resolution spectra were obtained with averages of 5 and 50 scans, respectively. The C(1s) peak at 284.8 eV was set as a reference for all XPS peak positions to compensate for energy shifts due to the spectrometer work function.

6.4. Results and Discussion

Tuning the Optical Properties of CdSe QDs. Using a focused argon ion laser beam directed through a confocal microscope, the laser light is scanned across the film with different rates to photo-oxidized the QDs and thus generate arrays of QDs with different luminescent intensities and wavelengths. Figure 6.2 shows the typical photoluminescence as a function of time under a fixed laser at the same spot on a CdSe film. The intensity of the CdSe QD emission is selectively tuned by altering the laser dwell time on a region from ca. 0.25 s/μm to10 s/μm. Additionally, increased exposure time results in a continuous blue-shifting of the QD emission (Figure 6.3). As shown in Figure 6.3, the time-resolved spectra of the QDs under laser illumination were recorded with an integration time of about 40 ms and show both the change in photoluminescence intensity and the shift in the center emission wavelength. The fabricated pattern may then be imaged under lower laser intensity (~4 W/cm2). Figure 6.3A shows the confocal fluorescence image of lines written by ratsering the sample at 4, 2, 1, 0.8, 0.6, 0.4, 0.2, 0.1 μm/s respectively, from left to right then top to bottom. Figure 6.3B shows the shift in the photoluminescence peak wavelength for each feature. For low raster rates < 0.2 μm/s, the intensity in the center of the line was smaller than the background, but that of the edge was greater than the background due to the Gaussian beam profile. The lines on the peak center image became darker because of blue shifting. Under the optimal conditions, the emission wavelength of the CdSe QDs can be tuned (blue-shifted) up to 45 nm (Figure 6.4). The feature size of the patterned arrays depends on the diameter of laser spot striking the surface and in this configuration is diffraction limited yielding

feature sizes as small as ca. 300 nm. Optimal structures to date however have features > 1 micron in size.

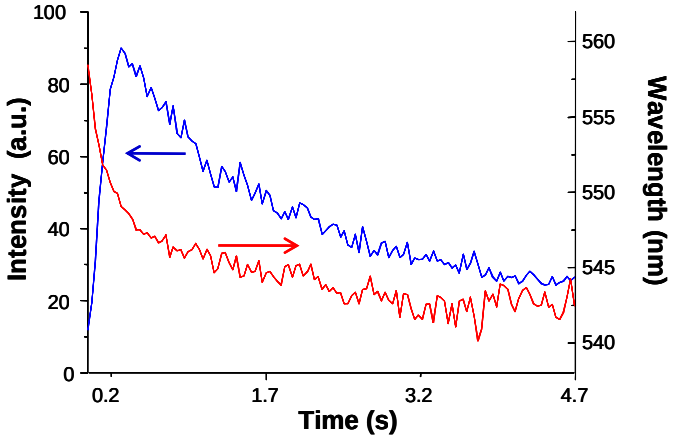

Figure 6.2. Change in luminescence intensity (left axis) and peak position (right axis) of a CdSe QD film under focused laser illumination.

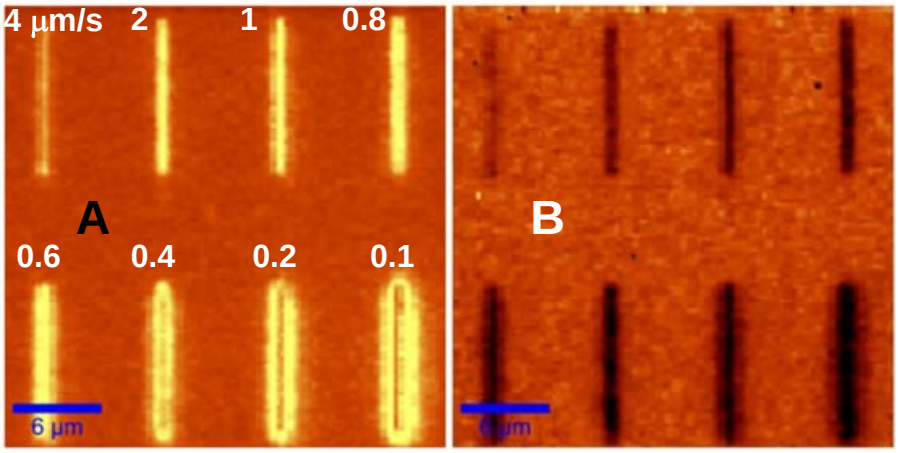

Figure 6.3. (A) Photoluminescence image (30 µm x 30 µm) and (B) peak position image (30 µm x 30 µm) of patterned CdSe QDs.

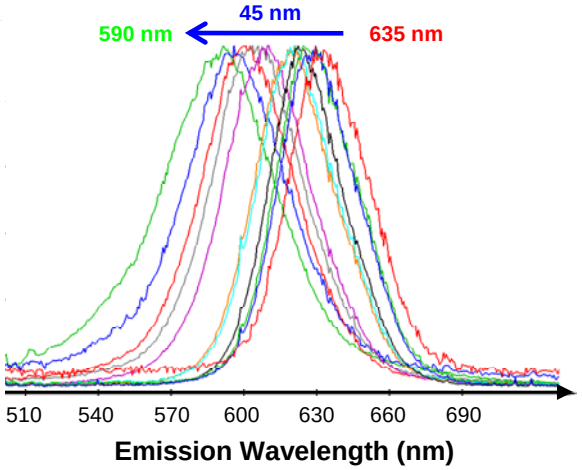

Figure 6.4. Selected spectra of QD emission under laser illumination. The spectra were normalized to the same intensity for the convenience of comparison. The center of the emission was blue shifted continuously from right to left controlled by the illumination time of the laser. The peak center may be blue shifted for ~45 nm under current experimental conditions.

The present processing method has as an advantage that only a single starting material is required. Moreover, by optimizing patterning conditions, the dispersity in the optical properties (i.e. luminescence wavelength) may possibly be reduced by precise control of the patterning conditions (i.e. materials that are not mondisperse could all be tuned to equivalent colors by the patterning process). Additionally, patterns may be created with high densities on any surface, making them extraordinarily useful for creating new optical display or sensing platforms. For example, they may be patterned on simple surfaces such as glass, or incorporated into composite materials, including polymers by encapsulation after patterning. Here we have successfully patterned the QDs onto TiO_2, sapphire, and Au surfaces. Moreover, any kind of features can be "written" selectively on CdSe QDs using this technique. Examples of confocal images

with various features created by laser lithography on CdSe QDs are shown in Figure 6.5. This could be very useful for the potential applications in 3-D optical storage media

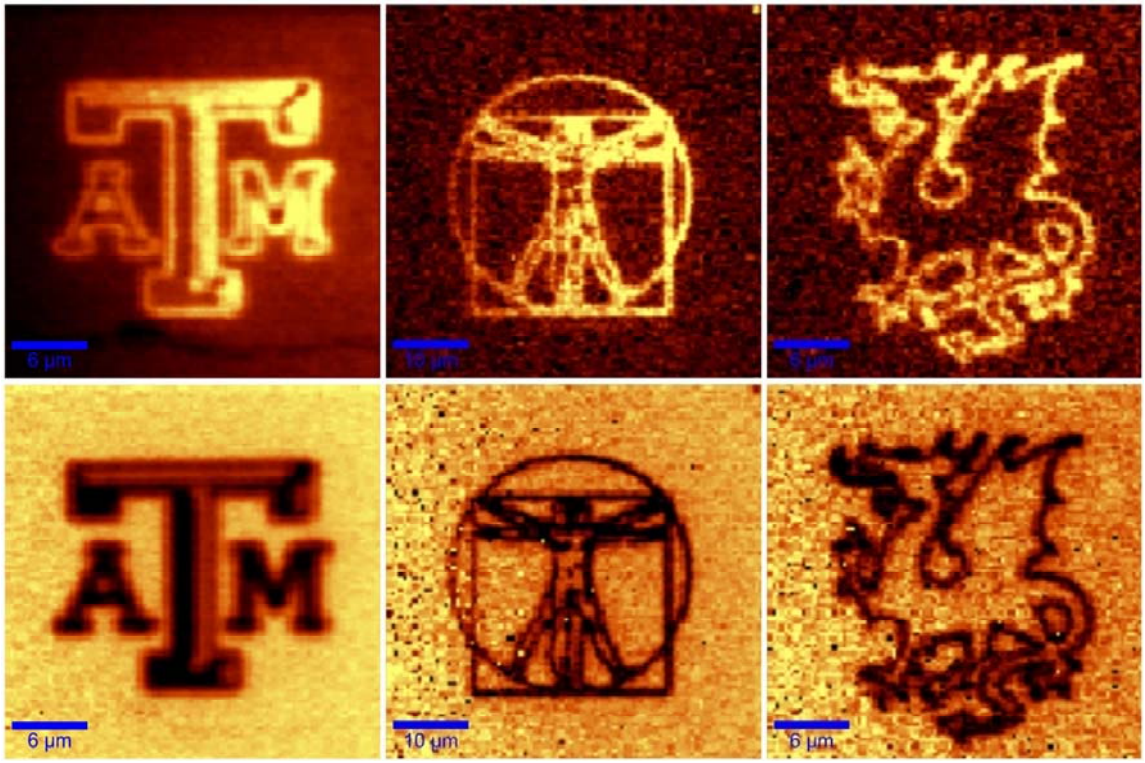

Figure 6.5. Each set of figures shows the PL intensity image (upper row) and the associated shift in wavelength (bottom row).

Rewritability of the Patterned QDs. We have observed that that the enhanced emission can be quenched back after resoaking the CdSe/sapphire into the 1 mM 16-MHA for 10 min and then can be "rewritten" by laser lithography at the same region, which suggests that the increased PL might be due to the removal of chemical bonds (i.e. S-CdSe bonds). The QD structures may be "written" to and "erased" for 12 cycles with little loss in feature fidelity or average ON/OFF luminescence ratio (Figure 6.6). This is accomplished by laser desorption/dissociation of the 16-MHA capping layer which may

then be replaced to "erase" the written feature. To confirm this assumption, we conducted the XPS experiments as shown in Figure 6.7. Under illumination, the thiol capping ligands can be removed by their photocatalytic oxidation to disulfide,[222] along with the formation of more complicated oxidized sulfur species. From XPS data, both Se and S were observed to be significantly oxidized after UV/ozone exposure and slight oxidation of C was also observed, while no noticeable changes in Cd were detected. For Se, the peak at around 54.4 eV is from CdSe and peak at 59.1 eV is known to arise from SeO_2.[223] For sulfur, the peak around centered around 160.5 eV corresponds to the thiolate chemisorbed (bounded) on Cd sites, while the peak from 164 eV to 167 eV may be attributed to the unbounded thiols and chemically (bounded) or physically (unbounded) absorbed dithiol species[224] on the CdSe surface as previously described from NMR data by Peng and co-workers.[225] The broad peak from 168 eV to 172 eV represent oxidized sulfur species which appear in this range of binding energies.

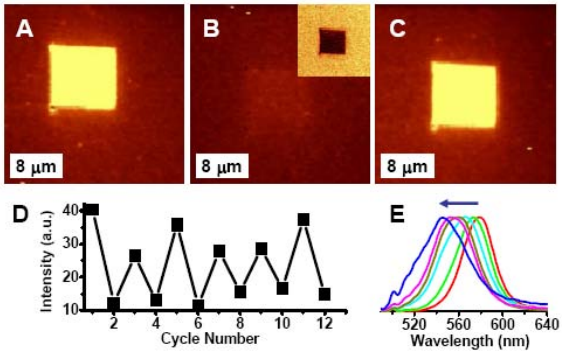

Figure 6.6. Demonstration of reversible surface modification of QDs. (A) A square is patterned onto the CdSe QD film where the QDs are partially oxidized and capping groups partially removed. (B) The sample is immersed in 16-MHA solution for 5 minutes (inset is the wavelength channel of the same region). (C) The surface is then re-patterned in the same location. (D) This process can be repeated many times with minimal signal loss. (E) During the cycles, the QD emission peak is continuously blue-shifted.

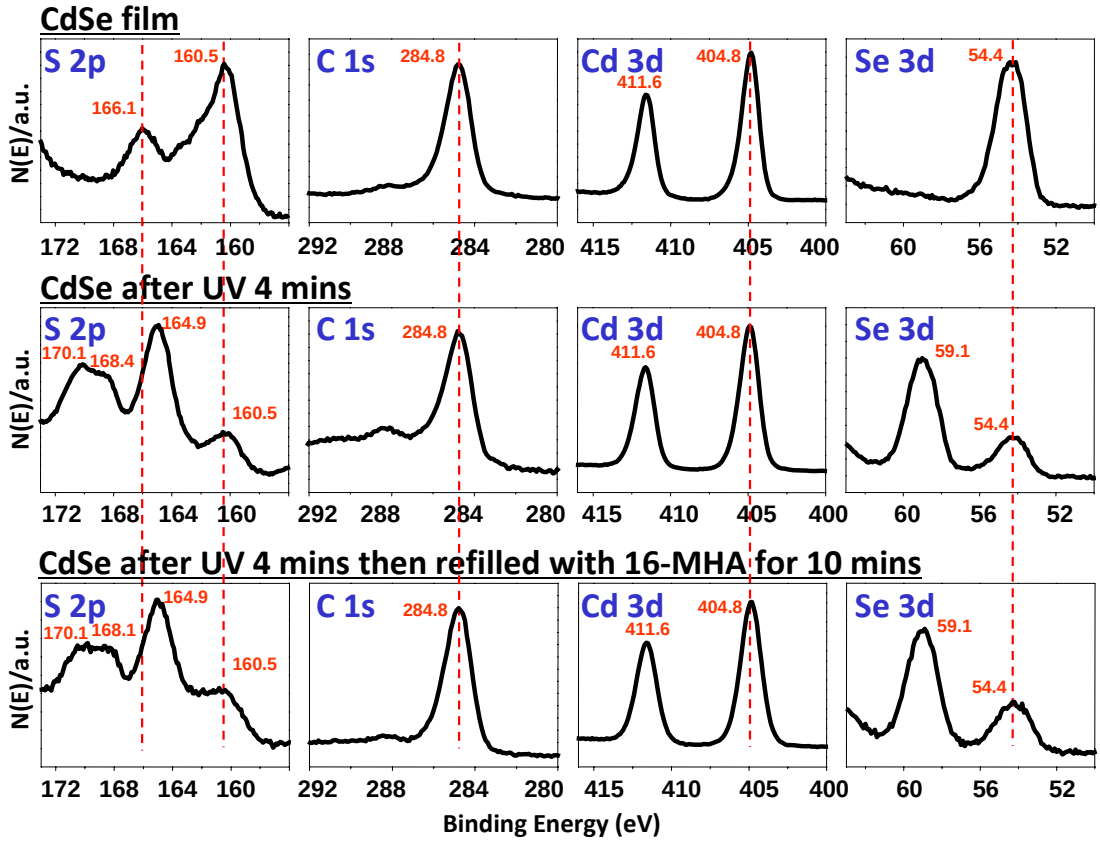

Figure 6.7. XPS spectra of a CdSe QD film before and after UV illumination and following UV illumination and re-exposure to 16-MHA.

The atomic concentrations of Cd, Se, S and C in each sample were obtained by integration of the peak areas with sensitivity corrections for each element using the Kratos Axis software (Table 6.1). The elemental ratio of (S + C) to (Cd + Se) of CdSe QDs decreases after UV treatment, from 6.4 to 2.4, and then increases back to 4.3 after exposing the film to 16-MHA (Table 6.1). This suggests that the 16-MHA surfactants are photo-oxidized under UV illumination and exposing the underlying CdSe which is then active for binding new 16-MHA molecules or other thiols.

Table 6.1. Elemental summary of Cd, Se, C and S in XPS spectra of Figure 6.7.

Elements	Atomic Concentration (%)		
	Original	After UV for 4 min	Refilled with 16-
Cd	9.96	19.08	11.83
Se	6.57	10.67	7.04
S	12.63	22.70	16.48
C	71.85	47.55	66.65

Insertion of Porphyrin Molecules into the Photopatterned Regions. The QD film samples were photo-patterned in air then transferred into 1 mM porphyrin thiol (TPy_3PF_4-SC_5SH) dissolved in CH_2Cl_2 for 10 min (Figure 3.1).[226] After insertion, the substrates were removed from the solution and were rinsed with dichloromethane and blown dry with streaming nitrogen. The control experiment was carried out by immersing the sample into pure CH_2Cl_2 for 10 min after photolithography. By comparing the control experiment (Figure 6.8A) to the sample following porphyrin attachment (Figure 6.8B, C), photoluminescence images showed that the porphyrin thiol had insertion to the surface. First, the CdSe photoluminescence was further quenched as compared to those films to which 16-MHA rebound to the surface, where the intensities of the first four lines in Figure 6.8 should go back to the background level. This increased quenching likely results from fluorescence resonant energy transfer (FRET) from the CdSe to the porphyrin. Luminescence images integrated over just the porphyrin fluorescence showed higher concentrations of porphyrin in the photo-oxidized regions as compared to the rest of the film, although some nonspecific binding of porphyrin was also observed (Figure 6.8C). Since nonspecific binding is surface dependent, one may expect to reduce this by surface modification. However, since

FRET is highly distance dependent, and the background CdSe QDs work as reference, from Figure 6.8B, the binding of porphyrin is very clear and is much better than directly using porphyrin fluorescence (Figure 6.8C) as a binding signal. The results demonstrate the feasibility for the attachment of various molecules in the regions of interest after selective photolithography on CdSe film.

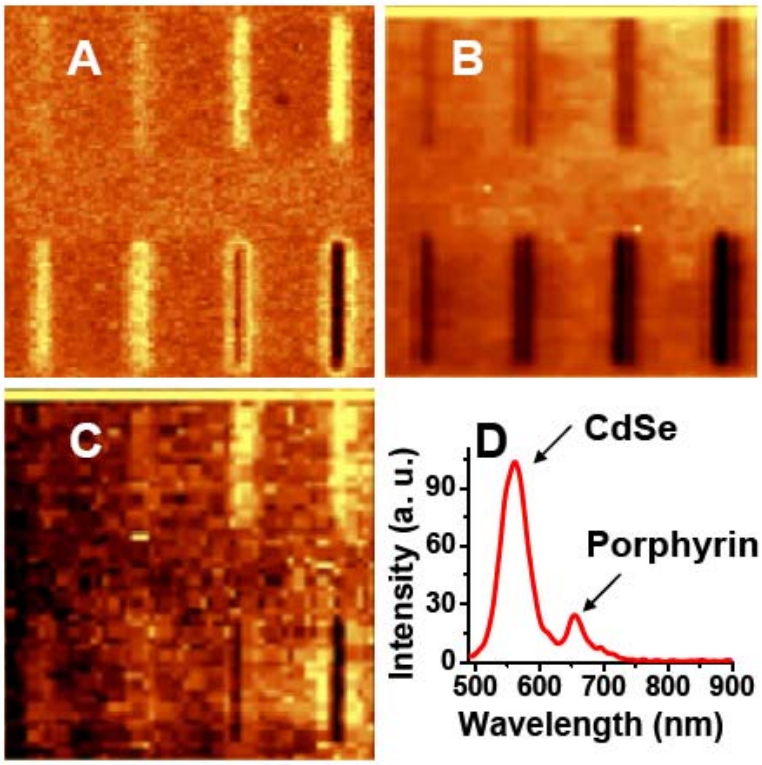

Figure 6.8. Demonstration of the application of this photolithography method to CdSe QD modification by additional ligands. Here molecules with thiol linkers can be selectively bound into the patterned regions. Photoluminescence images of samples that following patterning in air: a control sample that had been soaked in solvent CH_2Cl_2 (A); a sample that had been immersed in a porphyrin thiol solution (B,C) with luminescence image taken for the CdSe emission (B) and luminescence image of the porphyrin emission (C). (D) Emission spectrum of the porphyrin thiol modified sample with two emission peaks from CdSe and porphyrin respectively.

6.5. Summary

In summary, upon visible light illumination, the capping ligands of the QDs are photocatalytically oxidized along with the QDs themselves allowing for the selective modification of the local QD optical properties (emission intensity and wavelength). This method has many distinct advantages over other approaches for creating patterned arrays of QDs with different optical properties, in that only a single starting material is required and these patterned structures can be written optically using typically photolithographic techniques, affording ready industrial scale-up. Patterns can be created with high densities on any surface with appropriate modification, making them useful for creating displays or sensing platforms. The patterned structures can also be "erased" or modified by the selective addition of new surface ligands multiple times allowing the optical properties of the films to be reconfigurable.

CHAPTER VII

ULTRASENSITIVE COPPER(II) DETECTION USING PLASMON-ENHANCED AND PHOTO-BRIGHTENED LUMINESCENCE OF CDSE QUANTUM DOTS

7.1. Synopsis

Here we present a simple platform for using the enhanced emission of 16-mercaptohexadecanoic acid (16-MHA) capped CdSe QDs as a probe for ultrasensitive copper(II) detection. In this study, the photoluminescence (PL) of the QDs were first enhanced by Ag nanoprisms which were self-assembled on Si surfaces, and then further increased by photo-brightening. Using this approach, the control and different analytes could be readily probed all on a single platform using fluorescence microscopy. The enhanced PL intensity of CdSe QDs was selectively quenched in the presence of Cu^{2+}, accompanied by the emergence of a new red-shifted luminescence band. The quenching mechanism was found to be due to a cation exchange mechanism as confirmed by X-ray photoelectron spectroscopy (XPS) measurements. Herein, we have demonstrated that this simple methodology can offer a rapid and reliable detection of Cu^{2+} with a detection limit as low as 5 nM and a dynamic range up to 100 μM in a fixed fast reaction time of 5 minutes. The potential applications of this technique were tested in two ways: for mixed-ion solutions and in physiological fluids and both experiments exhibited good selectivity toward Cu^{2+}.

7.2. Introduction

Copper is among the most important transition metals in the human body. Copper is physiologically essential in various aspects such as bone formation, cellular respiration, connective tissue development and serves as a significant catalytic co-factor for several metalloenzymes,[227] and a deficiency of copper can lead to anemia or pancytopenia. Excessive amounts of copper can result in eczema, kidney disease, and damage to the central nervous system.[228] The Recommended Daily Allowance of copper suggested by National Research Council ranges from 1.5 to 3.0 mg for adults, 1.5 to 2.5 mg for children, and 0.4 to 0.6 mg for infants.[228] According to the guidelines for drinking-water quality of the World Health Organization (WHO), copper is identified as a "chemical of health significance in drinking-water".[57] Therefore, the importance of appropriate intake of copper in daily diet and its participating functions in physiological processes place an important emphasis on the detection of copper cations.

Among the detection techniques, there has been ongoing interest in exploiting metal nanoparticles (NPs) as prompt visual reporters for sensing species including transition metal ions, alkali ions, and biomolecules due to their change in surface plasmon absorption upon aggregation induced by the presence of the target molecules or ions.[229-232] However, the extinction spectra of metal NPs are usually broad and subtle changes of ion concentration might not be reflected from simply the color response of a NP solution or its extinction spectra. Recently, Chen and Rosenzweig developed the first example of copper and zinc ion probes using luminescent quantum dots (QDs) capped by different ligands in aqueous samples by taking advantage of the exceptional

features of QDs, including their high quantum yield, narrow emission spectra, and low rate of photobleaching.[233] To date there have been several research groups utilizing different types of functionalized QDs for the selective ion recognition including silver, copper, cadmium, and mercury.[234-240] Chou and coworkers[241] reported the use of 15-crown-5 capped CdSe/ZnS QDs as a sensing unit for K^+ *via* Förster type of energy transfer between two different size QDs. Ruedas-Rama *et al*. successfully used Zn^{2+} to "turn on" the emission of azamacrocycle-conjugated QDs,[242] while Ali *et al*. have demonstrated the ability of applying glutathione-capped ZnCdSe QDs to probe Pb^{2+} with a detection limit as low as 20 nM.[243] All of these developments show the promising potential of QD-based ion sensors for applications in biology, pharmacology and environmental science. Until now, these experiments were all performed in organic or aqueous media, with usually several mL of QD solutions and ion samples required for each fluorescence measurement. Additionally, clean-up of the poisonous QD solutions following the experiments and the ability to analyze trace amounts of sample at low concentrations however remain challenges in the applications of these materials. Most importantly, the thiol-derivatized molecules usually used as the capping ligands for QDs in order to make the ion analysis practical in aqueous media renders the quantum yield of the QDs very low (~ 1%),[244] which can have a detrimental impact on the overall sensitivity of these approaches.

In this chapter we present a simple and economical platform in which a thin film of CdSe QDs was deposited onto the Si surfaces pre-modified with Ag nanoprisms. The emission of CdSe QDs was enhanced by coupling with the surface plasmon of Ag

nanoprisms. Polymer layers, deposited using layer-by-layer assembly between the Ag and CdSe, are used to space the metal nanoparticles and QDs at the optimal separation distance for the maximum PL enhancement (Figure 7.1).[245] To further increase the sensitivity of QDs to their local environment, the CdSe QDs were also photobrightened by exposure to UV or laser light which resulted in photobrightening of the QDs, in an effort to achieve a lower detection limit and higher dynamic range.

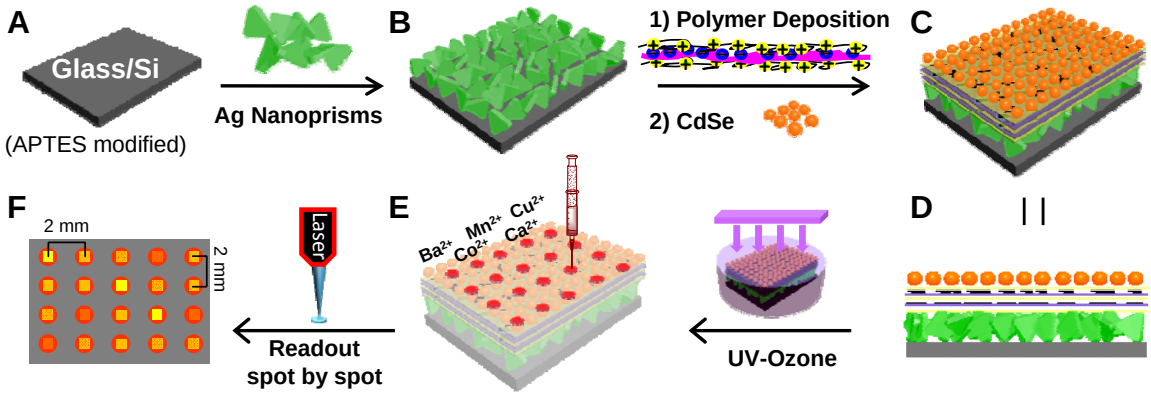

Figure 7.1. Schematic diagram showing the processes of fabrication of the enhanced CdSe device for ion-sensing. A glass or Si substrate was first cleaned and then modified with an APTES SAM (A). The substrate was next soaked in an aqueous solution of the citrate stabilized Ag nanoprisms allowing the nanoprisms to attach to the amine terminated surface (B). 5 layers of charged polymer were next deposited onto the Ag nanoprism modified surface terminating in PDADMAC. The negatively charged CdSe QDs of 6.5 nm in diameter were then adsorbed onto the outermost polymer layer (C). Panel (D) shows the side view of (C). The substrate was irradiated by UV-Ozone under pH 11 NH_4OH solution for 2.5 min and then blown dry with streaming nitrogen. Then, 2 μL of 100 μM ion samples were spotted onto the CdSe surface (E). After 5 min of reaction time, a confocal fluorescence microscope was used to measure the emission intensity of the CdSe QDs (F).

To address some of the above mentioned challenges of large sample volumes and disposal of large amounts of QD materials, here 2 μL of each different ion sample was dropped at predetermined spots marked on the back side of the glass substrate. This

simple approach provides enhanced PL of CdSe QDs in which only a thin film of QDs (less than 1 ng in CdSe weight) and trace amount of samples (2 μL) are required, greatly reducing potential cadmium contamination to the environment and unnecessary waste of samples. Additionally, this method allows the control (*i.e.* ion-free sample) and various ion samples to all be measured on the same platform using fluorescence imaging, aiding in eliminating variations from sample to sample. This simple platform can be readily fabricated using chemical self-assembly and adapted to diverse materials. Here, we demonstrated the capabilities of this approach using 16-MHA capped CdSe QDs as a selective probe for Cu^{2+} with a low detection limit (5 nM) and wide linear range (100 μM). The mechanism for copper ion detection was also investigated by using XPS and confocal fluorescence microscopy.

7.3. Experimental Details

Materials. The following inorganic salts were purchased from Sigma-Aldrich and used as received: copper(II) sulfate, potassium chloride, sodium chloride, nickel(II) chloride, barium(II) chloride, manganese(II) chloride, cobalt(II) chloride, calcium chloride and lead chloride. 3-aminopropyltriethoxylsilane (APTES) was purchased from Gelest, Inc. All other chemical reagents were purchased from Sigma-Aldrich and used as received without further purification. Single-side polished Si(100) wafers were obtained from Virginia Semiconductor Inc. High purity water (18.2 MΩ•cm, NANOpure Diamond, Barnstead) was used throughout the experiment. The piranha solution is a 1:3 (v/v) mixture of 30% H_2O_2 and concentrated H_2SO_4, and was used to

clean the Si wafers prior to use. *Caution: this solution reacts violently with organic materials and should be handled very carefully.*

Preparation of Silane Monolayers and Deposition of Silver Nanoprisms. The details of the preparation of silane monolayers have been described previously.[246] Briefly, self-assembled monolayers (SAMs) of APTES were formed by immersion of the freshly cleaned Si or glass substrate in 5 mM APTES in ethanol for 6 h. After being taken out from the solution of APTES, the SAM-modified substrates were rinsed with ethanol and blown dry under a nitrogen stream in preparation for deposition of silver nanoprisms. The samples were immersed in silver nanoprism solution overnight to allow a uniform absorbance of silver nanoprisms onto the APTES modified surface through electrostatic interaction.

Layer-by-layer Deposition of Polymers. A polymer spacer formed by layer-by-layer assembly was used to optimize the separation distance between the Ag and the CdSe to maximize the PL enhancement. The details of the polymer deposition on nanoprisms-modified substrates have been described elsewhere.[245] Here, a positively charged polymer solution was prepared by adding 0.5 M NaCl to an aqueous 5 μL/mL poly(diallyldimethylammonium chloride) (PDADMAC) (Aldrich, 20 wt. % in water, M_w 100,000-200,000) solution. For the negatively charged polymer solution, an aqueous solution of 1 mg/mL poly(sodium 4-styrenesulfonate) (PSS) (Aldrich, M_w 70,000) containing 0.5 M NaCl was used. An additional outermost layer terminating in a

positive layer of PDADMAC was deposited to allow for the further attachment of negatively charged 16-mercaptohexadecanoic acid terminated CdSe QDs.

X-ray Photoelectron Spectroscopy. XPS data were acquired with a Kratos Axis ULTRA X-ray photoelectron spectrometer equipped with a 165 mm hemispherical electron energy analyzer. The incident radiation was the monochromated Al Kα X-ray line (1487.7 eV) with a source power of 120 W (12 kV, 10 mA). The analysis chamber was maintained at a steady base pressure of 6×10^{-9} Torr during sample analysis. Survey scans of up to 1100 eV were carried out at a analyzer pass energy of 160 eV with 1.0 eV steps and a dwell time of 300 ms. Multiplexed high resolution scans of Cd(3d), C(1s), S(2p), Se(3d), Cu(2p), Ni(2p), and Co(2p) regions were taken at a pass energy of 40 eV with 0.1 eV steps and a dwell time of 60 ms. The survey and high resolution spectra were obtained with averages of 5 and 50 scans, respectively. The C(1s) peak at 284.8 eV was set as a reference for all XPS peak positions to compensate for energy shifts due to the spectrometer work function.

*Synthesis of CdS*e QDs. Trioctylphosphine oxide (TOPO)-passivated CdSe spherical nanocrystals of 6.5 ± 0.3 nm in diameter were synthesized from well-established solvothermal methods. The QDs were made water soluble through exchange of the capping ligand with 16-MHA (Figure 7.2).[170,247]

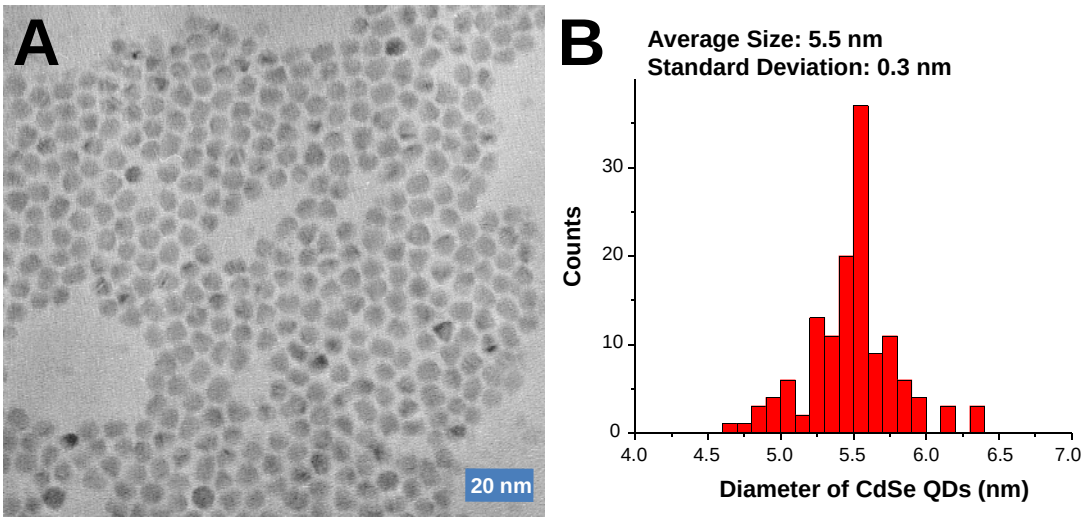

Figure 7.2. TEM images of (A) 6.5 nm and (B) size distribution of CdSe QDs.

Synthesis of Silver Nanoprisms. The Ag nanoprisms were synthesized by first creating spherical silver nanoparticles (NPs) by the reduction of $AgNO_3$ (Sigma, 99+% purity) with $NaBH_4$ at room temperature.[248] Here, 2 mL of 8 mM $NaBH_4$ solution was added dropwisely into 100 mL of 0.2 mM $AgNO_3$ and 0.4 mM sodium citrate aqueous solution. The color of this mixed solution turned to yellow immediately (Figure 7.3C) and was kept stirring for 30 min. The photochemical shape conversion of spherical Ag NPs into flat nanoprisms was carried out by exposure to a sodium lamp (50 W) for 14 h with a sample-source distance of ~ 3 cm.[248,249] The Ag NP solution was placed inside the glass water bath and monitored by thermometer to ensure that the temperature was below 30 ^{o}C. The color of the Ag NPs solution changed from yellow to green and then to light blue (Figure 7.3C) gradually during the period of illumination. The absorption spectra of Ag NPs were measured using UV-visible spectroscopy (USB-ISS-UV/Vis, Ocean Optics Inc.). The average edge length of triangular Ag nanoprisms measured by

transmission electron microscopy (TEM) were 70 ± 15 nm (Figure 7.3A-B). More than 90% of the Ag nanoparticles were found to be completely converted to nanoprisms.

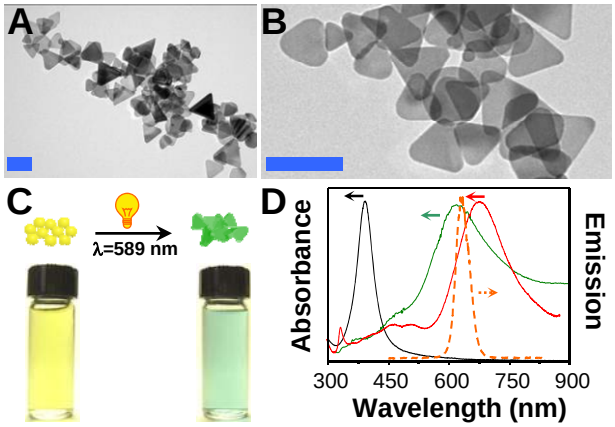

Figure 7.3. (A) TEM images of photoinduced Ag nanoprisms and (B) the enlarged view at a different region. The scale bars are 100 nm. (C) The Ag nanosphere (left) and nanoprism (right) solutions and (D) their corresponding absorption spectra displayed in solid black line and solid red line, respectively. The solid green line shows the UV-visible spectrum of Ag nanoprisms on APTES-modified glass covered with 5 layers of PSS:PDADMAC; and the orange line shows the photoluminescence of 6.5 nm CdSe QDs on top of 5 layers of PSS:PDADMAC.

Sample Imaging. As shown in Figure 7.1, 2 μL of 100 μM ion samples were dropped onto the CdSe surface one by one with a center-to-center spacing of *ca.* 2 mm. After 5 min of reaction time, the emission spectra of CdSe QDs were acquired spot by spot with a combined confocal fluorescence/atomic force microscope (WITec Alpha300 R, Germany) under ambient conditions (24 ± 2 ^{o}C). The photoluminescence spectra were collected using an Ar ion laser at 488 nm (~70 μW/μm^2) as the excitation source with a typical integration time of 36 ms/pixel. A Nikon 100x (0.9 NA) objective was utilized for imaging and spectral data acquisition and the laser was focused to a spot size

of ~1 μm^2. The spectral data were acquired with an Acton triple grating spectrometer with an Andor Peltier cooled (-66 ^oC) CCD detector. Each spectrum of the ion samples was averaged from 1000 different points on the surface with an integration time of 36 ms/pixel. TEM images of the synthesized CdSe nanoparticles were acquired using a JEOL 2010 transmission electron microscope at an acceleration voltage of 200 kV. Samples were prepared using copper grids from Ted Pella. A drop of CdSe solution, in toluene, or Ag nanoprism solution, in water, was dropped onto the grid and allowed to evaporate at room temperature.

For the determination of Cu^{2+} in simulated physiological backgrounds, solutions of 25 μM, 50 μM and 75 μM of copper ion were prepared by adding the $CuSO_4$ into as received and diluted (1:10 v/v and 1:20 v/v with high purity water) Dulbecco's Modified Eagle's Medium (DMEM D-5671, Sigma) solutions (Figure 7.4).

Component	g/L
Inorganic Salts	
$CaCl_2 \cdot 2H_2O$	0.2
$Fe(NO_3)_3 \cdot 9H_2O$	0.0001
$MgSO_4$	0.09767
KCl	0.4
$NaHCO_3$	3.7
NaCl	6.4
NaH_2PO_4	0.109
Amino Acids	
L-Arginine • HCl	0.084
L-Cysteine • 2HCl	0.0626
Glycine	0.03
L-Histidine • HCl • H_2O	0.042
L-Isoleucine	0.105
L-Leucine	0.105
L-Lysine • HCl	0.146
L-Methionine	0.03
L-Phenylalanine	0.066
L-Serine	0.042
L-Threonine	0.095
L-Tryptophan	0.016
L-Tyrosine • 2Na • $2H_2O$	0.10379
L-Valine	0.094
Vitamins	
Choline Chloride	0.004
Folic Acid	0.004
myo-Inositol	0.0072
Niacinamide	0.004
D-Pantothenic Acid • 1/2Ca	0.004
Pyridoxine • HCl	0.004
Riboflavin	0.0004
Thiamine • HCl	0.004
Other	
D-Glucose	4.5
Phenol Red • Na	0.0159
ADD	
L-Glutamine	0.584

Figure 7.4. Original composition of DMEM D5671.

7.4. Results and Discussion

Enhanced PL of CdSe QDs. The photoluminescent signals of the QDs in this study were enhanced in two ways: plasmonic enhancement and photo-enhancement. In our previous work, we have demonstrated that the luminescence of CdSe QDs can be locally enhanced by the electric field of Ag nanoprisms and can reach the maximum of *ca.* twice the original PL at a distance of ~ 8 nm between CdSe and Ag nanoprisms.[245] Here we used a modified method to photoconvert Ag nanoparticles into Ag nanoprisms with high yield (determined by TEM to be > 90%). As shown in Figure 7.3, the Ag nanoparticles were transformed into nanoprisms following the irradiation by a sodium lamp for 14 h. From the UV-vis spectra (Figure 7.3D), the absorption spectrum of Ag nanoprisms in solution exhibit an out-of-plane quadrupole (~ 334 nm), in-plane quadrupole (~ 466 nm), and in-plane dipole (~ 676 nm) plasmon resonance modes with no observable Ag nanoparticle band (expected to be *ca.* 400 nm). The Ag nanoprisms were then assembled onto an APTES-coated Si surface (Figure 7.1B). Following the attachment of Ag nanoprisms, a layer-by-layer deposition of oppositely charged polymers (PDADMAC:PSS) were cast sequentially onto the Ag-modified Si substrate as a spacer layer with the 16-MHA capped CdSe QDs (which carry a net negative charge at the assembly pH) absorbed onto the outermost polymer layer (PDADMAC) through electrostatic interactions (Figure 7.1C-D). As demonstrated in our previous work, the maximum field enhancement occurs at the distance of five layers of polymer (*ca.* 8 nm in thickness). Here an average PL enhancement of CdSe QDs by a factor of 2.5 was observed (Figure 7.5A).

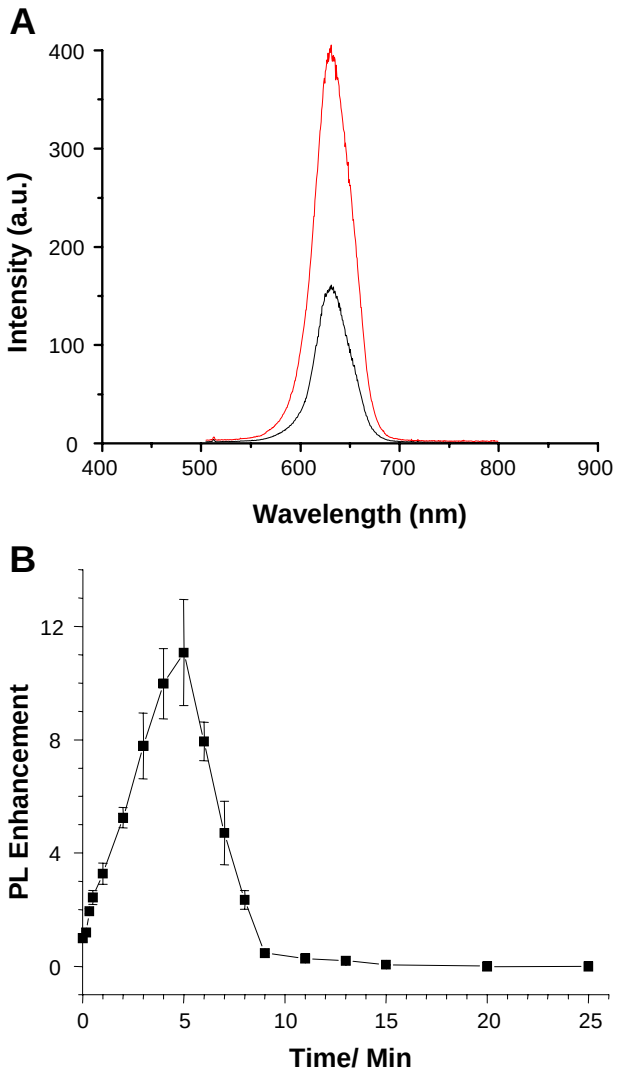

Figure 7.5. (A) Representative emission spectra of CdSe before (black line) and after (red line) plasmonic enhancement by Ag nanoprisms. (B) Relative photoluminescence enhancement of CdSe QDs which were irradiated by UV-Ozone for different durations, ranging from 0.2 to 25 min in pH 11 NH_4OH solution.

In addition to the plasmonic enhancement, it is known that the luminescence of the 16-MHA capped CdSe increase under light irradiation (photobrightening). Although the mechanisms explaining this type of photobrightening are still not well understood right now, there have been several groups reporting the plausible mechanisms in

analogue systems including passivation of surface states,[250-252] suppression of the ionization rate,[253,254] photochemical annealing,[255-257] and desorption of surfactants.[258] In our recent work, we have demonstrated that the removal of chemically bonded quencher (*i.e.* thiol capping ligands) is responsible for the photobrightening in our system.[259] In the present work we used the same stratagem to photobrighten the PL of CdSe in an NH_3 aqueous solution of pH 11, where detachment of the thiol capping agents along with concomitant Cd-OH formation was found to occur improved photostability of the QDs.[260] As displayed in Figure 7.5B, a maximum photobrightening of *ca.* 11-fold was observed following 5-min of UV/ozone irradiation. A dramatic decline in the PL intensity after 5 min, accompanied by a blue-shift of the emission wavelength (data not shown) however was also found due to the oxidation of the QD surface.[261] During illumination some damage of the supporting polymer film was also observed after 3 - 4 min of exposure resulting in an inhomogeneous distribution of QDs. As such, the illumination time to photobrighten the materials was fixed at 2.5 min in order to prevent any degradation of polymer layers but still yield a significant luminescence increase. In conjunction with increasing their luminescence, by photobrightening the QDs, we also expected that the partially removed capping reagent would also decrease the response time, thus accelerating the speed of sensing, as the removal of the capping ligands will raise the accessibility of Cu^{2+} from the bulk solution to the CdSe surface.

Luminescence Response of CdSe QDs to Metal Cations. The enhanced luminescence of the QD film was employed as a reporter for metal ions by spotting 2 μL

of 100 μM selected ion aqueous solutions onto the film (Figure 7.1E). It should be noted that one of the diagonal lines in the pattern served as a control experiment (*i.e.* only ultrapure H_2O was spotted at these locations). After 5 min of reaction time (*vide infra*), the luminescence of QDs was readout by a confocal laser scanning microscope (λ = 488 nm). As shown in Figure 7.6, the intensity of the emission maximum (λ = 627 nm) of the 16-MHA capped CdSe QDs was quenched selectively and effectively by copper ions by nearly 70% but minimally affected by other cations, as compared to the emission intensity of CdSe in the ion-free species (I_{blank}). Figure 7.7 shows the PL response of CdSe QDs to 100 μM of copper ions at different reaction times, which is indicative of a fast reaction rate of CdSe QDs with the copper ions. To better understand the selectivity of CdSe QDs toward copper ions, we conducted additional studies of this quenching behavior as described below.

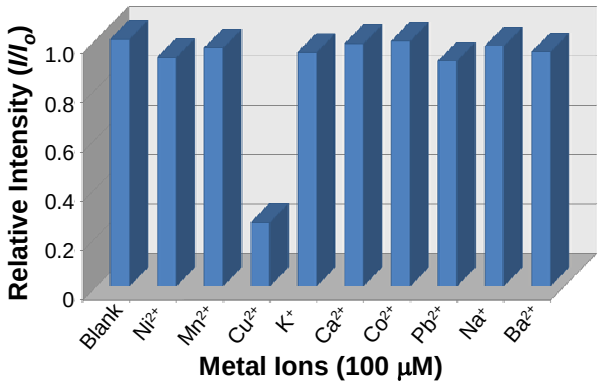

Figure 7.6. Effect of different ions (100 μM) on the luminescence intensity of CdSe QDs.

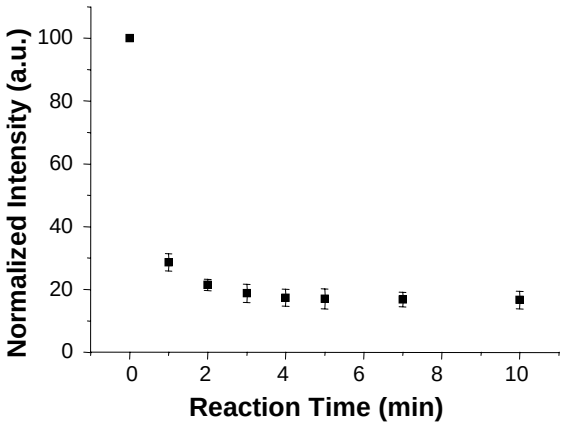

Figure 7.7. Normalized emission intensity of CdSe as a function of time after reacting with 100 μM Cu^{2+}.

Detection of Copper Ions Using 16-MHA Capped CdSe QDs Probe. As shown in Figure 7.8A, it was found that the presence of ultra-trace amounts (*ca.* 5 nM) of copper ions could produce a decrease in the PL of the CdSe QDs. For concentrations in excess of 100 μM however no further decrease in emission luminescence was observed, which suggests that no additional copper ion could be bound to the QD surface. Figure 7.8B describes the emission spectra of CdSe QDs as a function of copper ion concentration. The relative standard deviation of blank signal for 10 replicates was 1.2%. The dynamic range extends from *ca.* 5 nM to 100 μM and can produce a measurable quenching signal of as little as ~ 5%. Moreover, a slight red-shift (~ 5 nm) at the emission maximum along with the occurrence of a small shoulder peak at *ca.* 650 nm were observed with increasing copper ion concentration. The new peak is attributed to the formation of a new energy level associated with the CdSe-Cu^{+} species as demonstrated by Isarov *et al.*,[262] rendering a red-shift and broadening of the emission

maximum. The dependence of the PL quenching on copper ion concentration can be best expressed by typical Stern-Volmer quenching:

$$\frac{I_o}{I} = 1 + K_{sv}[Q],$$

where I_o and I are the PL intensity of QDs in an ion-free solution and at a given concentration of copper ions, respectively, $[Q]$ is the concentration of the quencher (*i.e.* copper ions) and K_{sv} is the Stern-Volmer constant. As shown in Figure 7.9, a linear relationship of I_o/I versus copper ion concentration is clearly observed (R^2 = 0.996) with K_{sv} = 6.5 x 10^4 M^{-1} for the CdSe QDs enhanced by both photobrightening and Ag nanoprisms. The dynamic range of the unmodified QDs however is much smaller and shows reduced linearity over the full range of concentration. This confirms that the CdSe QDs with enhanced PL can furnish a more efficient probe with higher sensitivity and a wider dynamic range toward copper ion detection.

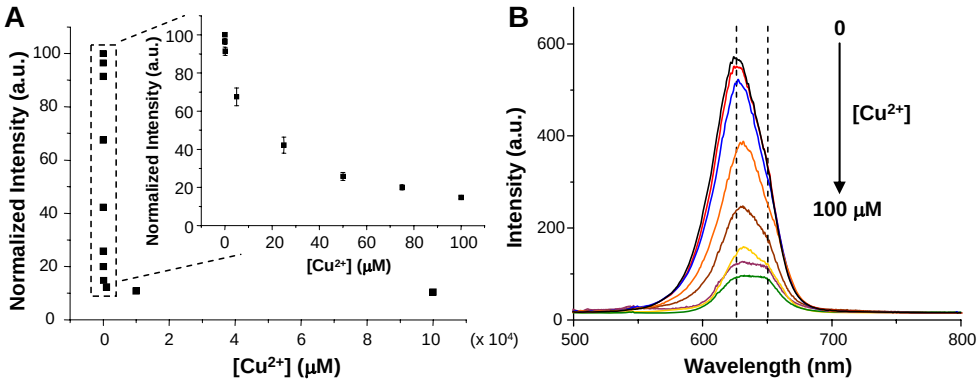

Figure 7.8. (A) Effect of various concentrations of Cu^{2+} ions on the luminescence of CdSe QDs. Concentration of Cu^{2+} from 0 to 100 μM: black line: 0, red line: 5 nM, blue line: 100 nM, orange line: 5 μM, brown line: 25 μM, gold line: 50 μM, plum line: 75 μM, green line: 100 μM. (B) Luminescence quenching of CdSe (λ_{max} = 626 nm) by Cu^{2+} ions. The inset in (A) magnifies the regions of lower concentration of Cu^{2+} (< 100 μM).

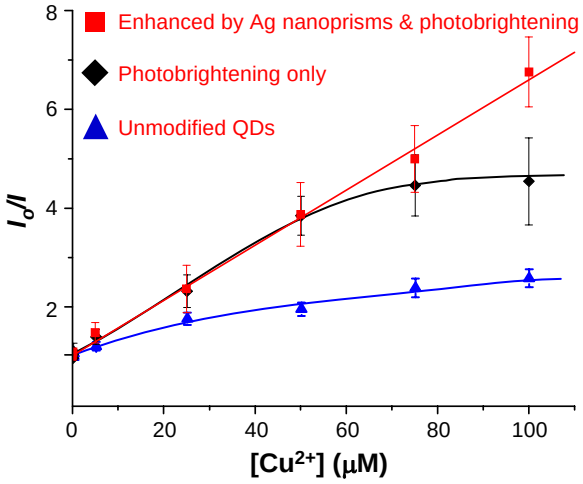

Figure 7.9. Stern–Volmer plot for the quenching of CdSe PL by Cu^{2+}. The solid red squares (■), black diamonds (◆), and blue triangles (▲) denote the CdSe QDs enhanced by both Ag nanoprisms and photobrightening, the photobrightened QDs, and the unmodified QDs, respectively. Note: the blue and black lines are added as a guide. The red line is a linear fit to the data.

Mechanism of Cu^{2+} Detection by CdSe QDs. XPS measurements were performed in an effort to investigate the mechanism of the selective copper ion response of CdSe QDs. Figure 7.10 shows high-resolution spectra of the S(2p), Se(3d), Cd(3d), C(1s), and Cu(2p) regions after treating the enhanced CdSe films with ion-free pure water (upper row) and 100 μM Cu^{2+} ions (bottom row). The sulfur peak reveals partial oxidation of the thiol capping groups prior to photo-brightening and plasmonic-enhancement (Figure 7.11), which demonstrates that oxidation of the 16-MHA by molecular oxygen in aqueous solutions cannot be avoided. It is worth pointing out that the decrease in atomic concentration of sulfur after photo-brightening (Table 7.1) is responsible for the increase in emission intensity, which is in agreement with our previous report.[259] Additionally, no significant peak shift or broadening was observed

for S(2p), Se(3d), Cd(3d), and C(1s) after the addition of Cu^{2+}, indicating that only the relative amount of each element was altered while the chemical structure of CdSe QDs remained intact. High-resolution photoelectron spectra of the Cu(2p) shows two peaks centering at 931.3 ± 0.1 eV and 951.2 ± 0.1 eV, which correspond to the $Cu(2p_{3/2})$ and $Cu(2p_{1/2})$, respectively. Interestingly, unlike previous reports which suggest the chemical replacement of surface Cd^{2+} ions by Cu^{2+} ions occurs,[263,264] we found that the peaks in the photoelectron spectra are characteristic of solely Cu^{+} rather than Cu^{2+} ions, which have been widely seen in copper(I) selenide and copper(I) sulfide compounds.[265,266] Additionally, no noticeable shake-up features in the Cu(2p) XPS was observed, further suggesting that only Cu(I) is present.[267] This is consistent with the thermodynamically allowed reduction of Cu^{2+} to Cu^{+} by the QDs, which in this case is rapid and complete, as previously shown by Isarov *et al.*[262] To elucidate the role of copper ions in quenching the QD PL, the atomic concentration of each element and the ratio of Cd to Se, and Cu to Se are summarized in Table 7.2, where the content of Se was assumed to be constant. Based on these data, it was found that the ratio of Cd:Se decreased with a concomitant increase of Cu:Se ratio as the concentration of copper ions used in the reaction was raised. This indicates that as the quenching occurs, Cu^{+} ions replace Cd^{2+}, rather than insert into Cd vacancies. The formation of copper(I) selenide by this process produces the associated red-shift and observed quenching phenomena. The ion-exchange processes is schematically illustrated in Figure 7.12 although the real model of the atomic exchange is much more complicated as recently described by the Alivisatos group.[268] The XPS data show that the ratio of Cd to Se and Cu to Se remain

almost unchanged for copper ion concentrations higher than 200 μM (Table 7.2) within the reaction time of 5 min. This suggests that under these conditions the surface of CdSe becomes saturated with Cu(I) and thus the Cd:Se ratio becomes constant. This result is consistent with the luminescence response where only a slight increase in PL quenching was observed at high copper ion concentrations (Figure 7.8A). It should be noticed that even after the ion exchange of Cu^{+} and Cd^{2+}, the surface stoichiometry of the CdSe was still Cd-rich.[269] As summarized in Table 7.2, we also examined the CdSe samples by XPS after treatment with Co^{2+} or Ni^{2+}, and no visible peak either from Co(2p) or Ni(2p) was detected (Figure 7.13), demonstrating the exquisite selectivity of this system for copper ions. It is also worth mentioning that the thiol group on the surface of the QDs can also interact with Cu^{2+} ions and then leave the surface, as reflected by the small decrease of sulfur content after copper ion treatment.

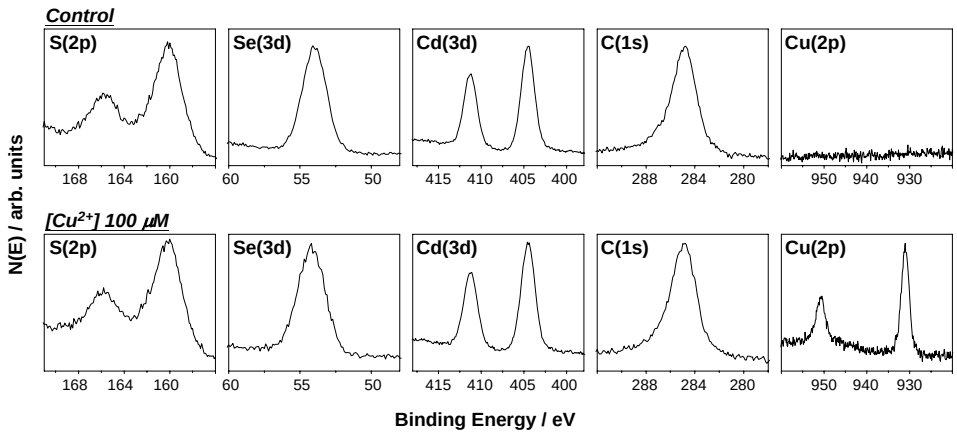

Figure 7.10. XPS spectra in the S(2p), Se(3d), Cd(3d), C(1s), and Cu(2p) regions of CdSe QDs after treatment with pure water (upper row) and 100 μM Cu^{2+} (bottom row).

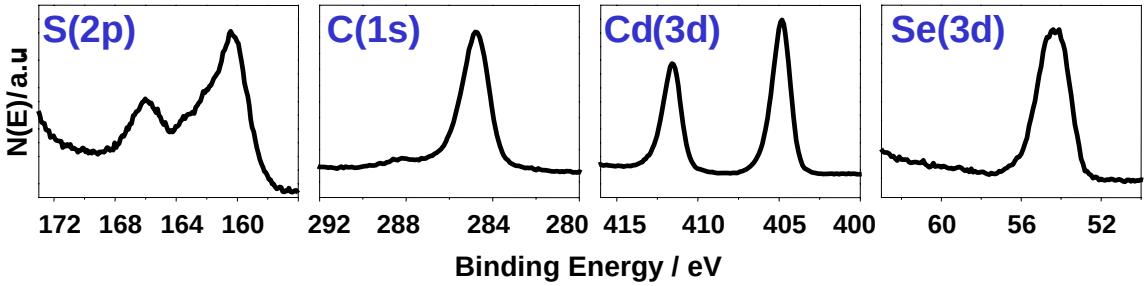

Figure 7.11. XPS spectra in the S(2p), C(1s), Cd(3d), and Se(3d) regions of CdSe QD film before UV illumination.

Table 7.1. Summary of atomic concentration of Cd, Se, S, C, and Cu of CdSe QDs samples before and after UV illumination. [a]The sample was reacted under pure water conditions. [b]The peak intensity is negligible.

Ion Concentration	Element / Atomic Concentration (%)				
	Cd	Se	S	C	Cu
Original	10.70	7.23	17.51	67.56	--[b]
Control[a]	9.80	6.01	14.99	69.20	--[b]

Table 7.2. Summary of atomic concentrations of Cd, Se, S, C, and Cu on the CdSe QDs samples after reaction at various ion concentrations. [a]The sample was reacted under pure water conditions. [b]No observable peak of Co(2p) (Figure 7.13). [c] No observable peak of Ni(2p) (Figure 7.13). [d]The peak intensity is negligible.

Ion Concentration		Element / Atomic Concentration (%)						
		Cd	Se	S	C	Cu	Cd/Se	Cu/Se
Control[a]		9.80	6.01	14.99	69.20	--[d]	1.63	0
$[Cu^{2+}]$	5 μM	9.16	7.14	14.35	70.16	0.19	1.49	0.03
	25 μM	9.08	7.16	14.42	69.49	0.85	1.47	0.14
	50 μM	8.82	7.22	13.94	68.91	2.11	1.42	0.34
	75 μM	8.44	7.49	13.95	68.62	2.50	1.30	0.39
	100 μM	7.74	7.10	13.99	68.86	3.31	1.27	0.54
	200 μM	7.87	7.17	16.11	68.92	3.93	1.11	0.63
	300 μM	7.80	7.10	14.00	69.20	3.92	1.11	0.64
$[Co^{2+}]$[b]	100 μM	9.86	6.07	14.92	69.15	--[d]	1.62	0

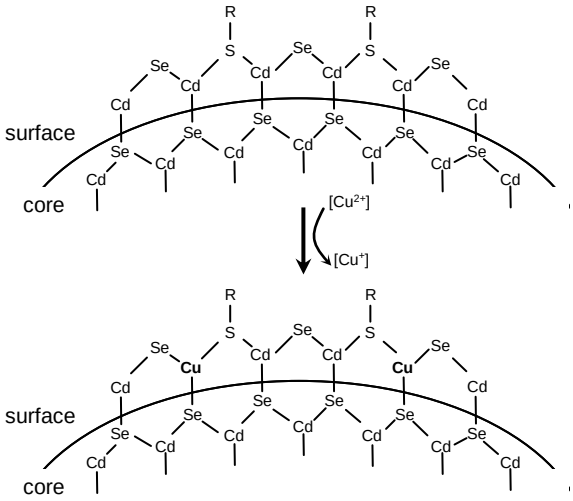

Figure 7.12. Schematic illustration of the surface structures of CdSe QDs and the cation exchange with copper ions. R represents the 16-MHA moiety.

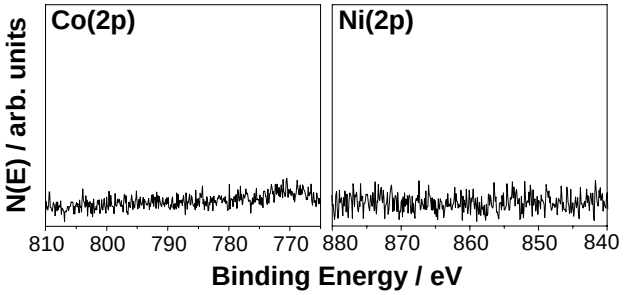

Figure 7.13. XPS spectra in the Co(2p) and Ni(2p) regions of CdSe QDs after treatment with 100 μM Co^{2+} and Ni^{2+} ions, respectively.

Cu^{2+} Detection in the Presence of Other Interfering Media. To evaluate the performance of CdSe QD films as a selective Cu^{2+} probe, an interference study was carried out as presented in Figure 7.14. It shows the 16-MHA capped CdSe QDs still exhibit good selectivity for Cu^{2+} ions in the presence of other metal ions including Ni^{2+}, Mn^{2+}, K^{+}, Ca^{2+}, Co^{2+}, Pb^{2+}, Na^{+}, and Ba^{2+}. To further assess the application of this

system in the simulated physiological media containing components similar to that of cell culture environment. The simulated samples were prepared by adding known amounts of copper ions at original and diluted DMEM solutions, which contain various inorganic salts, amino acids, vitamins, as well as additional supplementary components (Figure 7.4). As summarized in Table 7.3, the results show good agreement between the experimentally measured and known values for the concentration of copper ion in diluted DMEM solutions, while the rough values can be obtained in non-diluted ones. This indicates the feasibility of using this enhanced QD-based sensing system for copper ion detection in physiological samples.

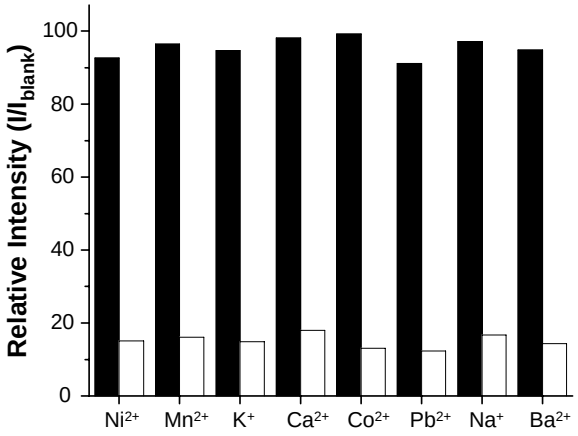

Figure 7.14. Response of CdSe intensity in the (■) absence and (□) presence of 100 μM Cu^{2+} solution containing a specific interfering metal ion of 100 μM.

Table 7.3. Application of enhanced luminescence of CdSe QDs for the determination of copper ion in simulated physiological media.

sample	$[Cu^{2+}]$ nominal (μM)	$[Cu^{2+}]$ found ± SD (μM)
1:20 diluted DMEM D-5671	25.00	21.74 ± 6.27
	50.00	56.31 ± 7.28
	75.00	79.15 ± 8.87
1:10 diluted DMEM D-5671	25.00	27.39 ± 4.31
	50.00	60.43 ± 10.11
	75.00	87.58 ± 12.72
commercial DMEM D-5671	25.00	30.22 ± 6.01
	50.00	68.20 ± 14.98

7.5. Summary

An ultrasensitive approach for Cu^{2+} ion detection and quantification sensing using CdSe QDs self-assembled on Si surfaces has been developed with a detection limit of 5 nM and a dynamic range extending up to 100 μM. The high sensitivity for copper ion detection results from a combination of the plasmon-enhanced luminescence of CdSe by Ag nanoprisms in conjunction with photobrightening using UV or visible light. PL quenching by Cu^{2+} is attributed to the selective ion-exchange processes between Cu^{2+} and Cd^{2+} at the CdSe QD surface as determined by XPS. Our studies have shown that this system is capable of Cu^{2+} detection even in mixtures of various metal salts and provides a practical example for the determination of copper in physiological media. This technique provides a means for different analytes of interest containing various

Cu^{2+} concentrations to be readily probed on a single platform, affording a simple tool for rapid, inexpensive, and ultrasensitive Cu^{2+} analysis.

CHAPTER VIII

CONCLUSIONS AND OUTLOOK

The aim of this dissertation was to further our development and application of the self-assembled monolayers for creating directed assemblies on both metal and semiconducting surfaces. In this work, we began by exploring the electronic properties of porphyrin molecules embedded in *n*-dodecanethiol monolayers on Au(111) surface by STM. Then we moved on to the investigation of the enhancement of CdSe emission via near-field coupling to the surface plasmon modes of self-assembled metal nanoparticles on GaAs. A potential application was also developed in which an ultrasensitive probe for Cu ion detection was developed based on photo-brightened and plasmon enhanced CdSe QDs.

In the course of these studies, three main projects have shown the utility of self-assembled monolayers for creating well defined nanoscale architectures on surfaces. In each case, SAMs are used as a powerful tool to address the desired topic of interest. In the first study, tripyridyl porphyrin molecules were anchored to a background matrix of dodecanethiol via self-assembly. The results from STM measurement indicated the low tunneling efficiency for this fluorinated porphyrin due to the poor orbital ovelap between the porphyrin macrocycle and the thiol tether. Future studies will aim to systematically explore how coordination of various M^{2+} metals into the porphyrin macrocycle and how selective removal of fluorine groups from the tether will influence the electon transport behavior of the porphyrins. This study provides a fundamental understanding of

molecular conduction that could be used to further optoelectronic and light harvesting applications.

In chapter IV, patterned silane SAMs were created on GaAs surface by conventional photolighography. Patterned arrays of Au or Ag nanostructures were thereby produced by using silane monolayers as linkers via electrostatic interactions. This platform was used to probe the plasmon enhanced photoluminescence of CdSe QDs as a function of metal-QD separation distance by directly scaling the luminescence intensities of QDs from coupled and noncoupled regions. By varying the separation distance between QDs and metal nanoparticles, we have shown that emission enhancement is strongly dependant on separation distance. The experimental results were also fit to a simple model consisting of two competitive mechanisms, energy transfer quenching and plasmon-assisted enhancement between QDs and metal nanoparticles. However, it was just an ensemble fitting without going down to a single nanoparticle level, therefore the exact mechanism responsible for the quenching or enhancement behavior cannot be determined at this stage. To predict and obtain the best performance of QD enhancement for sensing purposes, it will be necessary to improve the metal-QD sample design to more precisely control the relative positions, shapes and orientation of the metal nanostructures and their density on surface. Some of those challenges could be addressed with proper and fine control of the SAM patterning methods.

To evaluate the ability of enhanced emission of CdSe QDs for sensing applications, we take advantage of the system that we built for usingprobing enhanced

photoluminescence of CdSe QDs as new platform for ultrasensitive, cheap, and rapid copper(II) detection. Here enhanced emission of QDs is from the QDs coupled to the Ag nanoprisms self-assembld on Si and further photobrightened by UV or laser light to reach a higher emission intensity. We have demonstrated a detection limit of 5 nM and a dynamic range of 100 μM using this platform with very good selectivity even in physiological media. The quenching behavior is attributed to the ion-exchange between Cu^{2+} and Cd^{2+} on the CdSe QD surface.

Although we have successfully applied these self-assembly QD structures for ion-sensing, it is still a challenge to use this system in biosensing due to the toxicity of Cd^{2+} to organisms. In order to incorporate this platform into biological systems, we have synthesized the gold nanoclusters (less than 1 nm in diameter) in an attempt to replace the CdSe QDs. The Au nanoclusters have attracted a lot of interest due to their highly fluorescent, water-soluble, very stable properties.[270] Additionally, the emission wavelength of the Au nanoclusters can be tuned simply by controlling their size due the spatial confinement of free electrons in metal nanoclusters.[270] Most importantly, in contrast to semiconductor QDs which are typically toxic to biomolecules due to cadmium or lead ions, the Au nanoclusters are exceptionally attractive for *in vivo* cellular labeling and *in vitro* assay detection because of their ultrafine size and nontoxicity. The Au nanoclusters with blue and red emission capped by biologically compatible surfactants were synthesized as shown in Figure 8.1. The details of the synthetic methods were describes elsewhere.[271,272] Briefly, the blue emission Au nanoclusters were using a poly(amidoamine) (PAMAM) dendrimer as template. The Au

ions were mixed into the dendrimer solution and then incubated at 37 ^{o}C for 3 days to allow for the complete reduction of gold ions. For the red emission Au nanoclusters, the gold ions were added to bovine serum albumin (BSA) solution and the pH of the mixed solutions was adjusted to ~12 by NaOH. The reaction mixture was vigorously stirred at 37 ^{o}C for 12 h. Hopefully we will be able to use the enhanced fluorescence of the Au nanoclusters as a probe for biosensing in the future.

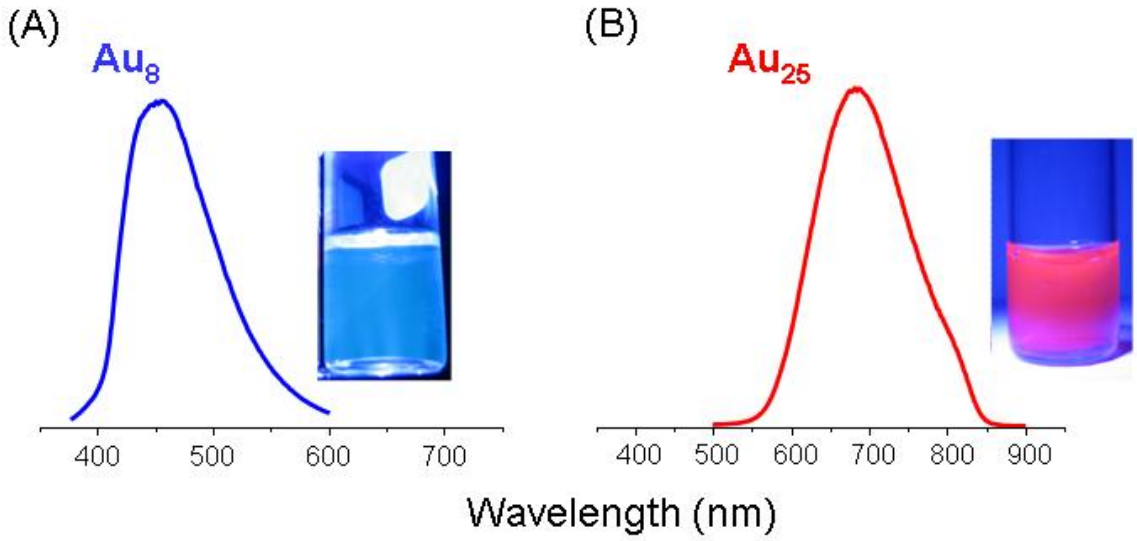

Figure 8.1. Au nanoclusters of (A) blue emission (λ_{exc}=366 nm) and (B) red emission (λ_{exc}=488 nm). Right figures show the photographs of Au nanocluster solutions under λ=398 nm UV light.

REFERENCES

(1) Bigelow, W. C. P., D. L.; Zisman, W. A. *J. Colloid Interface Sci.* **1946**, *1*, 513-538.

(2) Kuhn, H. M., D. *Physical Methodes in Chemistry*; Weissberger, A., Rossiter, B. W. ed.; Wiley: New York, 1972.

(3) Nuzzo, R. G. A., D. L. *J. Am. Chem. Soc.* **1983**, *105*, 4481-4483.

(4) Love, J. C.; Estroff, L. A.; Kriebel, J. K.; Nuzzo, R. G.; Whitesides, G. M. *Chem. Rev.* **2005**, *105*, 1103-1169.

(5) Chailapakul, O. S., L.; Xu, C.; Crooks, M. *J. Am. Chem. Soc.* **1993**, *115*, 12459-12467.

(6) Onclin, S.; Ravoo, B. J.; Reinhoudt, D. N. *Angew. Chem. Int. Ed.* **2005**, *44*, 6282-6308.

(7) McGovern, M. E.; Kallury, K. M. R.; Thompson, M. *Langmuir* **1994**, *10*, 3607-3614.

(8) Ulman, A. *Chem. Rev.* **1996**, *96*, 1533-1554.

(9) R. R. Rye, G. C. N., M. T. Dugger *Langmuir* **1997**, *13*, 2965-2972.

(10) Mukherjee, S. D.; Woodward, D. W. *Gallium Arsenide*; Wiley: New York, 1985.

(11) Pruniaux, B. R.; Adams, A. C. *Appl. Phys. Lett.* **1972**, *43*, 1980-1982.

(12) Baum, T.; Ye, S.; Uosaki, K. *Langmuir* **1999**, *15*, 8577-8579.

(13) McGuiness, C. L.; Blasini, D.; Masejewski, J. P.; Uppili, S.; Cabarcos, O. M.; Smilgies, D.; Allara, D. L. *ACS Nano* **2007**, *1*, 30-49.

(14) Krapchetov, D. A.; Ma, H.; Jen, A. K. Y.; Fischer, D. A.; Loo, Y.-L. *Langmuir* **2008**, *24*, 851 -856.

(15) Tkachenko, N. V.; Vuorimaa, E.; Kesti, T.; Alekseev, A. S.; Tauber, A. Y.; Hynninen, P. H.; Lemmetyinen, H. *J. Phys. Chem. B* **2000**, *104*, 6371-6379.

(16) Jin, Y.; Friedman, N.; Sheves, M.; He, T.; Cahen, D. *Proc. Natl. Acad. Sci.* **2006**, *103*, 8601-8606.

(17) Hou, T.; Greenlief, C. M.; Keller, S. W.; Nelen, L.; Kauffman, J. F. *Chem. Mater.* **1997**, *9*, 3181 - 3186.

(18) Martz, J.; Zuppiroli, L.; esch, F. N. *Langmuir* **2004**, *20*, 11428-11432.

(19) Rego, A. M. B. d.; Ferraria, A. M.; Beghdadi, J. E.; Debontridder, F.; Brogueira, P.; Naaman, R.; Vilar, M. R. *Langmuir* **2005**, *21*, 8765-8773.

(20) Vidoni, O.; Neumeier, S.; Bardou, N.; Pelouard, J.-L.; Schmid, G. *J. Cluster Sci.* **2003**, *14*, 325-336.

(21) Valsesia, A.; Colpo, P.; Meziani, T.; Lisboa, P.; Lejeune, M.; Rossi, F. *Langmuir* **2006**, *22*, 1763-1767.

(22) Shin, M.; Kwon, C.; Kim, S. K.; Kim, H. J.; Roh, Y.; Hong, B.; Park, J. B.; Lee, H. *Nano Lett.* **2006**, *6*, 1334-1338.

(23) Chow, D. C.; Lee, W.-K.; Zauscher, S.; Chilkoti, A. *J. Am. Chem. Soc.* **2005**, *127*, 14122-14123.

(24) Issle, J.; Pla-Roca, M.; Martinez, E.; Hartmann, U. *Langmuir* **2008**, *24*, 888-893.

(25) Cohen, J. D.; Sadowski, J. P.; Dervan, P. B. *J. Am. Chem. Soc.* **2008**, *130*, 402-403.

(26) Senaratne, W.; Andruzzi, L.; Ober, C. K. *Biomacromolecules* **2005**, *6*, 2427-2448.

(27) Ducker, R. E.; Janusz, S.; Sun, S.; Leggett, G. J. *J. Am. Chem. Soc.* **2007**, *129*, 14842 -14843.

(28) Kidambi, S.; Chan, C.; Lee, I. *Langmuir* **2008**, *24*, 224 -230.

(29) Duan, X.; Huang, Y.; Cui, Y.; Liber, C. M. In *Molecular Nanoelectronics*; Reed, M. A., Lee, T., Eds.; American Scientific Publishers: Stevenson Ranch, CA, 2003, p 199-227.

(30) Tans, S. J.; Dekker, C. *Nature* **2000**, *404*, 834-835.

(31) Ball, P. *Nature* **2000**, *406*, 118-120.

(32) Lee, K.-B.; Kim, E.-Y.; Mirkin, C. A.; Wolinsky, S. M. *Nano Lett.* **2004**, *4*, 1869 -1872.

(33) Sun, S.; Mendes, P.; Critchley, K.; Diegoli, S.; Hanwell, M.; Evans, S. D.; Leggett, G. J.; Preece, J. A.; Richardson, T. H. *Nano Lett.* **2006**, *6*, 345-350.

(34) Larsson, A.; Du, C.-X.; Liedberg, B. *Biomacromolecules* **2007**, *8*, 3511 -3518.

(35) Singhvi, R.; Kumar, A.; Lopez, G.; Stephanopoulos, G.; Wang, D.; Whitesides, G.; Ingber, D. *Science* **1994**, *264*, 696-698.

(36) Fan, Z.; Ho, J. C.; Jacobson, Z. A.; Yerushalmi, R.; Alley, R. L.; Razavi, H.; Javey, A. *Nano Lett.* **2008**, *8*, 20 -25.

(37) Naka, Y.; Eda, A.; Takei, H.; Shimizu, N. *J. Biosci. Bioeng.* **2002**, *94*, 434-439.

(38) Liu, G.-Y.; Xu, S.; Qian, Y. *Acc. Chem. Res.* **2000**, *33*, 457-466.

(39) Ding, L.; Li, Y.; Chu, H.; Li, X.; Liu, J. *J. Phys. Chem. B* **2005**, *109*, 22337-22340.

(40) Ku, S.-Y.; Wong, K.-T.; Bard, A. J. *J. Am. Chem. Soc.* **2008**, *130, 2392*.

(41) Ilic, B.; Yang, Y.; Craighead, H. *Appl. Phys. Lett.* **2004**, *85*, 2604-2606.

(42) Mendes, P. M.; Jacke, S.; Critchley, K.; Plaza, J.; Chen, Y.; Nikitin, K.; Palmer, R. E.; Preece, J. A.; Evans, S. D.; Fitzmaurice, D. *Langmuir* **2004**, *20*, 3766-3768.

(43) Ilic, B.; Craighead, H. G. *Biomed. Microdevices* **2000**, *2*, 317-322.

(44) Bruckbauer, A.; Zhou, D.; Kang, D.-J.; Korchev, Y. E.; Abell, C.; Klenerman, D. *J. Am. Chem. Soc.* **2004**, *126*, 6508-6509.

(45) Hoff, J. D.; Cheng, L.-J.; Meyhöfer, E.; Guo, L. J.; Hunt, A. J. *Nano Lett.* **2004**, *4*, 853-857.

(46) Minsky, M. 1957.

(47) Binnig, G.; Rohrer, H.; Gerber, C.; Weibel, E. *Appl. Phys. Lett.* **1982**, *40*, 178-180.

(48) Binnig, G.; Rohrer, H.; Gerber, C.; Weibel, E. *Phys. Rev. Lett.* **1983**, *50*, 120-123.

(49) F., M. *Phys. Rep.* **2004**, *399*, 175-225.

(50) Donhauser, Z. J.; Mantooth, B. A.; Kelly, K. F.; Bumm, L. A.; Monnell, J. D.; Stapleton, J. J.; Price, D. W., Jr.; Rawlett, A. M.; Allara, D. L.; Tour, J. M.; Weiss, P. S. *Science* **2001**, *292*, 2303-2307.

(51) Tans, S. J.; Devoret, M. H.; Dai, H.; Thess, A.; Smalley, R. E.; Geerligs, L. J.; Dekker, C. *Nature* **1997**, *386*, 474-477.

(52) Pomerantz, M.; Aviram, A.; McCorkle, R. A.; Li, L.; Aschott, A. G. *Science* **1992**, *255*, 1115-1118.

(53) Albrecht, T.; Guckian, A.; Ulstrup, J.; Vos, J. G. *Nano Lett.* **2005**, *5*, 1451-1455.

(54) Gittins, D. I.; Bethell, D.; Schiffrin, D. J.; Nichols, R. J. *Nature* **2000**, *408*, 67-69.

(55) David, I. G.; Donald, B.; David, J. S.; Richard, J. N. *Nature* **2000**, *408*, 67-69.

(56) Carroll, R. L.; Gorman, C. B. *Angew. Chem. Int. Ed.* **2002**, *41*, 4378-4400.

(57) Metzger, R. M. *Chem. Rev.* **2003**, *103*, 3803-3834.

(58) James, D. K.; Tour, J. M. *Chem. Mater.* **2004**, *16*, 4423-4435.

(59) Tkachenko, N. V.; Vuorimaa, E.; Kesti, T.; Alekseev, A. S.; Tauber, A. Y.; Hynninen, P. H.; Lemmetyinen, H. *J. Phys. Chem. B* **2000**, *104*, 6371-6379.

(60) Jin, Y.; Friedman, N.; Sheves, M.; He, T.; Cahen, D. *Proc. Natl. Acad. Sci.* **2006**, *103*, 8601-8606.

(61) Reed, M. A.; Zhou, C.; Muller, C. J.; Burgin, T. P.; Tour, J. M. *Science* **1997**, *278*, 252-254.

(62) Li, X.; He, J.; Hihath, J.; Xu, B.; Lindsay, S. M.; Tao, N. *J. Am. Chem. Soc.* **2006**, *128*, 2135-2141.

(63) Park, J.; Pasupathy, A. N.; Goldsmith, J. I.; Chang, C.; Yaish, Y.; Petta, J. R.; Rinkoski, M.; Sethna, J. P.; Abruna, H. D.; McEuen, P. L.; Ralph, D. C. *Nature* **2002**, *417*, 722-725.

(64) Venkataraman, L.; Klare, J. E.; Nuckolls, C.; Hybertsen, M. S.; Steigerwald, M. L. *Nature* **2006**, *442*, 904-907.

(65) Dunbar, T. D.; Cygan, M. T.; Bumm, L. A.; McCarty, G. S.; Burgin, T. P.; Reinerth, W. A.; Jone, L., II; Jackiw, J. J.; Tour, J. M.; Weiss, P. S.; Allara, D. L. *J. Phys. Chem. B* **2000**, *104*, 4880-4893.

(66) Kushmerick, J. G.; Naciri, J.; Yang, J. C.; Shashidhar, R. *Nano Lett.* **2003**, *3*, 897 -900.

(67) Chen, J.; Reed, M. A. *Chemical Physics* **2002**, *281*, 127-145.

(68) Weiss, E. A.; Chiechi, R. C.; Kaufman, G. K.; Kriebel, J. K.; Li, Z.; Duati, M.; Rampi, M. A.; Whitesides, G. M. *J. Am. Chem. Soc.* **2007**, *129*, 4336-4349.

(69) Morita, T.; Lindsay, S. *J. Am. Chem. Soc.* **2007**, *129*, 7262-7263.

(70) Wold, D. J.; Frisbie, C. D. *J. Am. Chem. Soc.* **2001**, *123*, 5549-5556.

(71) Donhauser, Z. J.; Mantooth, B. A.; Kelly, K. F.; Bumm, L. A.; Monnell, J. D.; Stapleton, J. J.; Price, D. W.; Rawlett, A. M.; Allara, D. L.; Tour, J. M.; Weiss, P. S. *Science* **2001**, *292*, 2303-2307.

(72) Samor´ı, P.; Rabe, J. P. *J. Phys.: Condens. Matter* **2002**, *14*, 9955-9973.

(73) Bumm, L. A.; Arnold, J. J.; Dunbar, T. D.; Allara, D. L.; Weiss, P. S. *J. Phys. Chem. B* **1999**, *103*, 8122-8127.

(74) Ishida, T.; Mizutani, W.; Aya, Y. O., H.; Sasaki, S. T., H. *J. Phys. Chem. B* **2002**, *106*, 5886-5892.

(75) Rawlett, A. M.; Hopson, T. J.; Nagahara, L. A.; Tsui, R. K.; Ramachandran, G.; Lindsy, S. M. *Appl. Phys. Lett.* **2002**, *81*, 3043-3045.

(76) Xu, B.; Tao, N. J. *Science* **2003**, *301*, 1221-1223.

(77) Wold, D. J.; Frisbie, C. D. *J. Am. Chem. Soc.* **2000**, *122*, 2970-2971.

(78) Holmlin, R. E.; Ismagilov, R. F.; Haag, R.; Mujica, V.; Ratner, M. A.; Rampi, M. A.; Whitesides, G. M. *Angew. Chem. Int. Ed.* **2001**, *40*, 2316-2320.

(79) Selzer, Y.; Salomon, A.; Cahen, D. J. *J. Am. Chem. Soc.* **2002**, *124*, 2886-2887.

(80) Ng, M.-K.; Yu, L. *Angew. Chem. Int. Ed.* **2002**, *41*, 3598-3601.

(81) Ng, M.-K.; Lee, D.-C.; Yu, L. *J. Am. Chem. Soc.* **2002**, *124*, 11862-11863.

(82) Yasuda, S.; Yoshida, S.; Sasaki, J.; Okutsu, Y.; Nakamura, T.; Taninaka, A.; Takeuchi, O.; Shigekawa, H. *J. Am. Chem. Soc.* **2006**, *128*, 7746-7747.

(83) Chen, J.; Reed, M. A.; Asplund, C. L.; Cassell, A. M.; Myrick, M. L.; Rawlett, A. M.; Tour, J. M.; Van Patten, P. G. *Appl. Phys. Lett.* **1999**, *75*, 624-626.

(84) Yang, G.; Qian, Y.; Engtrakul, C.; Sita, L. R.; Liu, G. *J. Phys. Chem. B* **2000**, *104*, 9059-9062.

(85) Hacker, C. A.; Batteas, J. D.; Garno, J. C.; Marquez, M.; Richter, C. A.; Richter, L. J.; Zee, R. D. v.; Zangmeister, C. D. *Langmuir* **2004**, *20*, 6195-6205.

(86) Blum, A. S.; Yang, J. C.; Shashidar, R.; Ratna, B. *Appl. Phys. Lett.* **2003**, *82*, 3322-3324.

(87) Nazin, G. V.; Qiu, X. H.; Ho, W. *Science* **2003**, *302*, 77-81.

(88) Elemans, J. A. A. W.; Hameren, R. v.; Nolte, R. J. M.; Rowan, A. E. *Adv. Mater.* **2006**, *18*, 1251-1266.

(89) Arima, V.; Fabiano, E.; Blyth, R. I. R.; Sala, F. D.; Matino, F.; Thompson, J.; Cingolani, R.; Rinaldi, R. *J. Am. Chem. Soc.* **2004**, *126*, 16951-16958.

(90) She, C.; Guo, J.; Irle, S.; Morokuma, K.; Mohler, D. L.; Zabri, H.; Odobel, F.; Youm, K.-T.; Liu, F.; Hupp, J. T.; Lian, T. *J. Phys. Chem. A* **2007**, *111*, 6832-6842.

(91) Lin, S.-Y.; Chen, I.-W. P.; Chen, C.-h.; Hsieh, M.-H.; Yeh, C.-Y.; Lin, T.-W.; Chen, Y.-H.; Peng, S.-M. *J. Phys. Chem. B* **2004**, *108*, 959-964.

(92) Chen, I.-W. P.; Fu, M.-D.; Tseng, W.-H.; Yu, J.-Y.; Wu, S.-H.; Ku, C.-J.; Chen, C.-h.; Peng, S.-M. *Angew. Chem. Int. Ed.* **2006**, *45*, 5814-5818.

(93) Yamada, H.; Imahori, H.; Nishimura, Y.; Yamazaki, I.; Ahn, T. K.; Kim, S. K.; Kim, D.; Fukuzumi, S. *J. Am. Chem. Soc.* **2003**, *125*, 9129-9139.

(94) Jiao, J.; Anariba, F.; Tiznado, H.; Schmidt, I.; Lindsey, J. S.; Zaera, F.; Bocian, D. F. *J. Am. Chem. Soc.* **2006**, *128*, 6965-6974.

(95) Wei, J. J.; Schafmeister, C.; Bird, G.; Paul, A.; Naaman, R.; Waldeck, D. H. *J. Phys. Chem. B* **2006**, *110*, 1301-1308.

(96) Vaughan, O. P. H.; Turner, M.; Williams, F. J.; Hille, A.; Sanders, J. K. M.; Lambert, R. M. *J. Am. Chem. Soc.* **2006**, *128*, 9578-9579.

(97) Ssenyange, S.; Anariba, F.; Bocian, D. F.; McCreery, R. L. *Langmuir* **2005**, *21*, 11105-11112.

(98) Chou, J.-H.; Kosal, M. E.; Nalwa, H. S.; Rakow, N. A.; Suslick, K. S. In *The Porphyrin Handbook*; Kadish, K. M., Smith, K. M., Guilard, R., Eds.; Academic Press: New York, 2000; Vol. 6, p 43-131.

(99) Imahori, H.; Fukuzumi, S. *Adv. Mater.* **2001**, *13*, 1197-1199.

(100) Amao, Y.; Asai, K.; Miyakawa, K.; Okura, I. *J. Porphyrins Phthalocyanines* **2000**, *4*, 19-22.

(101) Liu, Z.; Yasseri, A. A.; Lindsey, J. S.; Bocian, D. F. *Science* **2002**, *302*, 1543-1545.

(102) Yasseri, A. A.; Syomin, D.; Loewe, R. S.; Lindsey, J. S.; Zaera, F.; Bocian, D. F. *J. Am. Chem. Soc.* **2004**, *126*, 15603-15612.

(103) Hutchison, J. E.; Postlethwaite, T. A.; Murray, R. W. *Langmuir* **1993**, *9*, 3277-3283.

(104) Zak, J.; Yuan, H. o.; Ho, M.; Woo, L. K.; Porter, M. D. *Langmuir* **1993**, *9*, 2772-2774.

(105) Drain, C. M.; Batteas, J. D.; Flynn, G. W.; Milic, T.; Chi, N.; Yablon, D.; Sommers, H. *Proc. Natl. Acad. Sci.* **2002**, *99*, 6498-6502.

(106) Drain, C. M.; Smeureanu, G.; Patel, S.; Gong, X. C.; Garno, J.; Arijeloye, J. *New J. Chem.* **2006**, *30*, 1834-1843.

(107) Drain, C. M.; Lehn, J.-M. *Chem. Commun.* **1994**, 2313-2315.

(108) Drain, C. M.; Nifiatis, F.; Vasenko, A.; Batteas, J. D. *Angew. Chem. Int. Ed.* **1998**, *37*, 2344-2347.

(109) Drain, C. M.; Lehn, J.-M. *J. Chem. Soc., Chem. Commun.* **1994**, 2313-2315.

(110) Shirley, D. A. *Phys. Rev. B* **1972**, *5*, 4709-4714.

(111) Chan, Y.-H.; Lin, J.-T.; Chen, I.-W. P.; Chen, C.-h. *J. Phys. Chem. B* **2005**, *109*, 19161-19168.

(112) Varsanyi, G. *Assignments for Vibrational Spectra of SeVen Hundred Benzene Derivatives*; Wiley: New York, 1974.

(113) Chabal, Y. J. *Surf. Sci. Rep.* **1988**, *8*, 211-357.

(114) Anariba, F.; Viswanathan, U.; Bocian, D. F.; McCreery, R. L. *Anal. Chem.* **2006**, *78*, 3104-3112.

(115) Laibinis, P. E.; Whitesides, G. M.; Allara, D. L.; Tao, Y.-T.; Parikh, A. N.; Nuzzo, R. G. *J. Am. Chem. Soc.* **1991**, *113*, 7152-7167.

(116) Yang, G.; Liu, G.-y. *J. Phys. Chem. B* **2003**, *107*, 8746-8759.

(117) Poirier, G. E. *Chem. Rev.* **1997**, *97*, 1117-1128.

(118) Picraux, L. B.; Zangmeister, C. D.; Batteas, J. D. *Langmuir* **2006**, *22*, 174-180.

(119) Bumm, L. A.; Arnold, J. J.; Cygan, M. T.; Dunbar, T. D.; Burgin, T. P.; Jones, L.; Allara, D. L.; Tour, J. M.; Weiss, P. S. *Science* **1996**, *271*, 1705-1707.

(120) Cygan, M. T.; Dunbar, T. D.; Arnold, J. J.; Bumm, L. A.; Shedlock, N. F.; Burgin, T. P.; Jones, L.; Allara, D. L.; Tour, J. M.; Weiss, P. S. *Journal of the American Chemical Society* **1998**, *120*, 2721-2732.

(121) Moth-Poulsen, K.; Patrone, L.; Stuhr-Hansen, N.; Christensen, J. B.; Bourgoin, J.-P.; Bjørnholm, T. *Nano Lett.* **2005**, *5*, 783-785.

(122) Seferos, D. S.; Blum, A. S.; Kushmerick, J. G.; Bazan, G. C. *J. Am. Chem. Soc.* **2006**, *128*, 11260-11267.

(123) Zangmeister, C. D.; Picraux, L. B.; van Zee, R. D.; Yao, Y. X.; Tour, J. M. *Chemical Physics Letters* **2007**, *442*, 390-393.

(124) Wassel, R. A.; Fuierer, R. R.; Kim, N.; Gorman, C. B. *Nano Lett.* **2003**, *3*, 1617-1620.

(125) Ramachandran, G. K.; Hopson, T. J.; Rawlett, A. M.; Nagahara, L. A.; Primak, A.; Lindsay, S. M. *Science* **2003**, *300*, 1413-1416.

(126) Moore, A. M.; Dameron, A. A.; Mantooth, B. A.; Smith, R. K.; Fuchs, D. J.; Ciszek, J. W.; Maya, F.; Yao, Y.; Tour, J. M.; Weiss, P. S. *J. Am. Chem. Soc.* **2006**, *128*, 1959-1967.

(127) Di Ventra, M.; Kim, S. G.; Pantelides, S. T.; Lang, N. D. *Phys. Rev. Lett.* **2001**, *86*, 288 - 291.

(128) Cornil, J.; Karzazi, Y.; Bre´das, J. L. *J. Am. Chem. Soc.* **2002**, *124*, 3516-3517.

(129) Lang, N. D.; Avouris, P. *Phys. Rev. B* **2000**, *62*, 7325 - 7329.

(130) Seminario, J. M.; Zacarias, A. G.; Tour, J. M. *J. Am. Chem. Soc.* **2000**, *122*, 3015-3020.

(131) Hallbäck, A.-S.; Poelsema, B.; Zandvliet, H. J. W. *ChemPhysChem* **2007**, *8*, 661-665.

(132) Tao, Y.-T.; Wu, C.-C.; Eu, J.-Y.; Lin, W.-L.; Wu, K.-C.; Chen, C.-h. *Langmuir* **1997**, *13*, 4018-4023.

(133) Kim, Y. K.; Danner, A. J.; Raftery, J. J.; Choquette, K. D. *IEEE* **2005**, *11*, 1292-1298.

(134) Pellerin, J. G.; Shedd, G. M.; Griffis, D. P.; Russell, P. E. *J. Vac. Sci. Technol. B* **1989**, *20*, 1810-1812.

(135) Takado, N.; Asakawa, K.; Yuasa, T.; Sugata, S.; Miyauchi, E.; Hashimoto, H.; Ishii, M. *Appl. Phys. Lett.* **1987**, *50*, 1891-1893.

(136) Ochiai, Y.; Gamo, K.; Namba, S. *J. Vac. Sci. Technil. B* **1983**, *1*, 1047-1056.

(137) Sugimoto, Y.; Taneya, M.; Hidaka, H.; Akita, K. *J. Appl. Phys.* **1990**, *68*, 2392-2399.

(138) Sugimoto, Y.; Taneya, M.; Akita, K.; Hidaka, H. *J. Appl. Phys.* **1990**, *68*, 6415-6420.

(139) Wong, H. F.; Green, D. L.; Liu, T. Y.; Lishan, D. G.; Bellis, M.; Hu, E. L.; Petroff, P. M.; Holtz, P. O.; Merz, J. L. *J. Vac. Sci. Technol. B* **1989**, *6*, 1906-1917.

(140) Gamo, K.; Miyake, H.; Yuba, Y.; Namba, S.; Kasahara, H.; Sawaragi, H.; Aihara, R. *J. Vac. Sci. Technol. B* **1988**, *6*, 2124-2127.

(141) Jun, Y.; Zhu, X.-Y.; Hsu, J. W. P. *Langmuir* **2006**, *22*, 3627-3632.

(142) Ding, X.; Moumanis, K.; Dubowski, J. J.; Tay, L.; Rowell, N. L. *J. Appl. Phys.* **2006**, *99*, 054701/1-054701/6.

(143) McGuiness, C. L.; Shaporenko, A.; Mars, C. K.; Uppili, S.; Zharnikov, M.; Allara, D. L. *J. Am. Chem. Soc.* **2006**, *128*, 5231-5243.

(144) Dulcey, C. S.; Jr, J. H. G.; Krauthamer, V.; Stenger, D. A.; Fare, T. L.; Calvert, J. M. *Science* **1991**, *252*, 551-554.

(145) Tiberio, R. C.; Craighead, H. G.; Lercel, M.; Lau, T.; Sheen, C. W.; Allara, D. L. *Appl. Phys. Lett.* **1993**, *62*, 446-448.

(146) Janes, D. B.; Kolagunta, V. R.; Batistuta, M.; Walsh, B. L.; Andres, R. P.; Liu, J.; Dicke, J.; Lauterbach, J.; Pletcher, T.; Chen, E. H.; Melloch, M. R.; Peckham, E. L.; Ueng, H. J.; Woodall, J. M.; Lee, T.; Reifenberger, R.; Kubiak, C. P.; Kasibhatla, B. *J. Vac. Sci. Technol. B* **1999**, *17*, 1773-1778.

(147) Graf, D.; Frommenwiler, M.; Studerus, P.; Ihn, T.; Ensslin, K.; Driscoll, D. C.; Gossard, A. C. *J. Appl. Phys.* **2006**, *99*, 537071.

(148) Hyon, C. K.; Choi, S. C.; Hwang, S. W.; Ahn, D.; Kim, Y.; Kim, E. K. *Appl. Phys. Lett.* **1999**, *75*, 292-295.

(149) Magno, R.; Bennett, B. R. *Appl. Phys. Lett.* **1997**, *70*, 1855.

(150) Snow, E. S.; Campbell, P. M.; Perkins, F. K. *Appl. Phys. Lett.* **1999**, *75*, 1476-1478.

(151) Song, H. Z.; Nakata, Y.; Okada, Y.; Miyazawa, T.; Ohshima, T.; Takatsu, M.; Kawabe, M.; Yokoyama, N. *Physical E* **2004**, *21*, 625-630.

(152) Snow, E. S.; Campbell, P. M. *Science* **1995**, *270*, 1639-1641.

(153) Cho, Y.; Ivanisevic, A. *Langmuir* **2006**, *22*, 8670-8674.

(154) A. Vilan, A. S., D. Cahen *Nature* **2000**, *404*, 166-168.

(155) Lee, T.; Chen, N.-P.; Liu, J.; Andres, R. P.; Janes, D. B.; Chen, E. H.; Melloch, M. R.; Woodall, J. M. *Appl. Phys. Lett.* **2000**, *76*, 212-214.

(156) Loo, Y.-L.; Lang, D. V.; Rogers, J. A.; Hsu, J. W. P. *Nano Lett.* **2003**, *3,* 913-917.

(157) Reinhard, B. M.; Siu, M.; Agarwal, H.; Alivisatos, A. P.; Liphardt, J. *Nano Lett.* **2005**, *5*, 2246-2252.

(158) Sönnichsen, C.; Reinhard, B. M.; Liphardt, J.; Alivisatos, A. P. *Nat. Biotech.* **2005**, *23*, 741-745.

(159) Zhang, X.; Zhao, J.; Whitney, A. V.; Elam, J. W.; Duyne, R. P. V. *J. Am. Chem. Soc.* **2006**, *128*, 10304-10309.

(160) Lyandres, O.; Shah, N. C.; Yonzon, C. R.; Jr., J. T. W.; Glucksberg, M. R.; Duyne, R. P. V. *Anal. Chem.* **2005**, *77*, 6134-6139.

(161) Hecker, N. E.; pfel, R. A. H.; Sawaki, N.; Maier, T.; Strasser, G. *Appl. Phys. Lett.* **1999**, *75*, 1577-1579.

(162) Shimizu, K. T.; K.Woo, W.; Fisher, B. R.; Eisler, H. J.; Bawendi, M. G. *Phys. Rev. Lett.* **2002**, *89*, 117401-1--117401-4.

(163) Kulakovich, O.; Strekal, N.; Yaroshevich, A.; Maskevich, S.; Gaponenko, S.; Nabiev, I.; Woggon, U.; Artemyev, M. *Nano Lett.* **2002**, *2*, 1449-1452.

(164) Okamoto, K.; Niki, I.; Shvartser, A.; Narukawa, Y.; Mukai, T.; Scherer, A. *Nature Mater.* **2004**, *3*, 601-605.

(165) Biteen, J. S.; Pacifici, D.; Lewis, N. S.; Atwater, H. A. *Nano Lett.* **2005**, *5*, 1768-1773.

(166) Pompa, P. P.; Martiradonna, L.; Torre, A. D.; Sala, F. D.; Manna, L.; Vittorio, M. D.; Calabi, F.; Cingolani, R.; Rinaldi, R. *Nature Nanotech.* **2006**, *1*, 126-130.

(167) Murphy, C. J. *Nature Mater.* **2007**, *6*, 259-260.

(168) Jun, Y.; Zhu, X.-Y.; Hsu, J. W. P. *Langmuir* **2006**, *22*, 3627-3632.

(169) Peng, Z. A.; Peng, X. *J. Am. Chem. Soc.* **2001**, *123*, 183-184.

(170) Reiss, P.; Bleuse, J.; Pron, A. *Nano Lett.* **2002**, *2*, 781-784.

(171) Aldana, J.; Wang, Y. A.; Peng, X. *J. Am. Chem. Soc.* **2001**, *123*, 8844-8850.

(172) Frens, G. *Nature Phys.Sci.* **1973**, *241*, 20-22.

(173) Lee, P. C.; Meisel, D. *J. Phys. Chem.* **1982**, *86*, 3391-3395.

(174) Shipway, A. N.; Katz, E.; Willner, I. *ChemPhysChem* **2000**, *1*, 18-52.

(175) Seo, K.; Borguet, E. *Langmuir* **2006**, *22*, 1388-1392.

(176) He, M.; Ling, X.; Zhang, J.; Liu, Z. *J. Phys. Chem. B* **2005**, *109*, 10946-10951.

(177) Varazo, K.; Parsons, F. W.; Ma, S.; Chen, D. A. *J. Phys. Chem. B* **2004**, *108*, 18274-18283.

(178) Xie, X. N.; Chung, H. J.; Sow, C. H.; Wee, A. T. S. *Adv. Funct. Mater.* **2007**, *17*, 919-926.

(179) Tang, Q.; Li, H.; Song, Y.; Xu, W.; Hu, W.; Jiang, L.; Liu, Y.; Wang, X.; Zhu, D. *Adv. Mater.* **2006**, *18*, 3010-3014.

(180) Brinkmann, M.; Pratontep, S.; Chaumont, C.; Wittmann, J.-C. *Macromolecules* **2007**, *40*, 9420-9426.

(181) Ku, S.-Y.; Wong, K.-T.; Bard, A. J. *J. Am. Chem. Soc.* **2008**, *130*, 2392-2393.

(182) Pruniaux, B. R.; Adams, A. C. *Appl. Phys. Lett.* **1972**, *43*, 1980-1982.

(183) McGuiness, C. L.; Shaporenko, A.; Mars, C. K.; Uppili, S.; Zharnikov, M.; Allara, D. L. *J. Am. Chem. Soc.* **2006**, *128*, 5231-5243.

(184) Onclin, S.; Ravoo, B. J.; Reinhoudt, D. N. *Angew. Chem. Int. Ed.* **2005**, *44*, 6282-6304.

(185) Tao, Y. T. *J. Am. Chem. Soc.* **1993**, *115*, 4350–4358.

(186) Smith, E. L.; Porter, M. D. *J. Phys. Chem.* **1993**, *97*, 8032-8038.

(187) Ghosh, S. K.; Pal, A.; Kundu, S.; Nath, S.; Pal, T. *Chem. Phys. Lett.* **2004**, *395*, 366-372.

(188) Jin, R.; Cao, Y.; Mirkin, C. A.; Kelly, K. L.; Schatz, G. C.; Zheng, J. G. *Science* **2001**, *294*, 1901-1903.

(189) Noguez, C. *J. Phys. Chem. C* **2007**, *111*, 3806-3819.

(190) Su, K.-H.; Wei, Q.-H.; Zhang, X.; Mock, J. J.; Smith, D. R.; Schultz, S. *Nano Lett.* **2003**, *3*, 1087-1090.

(191) Biteen, J. S.; Lewis, N. S.; Atwater, H. A.; Mertens, H.; Polman, A. *Appl. Phys. Lett.* **2006**, *88*, 131109-1-131109-3.

(192) Mertens, H.; Biteen, J. S.; Atwater, H. A.; Polman, A. *Nano Lett.* **2006**, *6*, 2622-2625.

(193) Caruso, F.; Lichtenfeld, H.; Donath, E.; Möhwald, H. *Macromolecules* **1999**, *32*, 2317-2328.

(194) Tian, Z.-Q.; Ren, B.; Li, J.-F.; Yang, Z.-L. *Chem. Commun.* **2007**, *34*, 3514-3534.

(195) Kamat, P. V.; Shanghavi, B. *J. Phys. Chem. B* **1997**, *101*, 7675-7679.

(196) Walters, R. J.; Bourianoff, G. I.; Atwater, H. A. *Nat. Mater.* **2005**, *2*, 143-146.

(197) Bagalkot, V.; Zhang, L.; Levy-Nissenbaum, E.; Jon, S.; Kantoff, P. W.; Langer, R.; Farokhzad, O. C. *Nano Lett.* **2007**, *7*, 3065-3070.

(198) Xu, C. S.; Kim, H.; Yang, H.; Hayden, C. C. *J. Am. Chem. Soc.* **2007**, *129*, 11008-11009.

(199) Pons, T.; Medintz, I. L.; Sapsford, K. E.; Higashiya, S.; Grimes, A. F.; English, D. S.; Mattoussi, H. *Nano Lett.* **2007**, *7*, 3157-3164.

(200) Kooij, E. S.; Brouwer, E. A. M.; Wormeester, H.; Poelsema, B. *Langmuir* **2002**, *18*, 7677-7682.

(201) Bek, A.; Jansen, R.; Ringler, M.; Mayilo, S.; Klar, T. A.; Feldmann, J. *Nano Lett.* **2008**, *8*, 485-490.

(202) Lakowicz, J. R. *Principles of Fluorescence Spectroscopy*; 3 ed.; Springer: New York, 2006.

(203) Medintz, I. L.; Mattoussi, H. *Phys. Chem. Chem. Phys.* **2009**, *11*, 17-45.

(204) Anger, P.; Bharadwaj, P.; Novotny, L. *Phys. Rev. Lett.* **2006**, *96*, 113002-1--113002-4.

(205) Yun, C. S.; Javier, A.; Jennings, T.; Fisher, M.; Hira, S.; Peterson, S.; Hopkins, B.; Reich, N. O.; Strouse, G. F. *J. Am. Chem. Soc.* **2005**, *127*, 3115-3119.

(206) Govorov, A. O.; Lee, J.; Kotov, N. A. *Phys. Rev. B* **2007**, *76*, 125308-1--125308-16.

(207) Jennings, T. L.; Schlatterer, J. C.; Singh, M. P.; Greenbaum, N. L.; Strouse, G. F. *Nano Lett.* **2006**, *6*, 1318-1324.

(208) Jennings, T. L.; Singh, M. P.; Strouse, G. F. *J. Am. Chem. Soc.* **2006**, *128*, 5462-5467.

(209) Thomas, M.; Greffet, J.-J.; Carminati, R.; Arias-Gonzalez, J. R. *Appl. Phys. Lett.* **2004**, *85*, 3863-3865.

(210) Chen, Y.; Munechika, K.; Ginger, D. S. *Nano Lett.* **2007**, *7*, 690-696.

(211) Kühn, S.; Håkanson, U.; Rogobete, L.; Sandoghdar, V. *Phys. Rev. Lett.* **2006**, *97*, 017402-1--017402-1-4.

(212) Parak, W. J.; Gerion, D.; Pellegrino, T.; Zanchet, D.; Micheel, C.; CWilliams, S.; Boudreau, R.; Gros, M. A. L.; Larabell, C. A.; Alivisatos, A. P. *Nanotechnology* **2003**, *14*, R15-R27.

(213) Medintz, I. L.; Uyeda, H. T.; Goldman, E. R.; Mattoussi, H. *Nature Mater.* **2005**, *4*, 435-446.

(214) Sapsford, K. E.; Pons, T.; 1, I. L. M.; Mattoussi, H. *Sensors* **2006**, *6*, 925-953.

(215) Chan, W. C. W.; Nie, S. *Science* **1998**, *281*, 2016-2018.

(216) Chen, J.; Liao, W.-S.; Chen, X.; Yang, T.; Wark, S. E.; Son, D. H.; Batteas, J. D.; Cremer, P. S. *ACS Nano* **2009**, *3*, 173-180.

(217) Jaffar, S.; Nam, K. T.; Khademhosseini, A.; Xing, J.; Langer, R. S.; Belcher, A. M. *Nano Lett.* **2004**, *4*, 1421-1425.

(218) Bigioni, T. P.; Lin, X.-M.; Nguyen, T. T.; Corwin, E. I.; Witten, T. A.; Jaeger, H. M. *Nature Mater.* **2006**, *5*, 265-270.

(219) Galian, R. E.; de la Guardia, M.; Pérez-Prieto, J. *J. Am. Chem. Soc.* **2009**, *131*, 892-893.

(220) Derfus, A. M.; Chan, W. C. W.; Bhatia, S. N. *Nano Lett.* **2004**, *4*, 11-18.

(221) Liu, L.; Peng, Q.; Li, Y. *Inorg. Chem.* **2008**, *47*, 3182-3187.

(222) Aldana, J.; Wang, Y. A.; Peng, X. *J. Am. Chem. Soc.* **2001**, *123*, 8844-8850.

(223) Wagner, C. D.; Gale, L. H.; Raymond, R. H. *Anal. Chem.* **1979**, *51*, 466-482.

(224) Wagner, C. D.; Naumkin, A. V.; Kraut-Vass, A.; Allison, J. W.; Powell, C. J.; Rumble Jr., J. R. In *NIST X-ray Photoelectron Spectroscopy Database*; NIST.

(225) Aldana, J.; Wang, Y. A.; Peng, X. *J. Am. Chem. Soc.* **2001**, *123*, 8844-8850.

(226) Chan, Y.-H.; Schuckman, A. E.; Pérez, L. M.; Vinodu, M.; Drain, C. M.; Batteas, J. D. *J. Phys. Chem. C* **2008**, *112*, 6110–6118.

(227) McDowell, L. R. *Minerals in Animal and Human Nutrition*; 2nd ed.; Elsevier, Amsterdam, The Netherlands, 2003.

(228) Balch, P. A. *Prescription for Nutritional Healing*; 4th ed.; Penguin Group London, England, 2006.

(229) Lin, S.-Y.; Wu, S.-H.; Chen, C.-h. *Angew. Chem.* **2006**, *118*, 5044-5048.

(230) Lin, S.-Y.; Chen, C.-h.; Lin, M.-C.; Hsu, H.-F. *Anal. Chem.* **2005**, *77*, 4821-4828.

(231) Elghanian, R.; Storhoff, J. J.; Mucic, R. C.; Letsinger, R. L.; Mirkin, C. A. *Science* **1997**, *277*, 1078-1081.

(232) Kim, Y.; Johnson, R. C.; Hupp, J. T. *Nano Lett.* **2001**, *1*, 165-167.

(233) Chen, Y.; Rosenzweig, Z. *Anal. Chem.* **2002**, *74*, 5132-5138.

(234) Liang, J.-G.; Ai, X.-P.; He, Z.-K.; Pang, D.-W. *Analyst* **2004**, *129*, 619-622.

(235) Gattás-Asfura, K. M.; Leblanc, R. M. *Chem. Commun.* **2003**, *2003*, 2684-2685.

(236) Ruedas-Rama, M. J.; Wang, X.; Hall, E. A. H. *Chem. Commun.* **2007**, *2007*, 1544-1546.

(237) Touceda-Varela, A.; Stevenson, E. I.; n, J. A. G.-G.; Dryden, D. T. F.; Mareque-Rivas, J. C. *Chem. Commun.* **2007**, *2007*, 1998-2000.

(238) Chen, J.; Zheng, A.; Gao, Y.; He, C.; Wu, G.; Chen, Y.; Kai, X.; Zhu, C. *Spectrochim. Acta, Part A* **2008**, *69*, 1044-1052.

(239) Dong, C.; Qian, H.; Fang, N.; Ren, J. *J. Phys. Chem. B* **2006**, *110*, 11069-11075.

(240) Li, H.; Zhang, Y.; Wang, X. *Sensors and Actuators B* **2007**, *127*, 593-597.

(241) Chen, C.-Y.; Cheng, C.-T.; Lai, C.-W.; Wu, P.-W.; Wu, K.-C.; Chou, P.-T.; Chou, Y.-H.; Chiu, H.-T. *Chem. Commun.* **2006**, *2006*, 263-265.

(242) Ruedas-Rama, M. J.; Hall, E. A. H. *Anal. Chem.* **2008**, *80*, 8260-8268.

(243) Ali, E. M.; Zheng, Y.; Yu, H.-h.; Ying, J. Y. *Anal. Chem.* **2007**, *79*, 9452-9458.

(244) Munro, A. M.; Plante, I. J.-L.; Ng, M. S.; Ginger, D. S. *J. Phys. Chem. C* **2007**, *111*, 6220-6227.

(245) Chan, Y.-H.; Chen, J.; Wark, S. E.; Skiles, S. L.; Son, D. H.; Batteas, J. D. *ACS Nano* **2009**, *3*, 1735-1744.

(246) Onclin, S.; Ravoo, B. J.; Reinhoudt, D. N. *Angewandte Chemie-International Edition* **2005**, *44*, 6282-6304.

(247) Peng, Z. A.; Peng, X. *J. Am. Chem. Soc.* **2001**, *123*, 183-184.

(248) Tang, B.; An, J.; Zheng, X.; Xu, S.; Li, D.; Zhou, J.; Zhao, B.; Xu, W. *J. Phys. Chem. C* **2008**, *112*, 18361-18367.

(249) An, J.; Tang, B.; Ning, X.; Zhou, J.; Xu, S.; Zhao, B.; Xu, W.; Corredor, C.; Lombardi, J. R. *J. Phys. Chem. C* **2007**, *111*, 18055-18059

(250) Asami, H.; Abe, Y.; Ohtsu, T.; Kamiya, I.; Hara, M. *J. Phys. Chem. B* **2003**, *107*, 12566-12568.

(251) Cordero, S. R.; Carson, P. J.; Estabrook, R. A.; Strouse, G. F.; Buratto, S. K. *J. Phys. Chem. B* **2000**, *104*, 12137-12142.

(252) Jones, M.; Nedeljkovic, J.; Ellingson, R. J.; Nozik, A. J.; Rumbles, G. *J. Phys. Chem. B* **2003**, *107*, 11346-11352.

(253) Uematsu, T.; Kimura, J.; Yamaguchi, Y. *Nanotechnology* **2004**, *15*, 822-827.

(254) Uematsu, T.; Maenosono, S.; Yamaguchi, Y. *J. Phys. Chem. B* **2005**, *109*, 8613-8618.

(255) Hess, B. C.; Okhrimenko, I. G.; Davis, R. C.; Stevens, B. C.; Schulzke, Q. A.; Wright, K. C.; Bass, C. D.; Evans, C. D.; Summers, S. L. *Phys. Rev. Lett.* **2001**, *86*, 3132-3135.

(256) Wang, Y.; Tang, Z.; Correa-Duarte, M. A.; Pastoriza-Santos, I.; Giersig, M.; Kotov, N. A.; Liz-Marzán, L. M. *J. Phys. Chem. B* **2004**, *108*, 15461-15469.

(257) Zimnitsky, D.; Jiang, C.; Xu, J.; Lin, Z.; Tsukruk, V. V. *Langmuir* **2007**, *23*, 4509-4515.

(258) Stouwdam, J. W.; Shan, J.; Veggel, F. C. J. M. v.; Pattantyus-Abraham, A. G.; Young, J. F.; Raudsepp, M. *J. Phys. Chem. C* **2007**, *111*, 1086-1092.

(259) Chen, J.; Chan, Y.-H.; Yang, T.; Wark, S. E.; Son, D. H.; Batteas, J. D. *J. Am. Chem. Soc.* **2009**, *Submitted*.

(260) Sato, K.; Kojima, S.; Hattori, S.; Chiba, T.; Ueda-Sarson, K.; Torimoto, T.; Tachibana, Y.; Kuwabata, S. *Nanotechnology* **2007**, *18*, 465702.

(261) Zhang, Y.; He, J.; Wang, P.-N.; Chen, J.-Y.; Lu, Z.-J.; Lu, D.-R.; Guo, J.; Wang, C.-C.; Yang, W.-L. *J. Am. Chem. Soc.* **2006**, *128*, 13396-13401.

(262) Isarov, A. V.; Chrysochoos, J. *Langmuir* **1997**, *13*, 3142-3149.

(263) Fernández-Argüelles, M. T.; Jin, W. J.; Costa-Fernández, J. M.; Pereiro, R.; Sanz-Medel, A. *Anal. Chim. Acta* **2005**, *549*, 20-25.

(264) Xie, H.-Y.; Liang, J.-G.; Zhang, Z.-L.; Liu, Y.; He, Z.-K.; Pang, D.-W. *Spectrochim. Acta, Part A* **2004**, *60*, 2527-2530.

(265) Goh, S. W.; Buckley, A. N.; Lamb, R. N. *Minerals Engineering* **2006**, *19*, 204-208.

(266) Nakai, I.; Sugitani, Y.; Nagashima, K.; Niwa, Y. *J. Inorg, Nucl. Chem.* **1978**, *40*, 789-791.

(267) Xie, Y.; Zheng, X.; Jiang, X.; Lu, J.; Zhu, L. *Inorg. Chem.* **2002**, *41*, 387-392.

(268) Sadtler, B.; Demchenko, D. O.; Zheng, H.; Hughes, S. M.; Merkle, M. G.; Dahmen, U.; Wang, L.-W.; Alivisatos, A. P. *J. Am. Chem. Soc.* **2009**, *131*, 5285-5293.

(269) Jasieniak, J.; Mulvaney, P. *J. Am. Chem. Soc.* **2007**, *129*, 2841-2848.

(270) Zheng, J.; Nicovich, P. R.; Dickson, R. M. *Annu. Rev. Phys. Chem.* **2007**, *58*, 409-431.

(271) Xie, J.; Zheng, Y.; Ying, J. Y. *J. Am. Chem. Soc.* **2009**, *131*, 888-889.

(272) Bao, Y.; Zhong, C.; Vu, D. M.; Temirov, J. P.; Dyer, R. B.; Martinez, J. S. *J. Phys. Chem. C* **2007**, *111*, 12194-12198.

VITA

Yang-Hsiang Chan

Department of Chemistry, B2001, TAMU College Station, TX 77843

yhchan@mail.chem.tamu.edu

Education: Ph.D., Chemistry, Texas A&M Uinversity, 2010
B.S., Chemistry, National Sun Yat-sen University, Taiwan, 2001

Publication: Chan, Y.-H.; Chen, J.; Liu, Q.-S.; Wark, S. E.; Son, D. H.; Batteas, J. D. "Ultrasensitive Copper(II) Detection by Using Plasmon- and Photo-Enhanced Luminescence of CdSe Quantum Dots" *Anal. Chem.* **2010**, accepted.

Chen, J.; Chan, Y.-H.; Yang, T.; Wark, S. E.; Son, D. H.; Batteas, J. D. "Spatially Selective Optical Tuning of Quantum Dot Thin Film Luminescence" *J. Am. Chem. Soc.* **2009**, *131,* 18204-18205.

Chan, Y.-H.; Chen, J.; Wark, S. E.; Skiles, S. L.; Son, D. H.; Batteas, J. D. "Using Patterned Arrays of Metal Nanoparticles to Probe Plasmon Enhanced Luminescence of CdSe Quantum Dots" *ACS Nano* **2009**, *3*, 1735-1744.

Chan, Y.-H.; Schuckman, A. E.; Pe´rez, L. M.; Vinodu, M.; Drain, C. M.; Batteas, J. D. "Synthesis and Characterization of a Thiol-Tethered Tripyridyl Porphyrin on Au(111)" *J. Phys. Chem. C* **2008**, *112*, 6110-6118.

Honors and Awards:

2009	A.E. Martell Travel Awards
2009	Graduate Student Research and Presentation Grant
2008	1st place poster at Materials Characterization Facility, Texas A&M University
2008	2nd place & Session winner at 11th Annual Student Research Week, Texas A&M University